Laboratory Evaluation of Low to Medium Cost Particle Sensors

by

Ben Kinh Tan

A thesis
presented to the University of Waterloo
in fulfillment of the
thesis requirement for the degree of
Master of Applied Science
in
Mechanical and Mechatronics Engineering

Waterloo, Ontario, Canada, 2017

AUTHOR'S DECLARATION

I hereby declare that I am the sole author of this thesis. This is a true copy of the thesis, including any required final revisions, as accepted by my examiners.

I understand that my thesis may be made electronically available to the public.

Abstract

Low cost instruments for particulate matter monitoring directly benefits researchers, governments, and public with the overall goal of reducing the adverse effects of air pollution. As a result, companies have been rushing to produce such products. While laser light scattering is a low cost method, the technique suffers from drawbacks with accuracy. The performance of sensors on the market are questionable as few have been scientifically analyzed and the public lacks the technical means of verifying accuracy themselves. Thus, the objective of this research was to validate the performance of commercial laser light scattering based particle sensors. To accomplish this, eight were evaluated against a reference instrument and the relationship was modeled. Afterwards, a custom apparatus with improved calibration was developed for particulate monitoring.

The eight commercial sensors evaluated demonstrated high linearity with the reference instrument, but poor estimations of actual particulate concentrations. The performance of the sensors was strongly dependent on particle composition and size. Statistical analysis was also completed to compare linear parametric models used to calibrate the sensors with the non-parametric model. Results show that the linear models were frequently biased and therefore higher order polynomials should be used.

The custom apparatus was further evaluated with several laboratory particle sources as well as in real environments. Results show a low dependence on aerosol composition with higher flow rates. The instrument was calibrated to provide an "average" response for the tested particles. Models were developed for PM_{10} and $PM_{2.5}$ number and mass concentration measurements. The 95% prediction interval for PM_{10} and $PM_{2.5}$ number concentration was ±350 and ±360 particles/cm^3, respectively. For PM_{10} and $PM_{2.5}$ mass concentration, the intervals were ±75 and ±45 µg/m^3, respectively.

Acknowledgments

I would like to thank my supervisors Professors Zhongchao Tan and Tao Chen for their unwavering support, guidance, and confidence in my abilities. Their advice has not only helped me readily complete my thesis, but with my future career path as well.

I would also like to thank James Merli, Jason Benninger and Andy Barber for their technical support. I could not have completed my experiments without their help. My gratitude goes to Louise Green for assistance with administrative tasks. I am grateful to have met and worked with all the incredible people during my studies, especially Jiaxin Xu, Jorg Ahne, Maryam Razavi, Hasan Mrayeh, Eureka Choi, Wala Bkari, Professor Ali Ashrafizadeh, Abhishek Raj, and Dr. Dihua Wu.

I would like to acknowledge financial support from NSERC and O2 Canada.

Most notably, I would like to thank my friends and family who encouraged and supported me throughout my studies.

Dedication

To my family

Table of Contents

List of Figures

List of Tables

Chapter 1
Introduction

1.1 Background

Air pollution is used to describe airborne chemicals, particulate matter (PM), and biological materials which have negative impacts on human health, the environment, or economy. Commonly known pollutants are carbon monoxide, nitrogen oxides, sulfur oxides, volatile organic compounds, and ground level ozone. Human activity contributes to a significant portion of air pollution as sources include industrial and vehicle emissions, fossil fuel use, and burning wood for heating (The David Suzuki Foundation, 2014).

PM is a mixture of solid particles and liquid droplets in the air and in Ontario, chemical compositions consist of sulfates, nitrates, elemental and organic carbon, and soil (Ontario Ministry of the Environment and Climate Change, 2010a). PM is commonly classified by size into coarse, fine, and ultrafine particles. These correspond to particles with aerodynamic diameters of less than 10 µm (PM_{10}), 2.5 µm ($PM_{2.5}$), and 0.1 µm (nanoparticles), respectively. Air samples typically contain polydisperse aerosols, which are particulates of varying sizes at different concentrations. Research on long-term exposure to PM has shown serious health effects, including increased mortality from chronic cardiovascular and respiratory disease, lung cancer, and adverse reproductive outcomes (Engel-Cox et al., 2013). From 2008 to 2013 the World Health Organization measured PM in 67 countries and saw global urban air pollution levels increase by 8% (World Health Organization, 2016a), demonstrating a persistent problem.

The ability to measure particle size distribution (PSD) in an area over time is essential to improving understanding of adverse health impacts, atmospheric chemistry, sources of PM (Solomon and Sioutas, 2008), and impact of human activities on regional air quality (Gao et al., 2008). The information also allows preventative measures to be taken, from setting government policies to reducing individual exposure. With respect to health, the human body's natural filtration of particles smaller than 0.5 µm is very low (Schwab and Zenkel, 1998). Studies have provided some evidence that smaller $PM_{2.5}$ particles are more toxic than PM_{10}. This is because finer particles are more capable of penetrating the alveolar region of the respiratory system and with greater efficiency. Nanoparticles have been found to be more toxic per unit mass, likely due to increased surface area per unit mass and ability to penetrate the lung wall (Harrison and Yin, 2000).

Measuring PSD is also important to standardize emission limits and ensure acceptable air quality (Amaral et al., 2015). Countries adopt air quality standards to protect the public's health, and do so by balancing health risks, technological feasibility, economical considerations, and other social and political factors. Along with national capability in air quality management, these standards will vary from country to country. Once standards are adopted, governments will want to track progress by monitoring PM. The World Health Organization has assisted governments in setting standards by offering exposure limit guidelines intended for worldwide use. They are based on extensive scientific evidence relating to air pollution and its health consequences. Although adverse health effects cannot be entirely eliminated below these levels, the risks are significantly reduced and the limits have been shown to be attainable in large urban areas in highly developed countries (World Health Organization, 2005).

Since particulates are too small to be measured directly, instruments measure other properties instead and relate this back to a PSD. A wide range of instruments exist to make such measurements, including laser light scattering (LLS), aerodynamic particle sizing, filter based manual sampling (FBMS), beta attenuation monitors (BAM), tapered element oscillating microbalance (TEOM) (Engel-Cox et al., 2013), cascade impactors (CI), diffusion batteries (DB), aerodynamic particle sizers (APS), and scanning mobility particle sizer (SMPS). Each of these techniques present unique advantages in terms of cost, accuracy, particle size measurement range, spatial and temporal resolution, and limitations.

To obtain accurate representations of PM concentrations in an area, several instruments may be required to obtain data with sufficient spatial resolution. A single monitoring site may only represent PM levels of a very small area due to high concentration gradients. Such measurements will not be detailed enough for certain studies or represent exposures of nearby residents (Wang et al., 2015). Instruments for measuring PSD are typically expensive and lack portability, limiting the number which can be deployed. Cheap sensors allow PM monitoring with high spatial and temporal resolution by enabling several sensors to be deployed concurrently (Holstius et al., 2014). As such, there is the need for accurate, low cost, and portable PSD measuring instruments.

As a consequence of the need for low cost sensors, companies have been rushing to produce such products. Currently, sensors based on LLS is the only technique which can be produced cheaply. However, the method has poor accuracy as measurements are affected by particle refractive index, density, size, shape (Winkel et al., 2015), and humidity (Huang, 2007). Furthermore, these new low cost sensors have not been rigorously tested for their accuracy. Without proper scientific study, end users and government decision makers are at risk of being flooded with questionable air quality data. The public lack the technical means of verifying accuracy themselves and must take the quality of measurements on trust from the manufacturer (Lewis and Edwards, 2016). Properly validating existing low cost sensors will ensure that the instruments are accurate and users can be confident in the measurements obtained.

1.2 Research Objectives

The objective of this research is to validate the performance of commercial LLS based particle sensors. To achieve this goal, the following tasks were completed:

1. Experimental evaluation and modeling of the relationship between LLS sensors and APS measurements.
2. Develop and calibrate an apparatus for PM monitoring.

1.3 Thesis Structure

The thesis is organized into four chapters. Chapter 1 introduces the problem and objectives of the research. In Chapter 2, a literature review is presented to establish background knowledge required to successfully meet the research objective. Relevant theory and equations related to particle dynamics are first reviewed. Then, recent research conducted in the area of LLS evaluation is considered.

Chapter 3 describes the study of LLS based sensors completed. First the experimental setup and procedure for evaluating LLS sensors in a laboratory and real environment is outlined. Results are presented as linear models correlating sensor output to APS measurements. These are also validated by comparison with non-parametric regression models. Knowledge gained from the analysis provides insight into the characteristics of LLS sensors, which will be applied to developing a more accurate custom apparatus for PM monitoring. The custom device was further tested with various aerosol sources and calibration models were developed to obtain accurate measurements.

Chapter 4 concludes the thesis and provides recommendations for future work.

Chapter 2
Literature Review

2.1 Summary

This chapter begins with a brief discussion of particle dynamics topics relevant to the research work. Theory related to the LLS PSD measurement technique is also reviewed. Lastly, studies pertaining to the evaluation of LLS sensors against reference instruments in laboratory and ambient environments are presented.

The LLS is one technique used to measure PSD by measuring the intensity of light scattered by particles. The intensity depends on light wavelength, scattering angle, particle size, and relative index of refraction between medium and particle. The theory is constrained by several limitations which introduce errors when measuring real aerosols. Attempts have also been made to improve upon the design of LLS sensors.

The reviewed models proposed for correlating LLS sensors with reference instruments employed parametric regression, which may not be accurate due to certain assumptions made. Non-parametric regression does not make any assumptions about the data and is required to validate if the two models are statistically identical. Additional tests are required to validate a wider range of LLS sensors and determine their responses to different aerosol sources.

2.2 Particle Dynamics

A theoretical framework of particle dynamics is essential to research work in the area. This is especially important due to the different behaviour of micron-sized and nano-sized particles.

Knudsen Number and Cunningham Correction Factor

The drag force on particles is an important quantity as it directly affects their motion in a fluid. The parameter is calculated as:

$$F_D = \frac{C_D A_p \rho_f V_r^2}{2} \tag{2.1}$$

where C_D is the drag coefficient, A_p is the projected area of the particle, ρ_f is the density of fluid, and V_r is the relative velocity between particle and fluid. The drag coefficient is determined from correlations which depend on Reynold's number.

For large spherical particles, Stoke's law for drag force assumes no slipping occurs between the particle and fluid. The particle is much larger than gas molecules and the mean free path, so it behaves as though it is in a continuum. In this scenario, Equation 2.1 can be applied to calculate drag force on the particle. The dimensionless quantity which compares particle size to gas mean free path is the Knudsen number:

$$Kn = \frac{2\lambda}{d_p} \tag{2.2}$$

where λ is the gas mean free path and d_p is particle diameter. Continuum flow occurs when $Kn \ll 1$, making Equation 2.1 valid.

When $Kn \gg 1$, particles approach the size of gas molecules. The smaller the particle, the more slipping occurs with the molecules, making the flow non-continuum. Particle behaviour will be more similar to gas molecules. Slipping decreases the force that molecules i.e. the fluid exerts on the particle, so Equation 2.1 is no longer valid. To account for slip, Equation 2.1 is modified with the Cunningham slip correction factor C_c:

$$F_D = \frac{C_D A_p \rho_f V_r^2}{2C_c} \tag{2.3}$$

Several C_c correlations are provided in literature, with one being:

$$C_c = 1 + 1.392 Kn^{1.0783} \tag{2.4}$$

Values of C_c will always be equal to or greater than one, demonstrating that Stoke's law overestimates the drag force on nanoparticles because it assumes no slipping (Tan, 2014).

Stokes Number

The Stokes number is a dimensionless quantity which describes the motion of particles as they pass an obstacle. Due to inertia, smaller particles will tend to follow fluid streamlines, while larger particles continue in a straight line. The parameter is especially important in applications which measure PSD by classifying particles sizes due to their inertia. The Stokes number is given by:

$$Stk = \frac{\rho_p d_p^2 C_c u_0}{18 \mu d_c} \tag{2.5}$$

where ρ_p is the density of the particle, d_p is the particle diameter, u_0 is the undisturbed air velocity, μ is the gas viscosity, and d_c is the characteristic dimension depending on the application (Tan, 2014).

Aerodynamic Diameter

Aerosols are often non-spherical, so there is no geometrical diameter that can be determined. Instead, the aerodynamic diameter d_a is commonly measured. A particle has an aerodynamic diameter d_a if its terminal velocity in a gravitational field is the same as a spherical particle with standard density 1,000 kg/m^3 and diameter d_a. The expression for aerodynamic diameter is given by:

$$d_a = \sqrt{\frac{18\mu V_t}{C_c \rho_w g}} \tag{2.6}$$

where V_t is the particle terminal velocity, ρ_w is the density of water (1,000 kg/m^3), and g is the acceleration due to gravity (9.81 m/s^2) (Anderson, 2016).

2.3 Laser Light Scattering Technique

The LLS technique for measuring PSD is described in detail in this section. Other measurement techniques are covered in Appendix A. The goal of a PSD measurement instrument is to obtain a particle concentration versus size plot for the sample aerosol. Concentration may be expressed in terms of number, mass, volume, or surface area. Obtaining such a plot typically requires classifying particles by size first, followed by counting. On the contrary, certain techniques accomplish both simultaneously. Since particles are too small to be measured directly, another property is measured and related to size. Measurement techniques all exploit at least one of the following particle properties:

- Diffusivity
- Inertia
- Optics
- Electrical Mobility (Dhaniyala, 2017)

2.3.1 Theory of Operation

LLS operates upon the fact that particles scatter light at an angle and intensity dependent upon size. When light strikes a particle, it is either diffracted, refracted, reflected, or absorbed, as shown in Figure 2.1. Smaller particles scatter light more intensely and at smaller angles than larger particles. An aerosol sample produces a pattern of scattered light defined by intensity and angle, which is measured by an analyzer. All information about the PSD is contained in the scattering pattern, and it is obtained using an algorithm employing Mie theory (Webb, 2000).

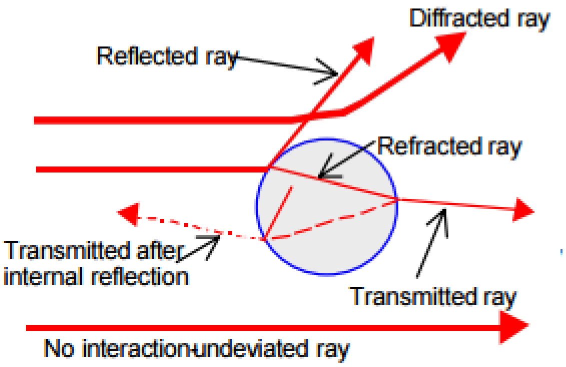

Figure 2.1: Types of interactions when light strikes a particle (Webb, 2000).

The intensity of light scattered is a function of its wavelength λ, scattering angle θ, particle size d_p, and relative index of refraction n between the medium and particle. Thus particle size can be calculated if I_{sc}, I_{in}, θ, λ, and n are known. Note that the scattering angle is measured relative to the incident light. This relation can be expressed as:

$$I_{sc} = I_{in}(\theta, \lambda, d_p, n) \tag{2.7}$$

Mie theory is used to relate measured scattering pattern to particle size, assuming all other parameters in Equation 2.7 are known. The theory accurately predicts the angle and intensity of light scattered by all sizes of spherical particles in any medium. Scattering angle and wavelength is fixed as it is dependent upon the design of the sensor. Often times, the refractive index is difficult to determine if the particle composition is unknown. Constraints and conditions of the theory is as follows:

- Incident light is monochromatic and composed of plane waves.
- The particle is isotropic and spherical.
- Scattering and absorption is considered.

- Only light scattered from the primary light source is considered, and not light scattered from one particle to another (Webb, 2000).

An example light scattering pattern of a single particle is shown in Figure 2.2. The pattern shows light intensity at different scattering angles projected onto a screen. Also shown is an equivalent graphical representation of intensity versus scattering angle. When multiple particles are present, each produce a similar pattern shifted in space proportional to the distance between individual particles. Lenses are used to direct light from all particles to converge at specific locations on a focal plane. The size of the scattering pattern projected on the focal plane depends on the focal length of the lens, and its location relative to the source of scattering (Webb, 2000).

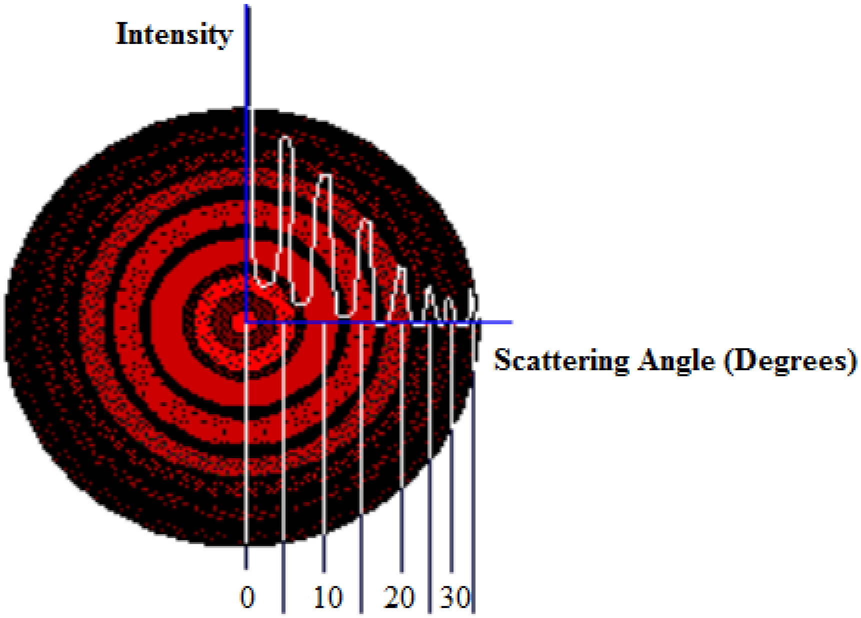

Figure 2.2: Light scattering pattern of a particle (Webb, 2000).

Each particle size produces a unique scattering pattern, for a fixed material, medium, and wavelength of light. Figure 2.3 shows normalized patterns for various particle sizes as a function of scattering angle. Scattering patterns also follow superposition. When patterns are superimposed from identical particle sizes, the result is the same pattern but brighter. Superposition of different patterns from different particle sizes create a new composite pattern (Webb, 2000).

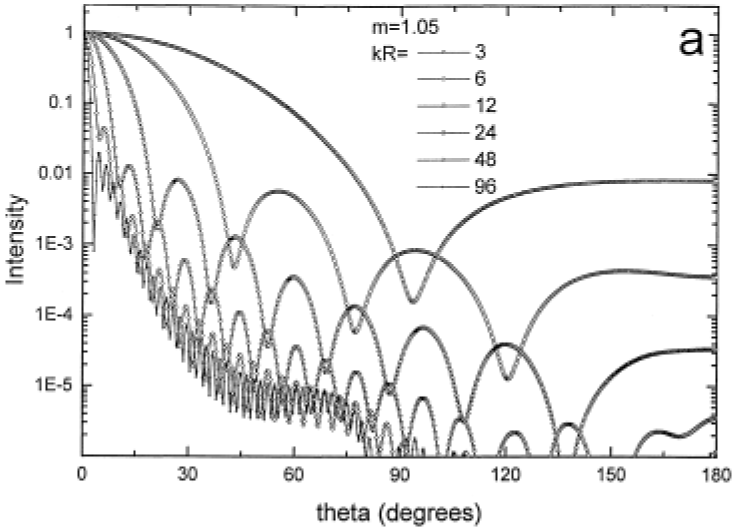

Figure 2.3: Normalized Mie scattering curves for various particle sizes (Sorensen and Fischbach, 2000).

Photodetectors are used to detect the intensity of scattered light. The energy of incident photons on these devices cause electrons to be liberated. This produces an electrical signal (current) which is proportional to the intensity of detected light. Photodiodes are a type of photodetectors made of a semi-conductor junction. An array of photo-diodes are placed on the focal plane of a LLS sensor and collects multiple signals of light intensity. The area of each element must be large enough so that sufficient light is incident to produce a suitable signal to noise ratio (Webb, 2000).

While the equations which describe Mie scattering are complex (Sorensen and Fischbach, 2000), there is a simplification known as Rayleigh scattering if the particle size is much less than the light wavelength. First, a size parameter is defined by:

$$\alpha = \frac{\pi d_p}{\lambda} \tag{2.8}$$

Rayleigh Scattering regime applies when $\alpha \ll \lambda$. In such situations, the scattered intensity may be expressed as:

$$I_{sc} = I_{in} \frac{1 + cos^2\theta}{2L^2} \left(\frac{2\pi}{\lambda}\right)^4 \left(\frac{n^2 - 1}{n^2 + 2}\right)^2 \left(\frac{d_p}{2}\right)^6 \tag{2.9}$$

where L is the distance to the particle (The University of Manchester, 2016).

2.3.2 Instruments Developed

The theoretical response curves of LLS are not practical to use for measuring PSD. Instead, a series of calibration particles of known size are used to determine instrument response over its full size range. A curve is then fitted to the measurements to allow sizing of particles falling in between the calibration points (The University of Manchester, 2016). Nevertheless, attempts have been made to improve the design of LLS based sensors.

Grimm and Eatough (2009) developed a light scattering based aerosol spectrometer consisting of: (i) a total aerosol inlet; (ii) an optical bench with integrated laser connected with (iii) a sampling pump with constant airflow; (iv) an analogue board for the particle sizing and classification; (v) a digital board for data conversion, processing, and storage; and (vi) a serial port. The optical setup is shown in Figure 2.4, consisting of a photo-diode at 90° detecting the scattered light. Particles from 0.25 to 32 µm were measured using a single laser diode and categorized into 32 size channels. The instrument generates clean sheath air to ensure dust does not contaminate the laser optical assembly.

The inlet's collection efficiency of particles up to 10-20 µm was found to be sensitive to wind speed. Above speeds of 8 m/s, collection efficiency decreased. A sampling head efficiency curve was thus established to make the necessary corrections. To calculate PM mass, a density factor corresponding to a established "urban environment" factor was used. The conversion was completed based on comparisons with Federal Reference Method (FRM) in several urban environments, and assuming that aerosols in all urban

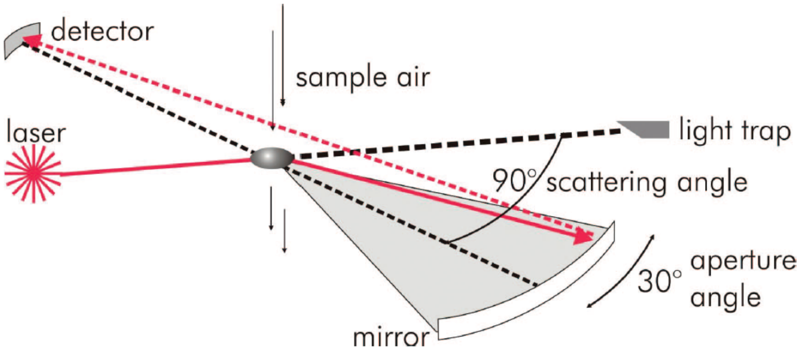

Figure 2.4: Schematic of the LLS configuration by Grimm and Eatough (2009).

environments are dominated by similar anthropogenic emissions. This allows the instrument to use a constant particle density over the full size range at all locations to calculate PM mass. Since particles below 0.25 µm cannot be detected, the measured data and log-normal Gaussian distribution is applied to account for their mass. Results were found to be in agreement with a filter dynamic measurement system.

While the results of Grimm and Eatough (2009) were favorable, the researchers made an important assumption that aerosols in all urban environments are dominated by similar anthropogenic emissions. This may be satisfactory for calibrating the instrument for use in urban environments, but obviously limits the device from being used anywhere else. In addition, any changes in emission sources in the urban environment would cause measurement errors and be undetectable by the device.

LLS sensors can also provide mass based concentration measurements if the particle density is known. Assuming spherical particles, calculating the volume of each size bin, summing, and multiplying by density yields the mass. However, the densities of particles vary significantly, from 700 kg/m^3 for oils to several thousands for metals, and may be unknown. To address this issue, Schrobenhauser et al. (2014) developed a LLS based sensor capable of determining the densities of PM using an impactor filter. The process is completed in three steps:

1. Determine the PSD without inertial filtering.
2. Connect the impactor filter to the inlet of the sensor and obtain a second PSD.
3. The difference of both PSDs represent the filtering efficiency if the density of particles is equal to the reference particles. If more larger/smaller particles were filtered, then the particle density must be larger/smaller as well. By knowing the particle size and density at a reference 50% filtering efficiency, the density of the sample is calculated as:

$$\rho = \frac{\rho_{ref} d^2_{p,50,ref} C_{c,ref}}{d^2_{p,50} C_c} \tag{2.10}$$

Although light scattering devices are typically calibrated in the factory, they are likely to show substantial bias when used in the field. Differences in refractive index, density, size, and shape between the calibration and actual aerosols lead to measurement errors (Winkel et al., 2015). These factors arise due to the dependence of light scattering intensity on several variables, as discussed in the previous section.

2.4 Light Scattering Sensor Evaluation

LLS sensors are sensitive to particle composition, so the difference between calibration and actual aerosols detected introduce great uncertainty and error in their measurements. In addition, other factors such as humidity and temperature have been found to affect readings (Wang et al., 2015). However, studies evaluating commercially available sensors have shown strong correlations with well characterized instruments. The results demonstrate potential for LLS sensors to monitor PM with great spatial and temporal resolution. Table 2.1 summarizes completed studies and important findings pertaining to the evaluation of LLS sensors.

Table 2.1: Summary of LLS sensor evaluation studies.

Researcher	**Sensors**	**Reference**	**Results**
Wang et al. (2015)	• Shinyei PPD42NS • Samyoung DSM501A • Sharp GP2Y1010AU0F	• TSI SidePak • TSI SMPS • TSI Air-Assure	• High sensitivity to particle composition, humidity, and particle size. • Strong linear correlations with the SidePak ($R^2 > 0.88$).
Northcross et al. (2013)	• Dylos	• TSI DustTrak	• High sensitivity to particle composition. • Strong linear correlations with the DustTrak ($R^2 > 0.81$).
Jiao et al. (2016)	• Shinyei • Dylos DC1100 PC • Dylos DC1100 PRO-PC • AirBeam • MetOne 831 • Air Quality Egg	• MetOne BAM 1020	• Poor to moderate correlation with the MetOne BAM 1020. • High agreement between identical sensors.
Han et al. (2017)	• Dylos DC 1700	• Grimm 11-R	• Good correlations ($R^2 > 0.78$) • Affected by RH > 60%.
Manikonda et al. (2016)	• Speck • Dylos 1100 PRO • Dylos 1700 • TSI AirAssure • UBAS	• TSI APS 3321 • TSI FMPS 3091 • GRIMM 1.109	• Sensors perform with adequate precision. • Field calibration with standard instrument required.

Continued on next page...

Table 2.1: Continued from previous page.

Researcher	Sensors	Reference	Results
Kelly et al. (2017)	• Plantower PMS 1003 • Plantower PMS 3003 • Shinyei PPD42NS	• Thermo Scientific 1405-F TEOM • Thermo Scientific Sharp 5030 BAM • GRIMM 1.109	• Good correlations ($R^2 > 0.72$) • Additional measurements needed under a variety of ambient conditions. • Potential interference caused by custom sensor housing.
Austin et al. (2015)	• Shinyei PPD42NS	• TSI APS 3321	• Sensor response was linear up to 50 µg/m^3. • Good linear correlation in this range ($R^2 > 0.66$).
Holstius et al. (2014)	• Shinyei PPD42NS	• Met One BAM-1020 • GRIMM 1.108 • TSI DustTrak II • Dylos DC1700	• Moderate to strong correlations with intercomparison of all instruments ($R^2 > 0.49$).
Huang (2007)	• TSI DustTrak	• Met One E-BAM	• Moderate correlation when E-BAM inlet was not heated ($R^2 = 0.74$). • Higher RH increased readings of the DustTrak.

Wang et al. (2015) evaluated the following aspects of three low cost LLS sensors in a custom built chamber:

1. Linearity of response.
2. Concentration resolution.
3. Limit of detection.
4. Dependence on particle composition.
5. Sensitivity to particle size.
6. RH and temperature influence.

Two sensors were tested for each sensor model, and the SidePak was used in all tests.

Linearity of response was evaluated with incense burning as the particle source, and responses were inter-compared between all sensors. Although results show strong correlations between all sensors, the TSI SidePak reference instrument was also LLS based. This methodology has the potential for error due to the SidePak also being susceptible to errors of LLS methods. Sucrose, NaCl, and ammonium nitrate (NH_4NO_3) were used to evaluate sensor dependence on particle composition. For the same mass concentrations measured by SMPS, the tested sensors provided different output depending on the particle source. Sucrose always gave the highest reading, followed by NH_4NO_3 and NaCl. To evaluate dependence on particle size, 300, 600, and 900 nm monodisperse polystyrene latex (PSL) particles were generated. For the same mass concentrations measured by SMPS, the tested sensors provided different output depending on the particle size. 900 nm particles always gave the highest output, followed by 600 and 300 nm particles. RH was also found to influence sensor measurements, but with no clear relationship.

Northcross et al. (2013) evaluated the Dylos against a DustTrak in an indoor aerosol chamber using woodsmoke, 0.5 µm PSL particles, and ammonium sulphate. Tests were also conducted in an outdoor environment with real atmospheric aerosols. The PSL tests showed that the Dylos' 2.5 µm size bin did not respond to the particles, and only the other 0.5 µm size bin gave a reading. Sensitivity to aerosol composition was evaluated by plotting the Dylos versus DustTrak response. Each particle source produced a different slope. The refractive index of PSL, woodsmoke, and ammonium sulphate is 1.58, 1.57, and 1.53, respectively. The slopes of PSL and woodsmoke were closest as is their refractive indices, suggesting the difference is related to refractive index rather than particle size. A MetOne E-BAM was used to adjust readings of the DustTrak and Dylos in ambient testing. A mean correction factor over the entire sampling period adjusted readings to average out temporal changes in particle composition. It was also found that there was less variability in the sensor response in laboratory tests compared to outdoors. This was because the aerosol composition outside changes over time, while only a single aerosol source was used in the laboratory tests.

Jiao et al. (2016) evaluated several LLS sensors in an outdoor environment against a BAM over several weeks. It is noted that the Airbeam and Air Quality Egg used an internal Shinyei PPD60PV and PPD42NS sensors, respectively. While sensors had poor to moderate correlations with the reference instrument, comparisons of identical sensors revealed generally the highest agreement. This demonstrates the high precision of LLS sensors and potential use for indicating relative concentration levels. However, their readings may not be representative of $PM_{2.5}$ reference instruments. Sensors moderately correlated with BAM were further investigated to see if improved models (multiple linear regression) can be developed by including temperature, RH, or days of use. Results show minor improvements in R^2 values, with the best being +0.11 for the Dylos when days of use and RH was accounted for.

Han et al. (2017) evaluated the Dylos DC 1700 against the GRIMM 11-R in an outdoor urban residential area. The GRIMM 11-R is also a LLS based sensor, and number concentrations from the Dylos was converted to mass concentrations using measurements from the GRIMM 11-R. The overall correlation between the sensors was $R^2 = 0.78$, but dropped to $R^2 = 0.48$ when considering only coarse particles. Sensor measurements were close when the RH was less than 60%, but Dylos measurements were higher relative to GRIMM with greater humidity.

Manikonda et al. (2016) evaluated various LLS sensors in an indoor 21.37 m^3 test chamber using cigarette smoke and Arizona Test Dust. A Samyoung DSM501A and Sharp GP2Y1010AU0F sensor is used in the Speck and UB AirSense (UBAS), respectively. For each test, particles were introduced into the chamber until a peak concentration was reached, and then allowed to equilibrate. This was repeated two more times for a total of three peak concentrations. For cigarette smoke, the Speck, AirAssure, and UBAS overestimated particle concentrations compared to APS, while the Dylos underestimated. When Arizona Test Dust was used, the Speck overestimated concentrations again, while the AirAssure and Dylos underestimated. Overall, the sensors performed with high precision but low accuracy for estimating PM concentrations.

Kelly et al. (2017) evaluated three LLS sensor models in a controlled wind tunnel and ambient environment. PMS sensors were found to correlate well with the reference instruments in ambient and laboratory environments. The PSD measured by PMS sensors in the wind tunnel were comparable to those obtained by GRIMM. During periods of high ambient concentrations the PMS sensors provided overestimated measurements. The sensors were also found to be more sensitive to particle properties compared to research grade instrumentation. Experiments were also conducted evaluating the PMS sensors with and without a housing in the wind tunnel. It was found that the housing design appears to inhibit particles to flow into the PMS sensors, as those without a housing were more responsive to changes in PM concentration. Results highlighted the importance of evaluating the sensors under target conditions and developing the appropriate correction factor if measurements comparable to advanced instruments are desired.

Austin et al. (2015) evaluated four Shinyei PPD42NS sensors against the APS in a laboratory chamber. Monodisperse polystyrene spheres with diameters 0.75, 1, 2, 3, and 6 µm were used, as well as polydisperse ASHRAE test dust #1. Responses were linear for concentrations below 50 $\mu g/m^3$ and non-linear until approximately 800 $\mu g/m^3$ where saturation occurs. As the monodisperse particle size increased, the slope relating sensor output to APS increased. The maximum concentration limit detected by the sensors also varied with particle source. Every sensor was found to have a unique output versus APS, so calibration of all sensors should be performed before deployment. The researchers note that in cases of unknown polydisperse aerosols, obtaining mass concentrations from the sensor may be difficult without the aid of gravimetric sampling.

Holstius et al. (2014) design a platform around the Shinyei PPD42NS for calibration in an outdoor environment. Precision and accuracy were found to be comparable to considerably more expensive reference instruments. Correlations between PPD42NS sensors were strong ($0.91 < R^2 < 0.92$), but weaker with the BAM ($0.55 < R^2 < 0.60$). The effects of light, temperature, or RH did not appear to impact sensor readings.

Huang (2007) compared the DustTrak with a BAM at various ambient RH, and found that the DustTrak provided higher readings regardless of whether the inlet heater of the BAM was turned on or off. Without heating, there was a moderate correlation ($R^2 = 0.74$) between the monitors. With heating, the correlation was poor ($R^2 = 0.17$). Overall, higher RH affected the DustTrak by increasing its readings.

Evaluations of LLS sensors in laboratory and real environments have repeatedly shown high precision among identical units and reference instruments for a particular aerosol source. Correlations with reference instruments were strong and relationships were almost always linear, with the exception of non-linear responses at high concentrations for certain devices. Sensors were highly dependent on particle composition, and accuracy was rarely observed without calibration.

Mixed results were found on the effects of humidity, but generally has no impact on sensors at low levels. Humidity may cause hygroscopic growth of particles and water droplets being detected by the sensor, leading to overestimation of particle mass concentrations (Manikonda et al., 2016). Findings were consistent for temperature not having effects on sensor measurements. An exception to this may be sensors which use resistive heating to induce natural convection and draw in aerosols such as the PPD42NS. Convective flow is proportional to temperature gradient, which will vary with ambient temperature (Kelly et al., 2017).

2.5 Knowledge Gap and Research Needed

Clearly, models are required to correlate each individual LLS sensor to advanced instruments if accuracy is desired. With the considerable amount of low cost LLS sensors on the market comprising of different designs, it is especially important to validate additional devices and determine their sensitivity to aerosol sources. Manikonda et al. (2016) noted a lack of precision among different monitors, which can be attributed to design parameters such as different laser wavelengths, orientation of the light source and detector, the mode of particle transfer from the inlet to sensor, and air flow rate. Furthermore, many researchers used another LLS sensor as the reference instrument, so sources of error unique to LLS method may not be revealed this way. Thus, additional laboratory tests are required for a wider selection of LLS sensors to obtain a general consensus on the performance of various instruments.

In the literature review of LLS sensor evaluations, the models developed to correlate devices with advanced instruments have been parametric models. The most common modeling approach observed was linear regression using ordinary least squares (OLS), but several assumptions must be made which if violated, would decrease accuracy of the model. An alternative approach is to model the relationship with non-parametric regression, which makes no assumptions about the distribution of data and is always valid. The disadvantage is that the method is more difficult to comprehend and implement. However, if there is no difference between the parametric and non-parametric models statistically, it is possible to prove this and simply use the parametric model. To ensure that using linear parametric models for calibrating LLS sensors is valid, comparison with the non-parametric model should be completed.

While studies have been completed comparing LLS sensors to a reference instrument, few address the issue of inaccurate measurements for PM monitoring in real environments.

The problem persists due to the dependence of measurements on particle source and the fact that compositions of real particulates are not universal. With gas instruments, bottled standards are available for calibration. However, the technique is impractical to apply for particulates due to difficulties in creating stable atmospheric suspensions of particulates to which populations are actually exposed (Holstius et al., 2014). Further study is required to gauge how much LLS sensor response varies with particle source. Afterwards, an "average" calibration curve can be obtained along with the associated uncertainty. This strategy may be the most ideal when constrained by lack of knowledge of the aerosol composition.

Chapter 3

Study of Laser Light Scattering Sensors

3.1 Summary

Eight randomly selected commercial LLS based particle sensors were evaluated by comparison with APS. Sensors were tested in a homemade wooden chamber with two particle sources: NaCl and road dust. The results showed high linearity at low particulate concentrations and repeatability versus APS, but poor estimations of actual particulate concentrations. Performance of the sensors was also strongly dependent on particle composition and size.

From the literature review completed, parametric models were always used to relate LLS sensor measurements to a reference instrument. However, certain assumptions are made about the data which if violated, leads to bias and misleading conclusions. Thus linear models developed from the sensor evaluation were verified by comparison with non-parametric regression curves, which are more accurate in describing the relationship. It was found that statistical differences often existed with the two models, which indicates that linear models are inadequate for calibrating LLS sensors. Higher order polynomials are therefore recommended, and their validity should also be confirmed with non-parametric models following the same procedure.

As realized from the study completed thus far, the market lacks accurate and well characterized low cost particulate monitors. Using the knowledge gained, a custom portable particle counter (PPC) was developed to address this need. One of the evaluated sensors was selected to be incorporated in the PPC apparatus for particle detection. Since one of the drawbacks of LLS sensors is sensitivity to particle source, the apparatus was designed to reduce this effect. Also, the PPC was further evaluated with several additional real and laboratory generated aerosols to obtain an "average" response. Calibration models were developed for its PM_{10} and $PM_{2.5}$ number and mass concentration measurements. The calibrated PPC showed low sensitivity to particle source, high accuracy, and high linearity with APS compared to just the PMS A003 sensor. The 95% prediction interval for PM_{10} and $PM_{2.5}$ number concentration was ±350 and ±360 particles/cm^3, respectively. For PM_{10} and $PM_{2.5}$ mass concentration, the intervals were ±75 and ±45 µg/m^3, respectively.

Additional testing of the PPC in real environments is still required. With the available resources, the PPC could only be evaluated at low ambient PM concentrations and in a small range. Particulate levels in a real environment cannot be easily controlled as with laboratory generated particles. The PPC should be tested in settings with consistently poor air quality, such as China, Iran, or India to evaluate its performance at higher concentrations. Testing over long periods of time is also required so that a wide concentration range is observed. Since laboratory particles were mainly used to develop the calibration models, improvements can be made by using more relevant data.

3.2 Materials and Method

3.2.1 Particle Sensors

Eight randomly chosen commercial LLS based particle sensors were tested in a laboratory chamber. The Node was further evaluated in a real environment. These devices or monitors were available for purchase online. Specifications of the sensors are summarized in Table 3.1 and photographs can be found in Figure 3.1. The general working principles of the sensors are also briefly introduced as follows.

Table 3.1: Specifications of the evaluated particle sensors.

Sensor	Dimensions W×H×D (cm)	Measurement Range (µm)	Channels & Concentration Units	Cost (CAD)
Fluke 985	9.9×27.2×5.3	0.3-10	6#	$6100
Handheld 3016	12.7×22.2×6.4	0.3-25	6#	$5000
DC1100 Pro	11.4×17.8×7.6	>0.5	2#	$380
Node	18.2×8.1×10.3	0.3-10	2 Mass	$310
PMS A003	3.8×3.5×1.2	0.3-10	6 #, 2 Mass	$40
PMS 7003	4.8×3.7×1.2	0.3-10	6 #, 2 Mass	$40
SDS 021	4.3×3.2×2.5	0.3-10	2 Mass	$40
DN7C3CA006	5.3×5.1×4	<2.5	1 Analog Voltage	$40

Figure 3.1: Photograph of the evaluated sensors. Clockwise from top left: Fluke 985, Handheld 3016, DC1100 Pro, Node, DN7C3CA006, SDS 021, PMS 7003, and PMS A003.

Fluke 985

The Fluke 985 (Fluke Inc.) counts particles using a 775 to 795 nm, 90 mW class

3B laser and features six size channels: 0.3, 0.5, 1.0, 2.0, 5.0, and 10 µm. Aerosol is drawn in by an internal pump and the rated maximum concentration is 140 particles/cm^3. Measurement intervals down to one second can be set and readings are displayed on a LCD screen. The sensor also carries a rechargeable battery, utilizes an isokinetic inlet, automatically logs timestamps with measurements, and can store up to 10,000 records. Data is retrieved through a USB connection with a computer.

Handheld 3016

The Handheld 3016 (Lighthouse Worldwide Solutions) employs a laser diode to count particles in six size channels, and bin widths can be chosen when ordering the product. Aerosol is drawn in by an internal pump and the rated maximum concentration is 280 particles/cm^3. Sampling intervals can be set and readings are displayed on a touch screen. Similar to the Fluke 985, the sensor features a rechargeable battery, isokinetic inlet, automatically logs timestamps with measurements, and can store up to 3,000 records. Data can be easily accessed with RS-232 communication and software provided by the manufacturer. Temperature and humidity probes are also included with the system.

DC1100 Pro

The DC1100 Pro (Dylos Corporation) counts particles in two size channels via a laser. Readings are displayed for small particles greater than 0.5 µm, and large particles greater than 2.5 µm. An internal fan draws in air from an opening on the back of the sensor and a LCD screen showing actual particle count readings. Data can be recorded on the sensor's internal memory by minute, hour, or day. However, timestamps are not included unless logging is completed via serial connection to a computer.

Node

The Node (AirVisual) counts particles using a laser and also considers factors such as temperature, humidity, and outliers. Particles from 0.3 to 10 µm are counted and displayed as PM_{10} and $PM_{2.5}$ mass concentrations. Other features include a rechargeable battery, LCD screen, and Wi-Fi connection for remote monitoring. Samples can be logged every ten seconds and downloaded to a computer.

PMS A003 and PMS 7003

The PMS A003 and PMS 7003 are similar sensors both manufactured by PlanTower. The only difference appears to be physical dimensions and cost. Both use light scattering and were the only low cost sensors studied to report both number and mass concentrations. Number concentrations are divided into six size channels. For mass concentration, the sensor reports readings for a ”standard” and ”atmospheric” type particle. The “standard” reading refers to industrial metal particle densities used for mass calculations and is suitable for environments such as an industrial production workshop. The “atmospheric” reading refers to pollutants commonly found in the atmosphere, and suitable for use in an indoor environment. Air is drawn in by an internal fan and readings are automatically sent to UART serial output. When the concentration detected by the sensor is stable, the sampling interval is every two to three seconds. However, when the concentration rate of change is high, the sensor automatically reduces the sampling interval down to 200 milliseconds. Since these sensors provide three different concentration readings, in this work they will be abbreviated with their names followed by “Num”, “Std”, and “Atm” for number concentration, standard particle mass concentration, and atmospheric particle mass concentration, respectively.

SDS 021

The SDS 021 (Nova Fitness Co. Ltd.) uses light scattering to report $PM_{2.5}$ and PM_{10} readings at concentrations from 0 to 1,000 $\mu g/m^3$. A built in fan draws in aerosol and a spiral duct separates the inlet into small and large particle streams. The sensor uses UART communication protocol and readings are automatically generated every second.

A 5V power supply is required to operate the sensor.

DN7C3CA006

The DN7C3CA006 (Sharp Corporation) also uses light scattering method and measures only $PM_{2.5}$ up to 500 µg/m^3. Aerosol is drawn in by a fan and $PM_{2.5}$ is separated by a virtual impactor. A pulse driving condition applied to the LED is required to operate the sensor. This in turn produces a output pulse, whose analogue voltage is proportional to the measured $PM_{2.5}$ mass concentration. A linear correlation between measured voltage and mass concentration has been recommended by the manufacturer. The model takes into account humidity effects, and shows that above 50% relative humidity, the same particle mass concentration will cause a higher output voltage.

APS 3321

The APS 3321 (TSI Inc.) was the reference instrument used in this study, and includes many features of the low cost sensors, as well as improvements. The device can measure particle sizes from 0.5 to 20 μm and provides high resolution data with 52 size channels. Concentration accuracy is specified to be ±10% of reading plus variation from counting statistics. When operating, aerosol sample is accelerated through an orifice and a particle's aerodynamic size determines its rate of acceleration. Small particles accelerate more rapidly than larger ones due to lower inertia. Particles then pass two laser beams and produce two pulses of scattered light. The time delay between the pulses determines the particle's velocity and aerodynamic diameter. From this information, a particle size distribution based on number concentration can be determined. To calculate the mass concentration, the particle density must be supplied to the APS. These parameters were known for laboratory generated particles Although the true densities of particles are likely lower due to voids in their structure, the values were used by APS for mass concentration estimates. For real aerosols, densities recommended by literature was used for the calculation.

DustTrak II

The DustTrak II (TSI Inc.) was the reference instrument used in the real environment test. The device uses LLS to measure particle concentrations in conjunction with inlet conditioners corresponding to $PM_{2.5}$, PM_{10}, and respirable size fractions. A internal pump draws in aerosol and the rated concentration range is 1 to 150,000 µg/m^3. Readings are displayed on a touchscreen, can be logged with timestamps, and can be retrieved via USB. Devices also include a battery for portability.

3.2.2 Test Setup

Laboratory tests were conducted in a 58×58×28 cm homemade wooden chamber with acrylic glass lid as shown in Figure 3.2. Cracks and gaps in the chamber were sealed to reduce particle loss and achieve a more uniform particle distribution. The lid was sealed using rubber strips and toggle clamps to apply pressure. The remaining edges of the chamber were sealed with wood glue. Two holes with diameters of 19 mm were drilled in the bottom corners of the chamber to pass electrical wires through the wall. Wires were routed between two rubber stopper halves, plugged into the hole, and sealed with silicon. Two small holes were also drilled in the center top and bottom of the chamber to serve as dust and APS inlets, respectively. Compression fittings were placed through the holes and sealed with O-rings.

Test sensors were placed side by side on the chamber floor centerline, and oriented such that their inlets faced the same side wall without obstruction. Inlets were also at least 5 cm apart from each other to avoid interference with air intake, and sensors were tested in batches with no defined groupings. Wooden blocks were placed under sensors as required so that all inlets were approximately 12 cm from the floor. The APS was placed

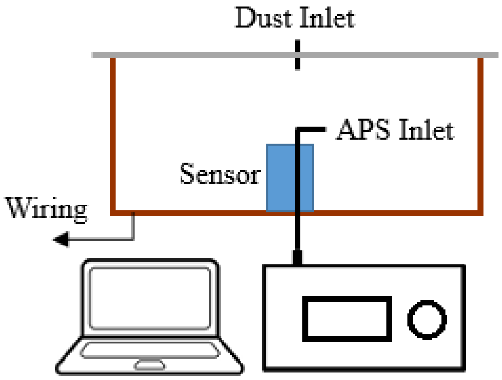

Figure 3.2: Schematic of the test chamber used in the experiments.

outside and directly underneath the chamber, with a tube connection to the bottom fitting. This minimized tubing length and consequently particle loss. A chamber-side tube was attached to the fitting to sample air at the same height and direction as the low cost sensors. The APS sampled air at a rate of 5.0 L/min, which gets exhausted outside the chamber. In contrast, the tested sensors recirculated air back inside. As a result, the fitting on the lid was left opened during the tests to replace air removed by APS.

In a similar study, Wang et al. Wang et al. (2015) found the concentration in their chamber to be uniformly distributed without mixing. The experimental setup and procedure was comparable with this work as the chambers were of the same dimensions, particles were introduced to the chamber via a tube, holes were made for sampling to reference instruments placed outside, and test sensors made measurements as settled due to gravity. Particles in the chamber were transported mainly by random diffusion, and due to the relatively large size of the chamber and limited air exchange rates, forced convection through mixing would create an uneven distribution of particles. The researchers found differences in particle concentrations at the four sides of the chamber to be less than 15%, at concentrations up to 1,000 μg/m^3.

Tests were conducted using ISO road test dust and sodium chloride (NaCl) particles. The Fluidized Bed Aerosol Generator (FBAG) 3400A (TSI Inc.) was used to generate road dust particles. A schematic of the FBAG setup is shown in Figure 3.3. Clean dry air from the Filtered Air Supply 3074B (TSI Inc.) was supplied to the FBAG. Descriptions on the working principle of the FBAG is described in Section D.3.2.

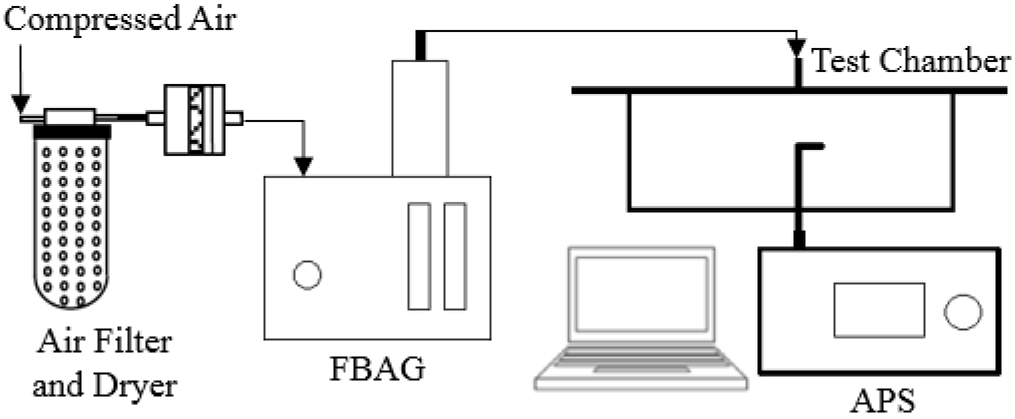

Figure 3.3: Schematic of road dust particle generation.

The Aerosol Generator 3076 (TSI Inc.) was used to generate NaCl particles and a description of its working principle can be found in Section D.3.2. The schematic diagram of the Aerosol Generator setup is shown in Figure 3.4. Clean dry air was again produced by Filtered Air Supply 3074B and supplied to the Atomizer. The 3076 nominally generates particles with a size range of 0.01 to 2.0 µm with 0.3 µm count mean diameter. These sizes correspond to a 0.001 g/cm^3 NaCl and water solution concentration used in the Aerosol Generator. Since the majority of particles generated were too small to be detected by the sensors, a 0.1 g/cm^3 solution was used as higher concentrations result in larger sized particles. Aerosol leaving the atomizer passed through the Diffusion Dryer 3062 (TSI Inc.). Inside, silica gel removes excess water and the NaCl ions solidify to form particles before being introduced into the test chamber.

The sensors tested had various sampling intervals. The Fluke 985, Handheld 3016, SDS 021, DN7C3CA006, PMS A003, and PMS 7003 was set to take samples every five seconds. Although shorter sampling intervals were possible, readings were averaged over

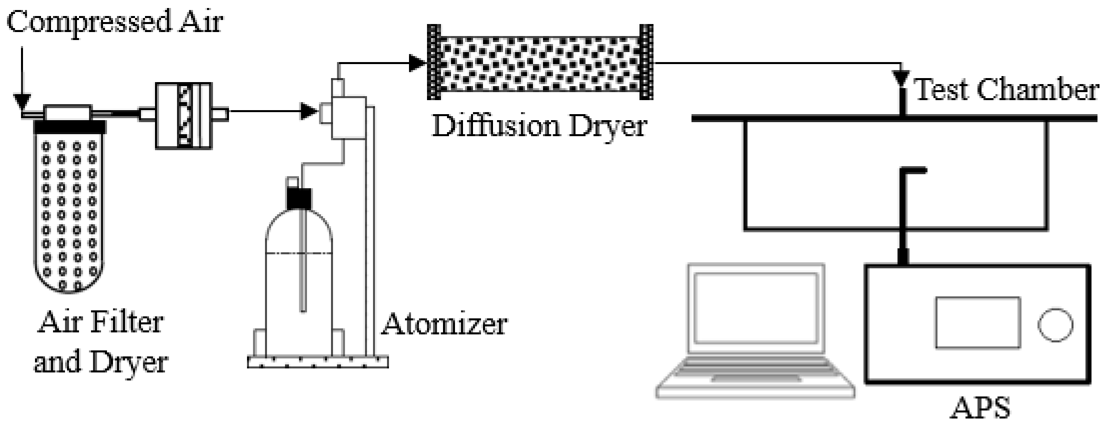

Figure 3.4: Schematic of NaCl particle generation.

a five second period to reduce noise. The Node and DC1100 Pro were sampled every ten seconds and one minute, respectively as those were the shortest intervals possible for the instruments. The sampling interval of APS was always set to match that of the sensor being tested. Timestamp synchronization between sensor and APS readings were essential to ensure accurate comparison of concentration outputs. Short sampling intervals introduce the least uncertainty. Timestamps could be offset with APS by as much as one half the sampling interval time.

The Fluke 985, Handheld 3016, and Node stored readings on internal memory. Since these devices also carried rechargeable batteries, no wiring was required for these sensors during testing. Data on these devices were retrieved after the experiments completed by using a computer to access the internal memory. The DC1100 Pro did not have on-board data storage or battery, so a wire feedthrough was made for connecting the sensor to computer via RS232 to USB adapter. Data was logged on the computer using manufacturer provided Dylos Logger v1.6 software. A second wire feedthrough was also made to supply power to the sensor. An Arduino Due board was used to read data from the SDS 021, PMS A003, PMS 7003, and DN7C3CA006 sensors, as they were not modules. The SDS 021, PMS A003, and PMS 7003 were connected to the serial pins of the Arduino. The DN7C3CA006 required an external high frequency square wave to operate, which was provided by the Arduino. The sensor represented concentration measured by a voltage output and this was read by a Due analog pin. Power required to operate these sensors were provided by the Arduino board. Code was written for the Arduino to collect data from the sensors, average readings over every five second interval, and send data to the computer via USB cable feedthrough. A Windows application program written using VB.NET was developed to read data sent by the Arduino, add timestamps, and save to an Excel file.

Evaluation of the Node in real indoor and outdoor environments was completed by another researcher. Testing took place in the month of March and at Hangzhou province in China. Measurements were made at three elementary schools: Jingyuan, Xiaosha No. 2, and Qiyuan. The experimental work lasted three days, and with each day, the sampling was completed at a different school. The Node and DustTrak II were operated by simply co-locating the devices, turning them on, and then allowing air to be sampled. No other equipment was involved with the experimental setup. Since the Node and DustTrak II provided readings every 30 and 10 seconds respectively, every three measurement of the Node was averaged in order to allow comparison. Both instruments stored readings on internal memory so microcontrollers were not required.

3.2.3 Assessment Procedure

In this work, two different laboratory tests were completed to evaluate the low cost sensors listed in Table 3.1. Accuracy was evaluated by comparing sensor readings to APS readings using road dust and NaCl particles. Precision was also evaluated by taking sensor measurements at a constant PM concentration. Accuracy of the Node was further evaluated in a real environment by comparison with the TSI DustTrak II.

To evaluate accuracy, the FBAG was first connected to the chamber and particles were generated. When the mass concentration measured by APS was at least 1,500 µg/m^3, the FBAG was disconnected. The concentration would then drop due to dust settling and being removed by APS. When the concentration dropped below 10 µg/m^3, particles were again reintroduced to at least 1,500 µg/m^3. This was repeated again for a total of three peak concentrations. The same procedure was followed using NaCl as the particle source. For analysis, data points were considered only when (i) the mass concentrations measured by APS was below 1,000 µg/m^3 and (ii) the aerosol generator was not connected. It has been reported Wang et al. (2015) that typical mass concentrations in highly polluted cities are slightly below 1,000 µg/m^3, so there was no need to evaluate the sensors above this threshold. On the lower end, data collection was terminated below 10 µg/m^3 since the World Health Organization's guideline for annual average concentration of PM$_{2.5}$ is 10 µg/m^3 (World Health Organization, 2005). In addition, when particles were generated it caused a highly uneven distribution in the chamber due to the inlet velocity. Thus measurements during these periods were discarded to reduce outliers.

Sensor precision was assessed by measuring output for a constant particulate concentration. Difficulty lied in maintaining a constant concentration with the FBAG or Aerosol Generator 3076. As a result, precision was only evaluated at a single particulate concentration. Tests were conducted in an open room indoor setting by operating sensors to sample the constant PM concentration of the room. Temperature and relative humidity were not measured since the objective of the study was not to determine their influence on the performance of the sensors.

Real environment tests in China were completed on three separate days, with each lasting approximately two hours. The same procedure was followed for each day at the three schools. The Node and DustTrak II was turned on and allowed to sample air while a person carried the devices in their hands from room to room. When in the classroom, the instruments were set on a table for a period of time, in which measurements for the indoor environment were made. Afterwards, a person would move the sensors to another classroom, and this was repeated a number of times. It was noted that sensors sampled air continuously between classrooms as they were being transported. During travel to the next room, the person may have to walk outside. This was the manner in which outdoor measurements were made as the two sensors were never placed on a surface outside and left to sample air for a period of time.

Unfortunately, the researcher did not note the specific times when the sensors were moved to another classroom. As a result, whether a measurement point is for an outdoor or indoor environment could not be identified. Nevertheless, all data from the three days were combined together to form one dataset. Accuracy was evaluated in the same manner as laboratory tests by plotting the Node versus DustTrak II response.

3.3 Results and Discussion

3.3.1 Linear Parametric Models

Except for the DN7C3CA006, data collected by all sensors were plotted against APS measurements for PM_{10} road dust, PM_{10} NaCl, $PM_{2.5}$ road dust, and $PM_{2.5}$ NaCl as shown in Figure 3.5. All plots show APS readings on the x-axis in the same concentration units as the sensor. The DN7C3CA006 only provided $PM_{2.5}$ readings and its output in voltage was plotted against both APS mass and number concentration as shown in Fig. 3.6. A total of 48 datasets was obtained for the eight sensors evaluated. A summary of the linear regression between all tested sensors and APS 3321 is shown in Table 3.2. Note that the DN7C3CA006 output was in voltage, and the units shown in the table indicate the APS concentration units for which the comparison was made.

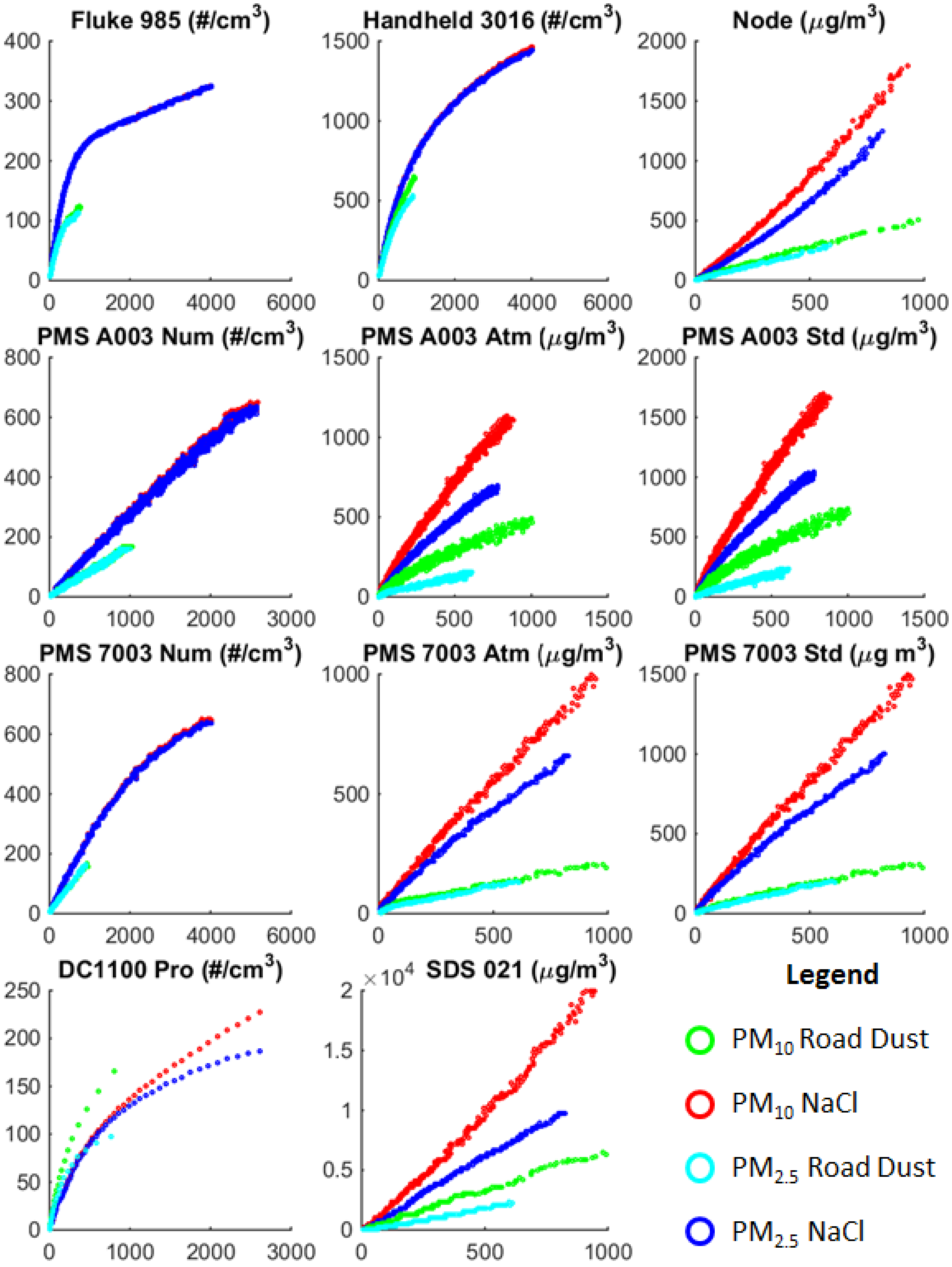

Figure 3.5: Plots of sensor concentration measurements versus APS.

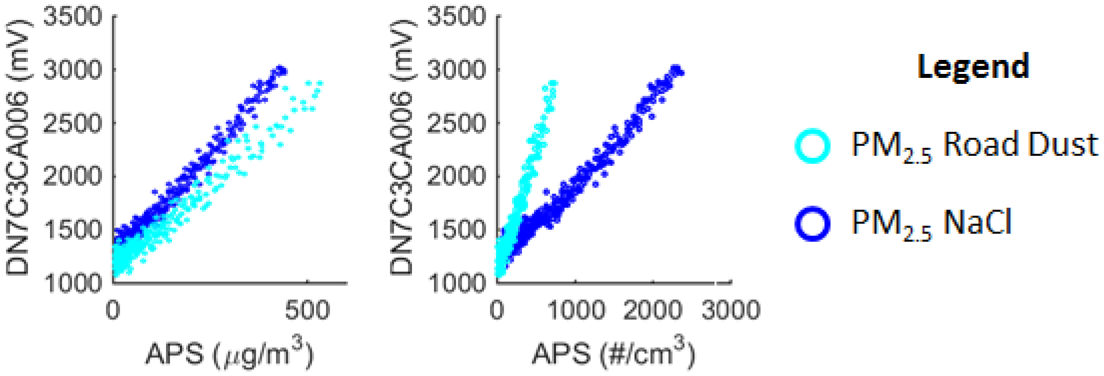

Figure 3.6: Plot of DN7C3CA006 voltage output versus APS.

It was noted that the DC1100 Pro, PMS 7003, and PMS A003, provided erroneous readings due variable overflow at PM concentrations below 1,000 μg/m^3. For the DN7C3CA006, the voltage output was saturated around 3,000 mV at concentrations below 1,000 μg/m^3. As a result these data points were removed. The PMS sensors transfer readings stored as 16 bit unsigned integers, which correspond to a maximum value of 65,536. This limit was reached by the 0.3 µm count channels before 1,000 µg/m^3, causing the erroneous readings. While the data type used by the DC1100 Pro was unknown, it is also speculated that memory space was an issue at high concentrations. If all DC1100 Pro measurements were divided by 100 (the two least significant digits were always zeros) the highest value is close to, but below the maximum value of 16 bit unsigned integers. Also, the experiments exceeded the manufacturer specified concentration limits for the Fluke 985 and Handheld 3016, but their readings were still included in the analysis.

The ideal sensor would closely match APS measurements regardless of particle source or size. Linear regression of the data would result in a line with slope approximately equal to one. The slope for real sensors represent the factor by which actual PM concentrations were overestimated and values were typically less than one, demonstrating an underestimation. The only exception was the SDS 021, which showed significant overestimation for all four particle source and size combinations. The Node, PMS A003 Std, and PMS 7003 Std

Table 3.2: Summary of linear regression between APS and tested sensors.

Sensor	**PM$_{10}$**		**PM$_{2.5}$**	
	Road Dust	NaCl	Road Dust	NaCl
Fluke 985 #/cm^3	$y = 0.18x + 16.5$ $R^2 = 0.93$	$y = 0.074x + 97.2$ $R^2 = 0.78$	$y = 0.17x + 16.6$ $R^2 = 0.91$	$y = 0.074x + 97.2$ $R^2 = 0.78$
Handheld 3016 #/cm^3	$y = 0.73x + 38.4$ $R^2 = 0.98$	$y = 0.38x + 236$ $R^2 = 0.92$	$y = 0.63x + 41.4$ $R^2 = 0.97$	$y = 0.38x + 237$ $R^2 = 0.91$
DC 1100 Pro #/cm^3	$y = 0.25x + 8.16$ $R^2 = 0.94$	$y = 0.09x + 26.8$ $R^2 = 0.94$	$y = 0.16x + 8.27$ $R^2 = 0.88$	$y = 0.08x + 30.7$ $R^2 = 0.90$
Node µg/m^3	$y = 0.53x + 7.51$ $R^2 = 1$	$y = 1.84x - 20.3$ $R^2 = 1$	$y = 0.46x + 3.62$ $R^2 = 1$	$y = 1.38x - 14.4$ $R^2 = 0.99$
PMS A003 Num #/cm^3	$y = 0.17x + 1.82$ $R^2 = 0.99$	$y = 0.26x + 10.3$ $R^2 = 1$	$y = 0.17x + 1.60$ $R^2 = 0.99$	$y = 0.26x + 10.7$ $R^2 = 1$
PMS A003 Std µg/m^3	$y = 0.78x + 27.4$ $R^2 = 0.97$	$y = 2.01x + 56.7$ $R^2 = 0.99$	$y = 0.38x + 4.45$ $R^2 = 0.98$	$y = 1.38x + 45.6$ $R^2 = 0.99$
PMS A003 Atm µg/m^3	$y = 0.51x + 24.8$ $R^2 = 0.97$	$y = 1.33x + 43.1$ $R^2 = 0.99$	$y = 0.24x + 7.51$ $R^2 = 0.96$	$y = 0.91x + 33.7$ $R^2 = 0.99$
PMS 7003 Num #/cm^3	$y = 0.17x + 4.48$ $R^2 = 1$	$y = 0.18x + 40.9$ $R^2 = 0.97$	$y = 0.18x + 4.17$ $R^2 = 1$	$y = 0.18x + 41.2$ $R^2 = 0.97$
PMS 7003 Std µg/m^3	$y = 0.34x + 12.9$ $R^2 = 0.98$	$y = 1.50x + 28.8$ $R^2 = 0.99$	$y = 0.34x + 6.21$ $R^2 = 0.99$	$y = 1.17x + 31.4$ $R^2 = 0.99$
PMS 7003 Atm µg/m^3	$y = 0.22x + 16.4$ $R^2 = 0.96$	$y = 0.99x + 26.0$ $R^2 = 0.99$	$y = 0.21x + 9.72$ $R^2 = 0.98$	$y = 0.77x + 24.9$ $R^2 = 0.99$
SDS 021 µg/m^3	$y = 6.99x - 64.3$ $R^2 = 0.99$	$y = 20.4x - 368$ $R^2 = 1$	$y = 3.69x - 89.8$ $R^2 = 0.99$	$y = 11.9x - 131$ $R^2 = 1$
DN7C3CA006 #/cm^3	N/A	N/A	$y = 2.06x + 1180$ $R^2 = 0.95$	$y = 0.74x + 1230$ $R^2 = 0.97$
DN7C3CA006 µg/m^3	N/A	N/A	$y = 2.85x + 1220$ $R^2 = 0.95$	$y = 3.85x + 1260$ $R^2 = 0.98$

showed overestimation for NaCl particles only. The PMS A003 Atm only overestimated PM$_{10}$ NaCl particles. Although measurements were never a one to one relation with APS, R$_2$ values were always greater than 0.78. The weakest linearity belonged to the Fluke 985, which is likely the result of the sensor measuring concentrations above its rated maximum. The results were what was expected of LLS based sensors: strong linear correlations with a reference instrument, but inaccurate PM concentration measurements.

Sensors also provided different readings for the same concentration (measured by APS) depending on particle source and particle size. Higher estimations were made for NaCl particles compared to road dust for the same APS concentration measurement, with the only exception being DC1100 Pro PM_{10} measurements. Also, higher estimations were made for PM_{10} particles compared to $PM_{2.5}$ for the same APS concentration measurement. The sensitivity can be seen by the plots in Fig. 3.5 not being coincident. To quantify sensitivity to particle source, the ratio of slopes for PM_{10} NaCl with PM_{10} road dust, or $PM_{2.5}$ NaCl with $PM_{2.5}$ road dust was found, as shown in Fig. 3.7. Sensitivity to particle size was analyzed by finding the ratios of road dust PM_{10} to road dust $PM_{2.5}$ and NaCl PM_{10} to NaCl $PM_{2.5}$, which is also shown in Fig. 3.7. Ratios close to one indicates that the sensor was insensitive to particle source or size.

For each data-set pair used to calculate a ratio, it was ensured that the maximum APS concentration (x-axis) measurements were equal for both sets before calculating the slopes i.e. observations from the data-set with higher maximum concentration were discarded until both data-sets had the same maximum concentration. This was completed to ensure an unbiased comparison between particle sources because the number concentration range evaluated for NaCl and road dust were not equal. At high concentrations, certain sensor responses become non-linear, so ratios would be biased if one of the slopes was calculated from a linear relation while the other was not. Thus the slopes shown in Table 3.2 were not necessarily used to calculate the results of Fig. 3.7.

Ratios close to one shows that the sensor was insensitive to particle source or size. The Node, PMS A003 Std, PMS A003 Atm, PMS 7003 Std, PMS 7003 Atm, and SDS021 showed significant dependence on particle source. NaCl readings for these sensors were 2.5 to 4.9 times greater than road dust for the same concentration measured by APS. The Handheld 3016 was the least sensitive to particle source as the ratio was 1.1 and 1.3 for PM_{10} and $PM_{2.5}$, respectively. The difference in measurements depending on particle source can be attributed to their different refractive indices and shapes. The

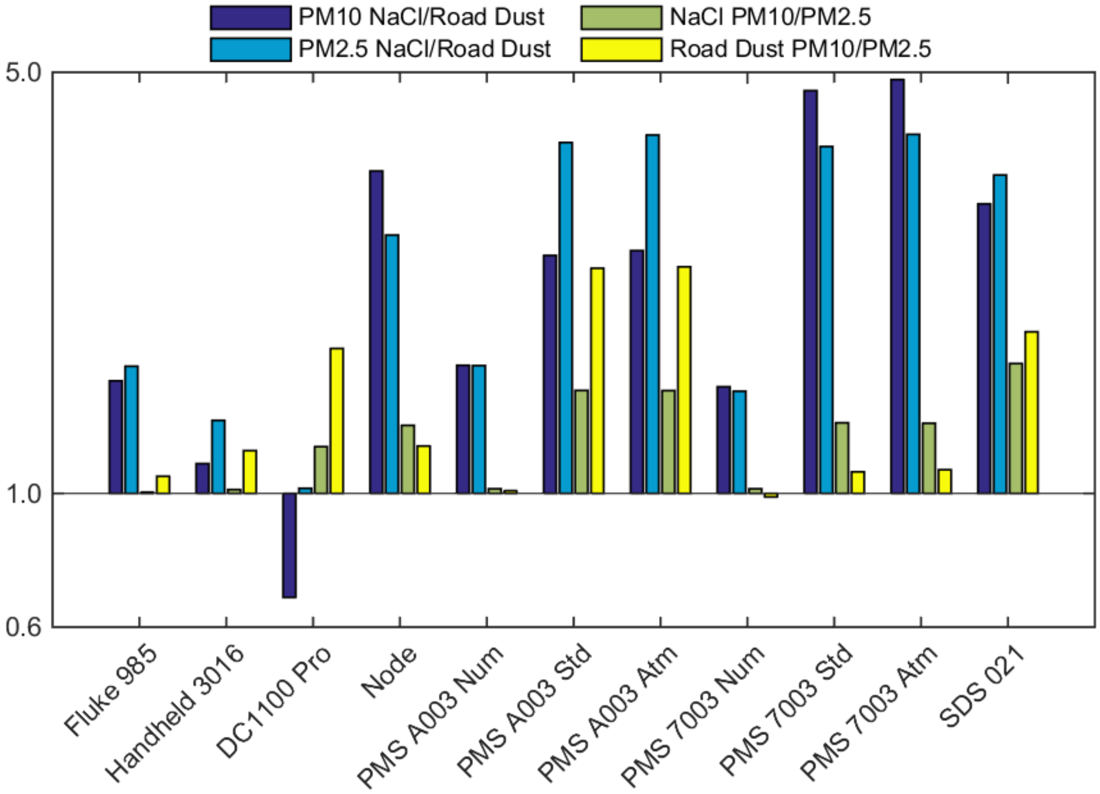

Figure 3.7: Slope ratios by particle material and size.

fact that NaCl readings were almost always greater than road dust for the same APS measurements (with one exception being DC1100 Pro PM_{10} readings) indicates the cause is due to particle physical properties. This is consistent with light scattering theory, which specifies that the intensity of scattered light is dependent on particle shape, refractive index, wavelength, scattering angle, and particle size. When different particle sources are tested, the refractive index and shape changes while other parameters remain constant. As a result, this is the likely cause of sensor sensitivity to particle source.

The PMS A003 Std, PMS A003 Atm, and SDS 021 showed significant dependence on particle size. PM_{10} readings for these sensors were 1.5 to 2.4 times greater than $PM_{2.5}$ for the same concentration measured by APS. The PMS A003 Num and PMS 7003 Num showed the smallest measurement bias depending on the particle size with ratios approximately equal to one. The discrepancy may be caused by smaller $PM_{2.5}$ particles not being detected as efficiently by the low cost sensors.

Sensor over or underestimation at low concentrations was constant. At higher concentrations, the underestimations grew for the Fluke 985, DC1100 Pro, and PMS 7003 Num. This was evident when the scatter plot comparing these sensors with APS was curved instead of a straight line. The decrease in counting efficiency may be caused by too many particles blocking laser light from reaching those behind it. This would cause the sensor to not be able to detect some particles as they would not be scattering light.

The results of the real environment test is shown in Figure 3.8. The Node slightly underestimated particle concentrations compared to the DustTrak II and correlations were strong with $R^2 = 0.955$. The two clusters of data points seen in the plot is due to the three test periods being discontinuous. The sensors were only evaluated in a small range of particle concentrations due to the inability to control PM concentrations in a real environment. Caution should be taken with the results of this experiment because the reference instrument is also a LLS based sensor. As previously noted, the technology can be inaccurate and sensitive to bias. These errors may not be revealed when both sensors in the experiment use the same measurement technique.

From this study, the PMS 7003 Num readings were found to be the most promising to use for air quality monitoring. Measurements were not significantly impacted by particle size or source as seen by the approximately unity ratios in Fig. 3.7. Although concentrations were underestimated by about a factor of five, a strong linear correlation existed with APS as R^2 values greater than 0.97. The reproducible and identifiable relation allows sensor measurements to be calibrated to match APS and provide more accurate readings. Surprisingly, the sensor was of low cost compared to the others tested, showing that price does not necessarily result in better performance.

Overall, LLS sensors show potential as long as they are properly calibrated in the

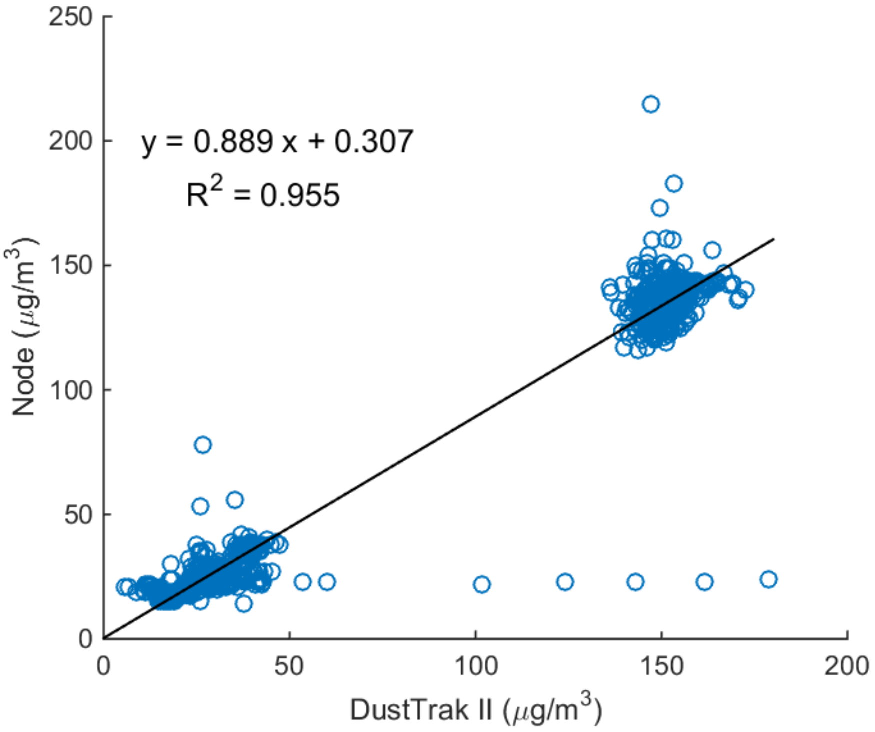

Figure 3.8: Results of the real environment test in China.

environment they will be used in. However, the public lack the technical means of accomplishing this. As a possible solution, manufacturers should develop multiple calibration curves in different environments where they expect their sensors to be used, such as outdoor urban or rural, indoor residential, or industrial settings. The consumer would then select the environment where they plan to use the sensor from the available choices. This strategy is already somewhat implemented in the PMS 7003 and PMS A003 sensors, as they have measurements for both a “standard” and “atmospheric” particle. Sensors should also be tested with as many different laboratory generated particle sources as possible, which will provide insight into the maximum sensitivity to particle source. This information will be useful when the sensor is used with an unknown particle composition as the sensor can provide the ”average” response of all sources and associated uncertainty. To provide consumers with further confidence, experimental setup, procedures, and results from calibrating the sensors should be made available.

Researchers with access to limited numbers of accurate instruments would be able to take greater advantage of low cost sensors, obtaining high spatial and temporal resolution data. By using a few accurate instruments with multiple low cost sensors in a large spatial area, the measurements of all low cost sensors can be related to actual concentrations as long as a low cost sensor and accurate instrument is located at the same point.

3.3.2 Precision

The sensor response in an ambient room is summarized in Table 3.3. The ideal sensor's average measurement would match APS and have zero relative standard deviation (RSD). Since the SDS 021, PMS 7003 Std, and PMS 7003 Atm reported average measurements of zero and had zero standard deviation, the RSD could not be calculated so an entry of "Error" is shown in the Table for these cases. For PM_{10}, the DC1100 Pro has the highest precision at low concentrations with a RSD of 10.7%. When considering $PM_{2.5}$, the DN7C3CA006 has the highest precision with 1.02% RSD. The Fluke 985 showed the lowest precision for both PM_{10} and $PM_{2.5}$.

Table 3.3: Summary of sensor means and RSDs in ambient room conditions.

Sensor	**PM$_{10}$** Mean	**PM$_{10}$** % RSD	**PM$_{2.5}$** Mean	**PM$_{2.5}$** % RSD	**Samples**
APS #/cm^3	3.50	22.4	3.50	22.5	183
APS µg/m^3	0.34	72.1	0.27	26.5	183
Fluke 985 #/cm^3	8.54	259	8.54	260	183
Handheld 3016 #/cm^3	6.64	16.7	6.61	16.7	183
DC 1100 Pro #/cm^3	0.56	10.7	0.52	8.06	53
Node µg/m^3	2.57	25.7	2.40	22.7	350
PMS A003 Num #/cm^3	7.50	12.0	7.49	12.0	183
PMS A003 Std µg/m^3	5.28	26.4	4.74	21.8	183
PMS A003 Atm µg/m^3	5.28	26.4	4.74	21.8	183
PMS 7003 Num #/cm^3	1.93	29.5	1.93	29.5	183
PMS 7003 Std µg/m^3	0.00	Error	0.00	Error	183
PMS 7003 Atm µg/m^3	0.00	Error	0.00	Error	183
SDS 021 µg/m^3	0.00	Error	0.00	Error	183
DN7C3CA006 mV	N/A	N/A	1975	1.02	183

3.4 Parametric Model Verification

3.4.1 Motivation

From the literature review conducted in Section 2.4, parametric models were always used to relate sensor measurements to an reference instrument, with the most common being linear functions. For a single independent variable, the ordinary linear regression model with n observations is described by:

$$Y = 1_n\alpha + \beta X + \epsilon \tag{3.1}$$

where

$$Y = \begin{bmatrix} y_1 \\ \vdots \\ y_n \end{bmatrix}, \quad X = \begin{bmatrix} x_1 \\ \vdots \\ x_n \end{bmatrix}, \quad \epsilon = \begin{bmatrix} \epsilon_1 \\ \vdots \\ \epsilon_n \end{bmatrix}$$

The matrix Y denotes the sensor measurements, α and β are unknown constants, 1_n is a vector of n ones, X is the reference instrument measurements, and ϵ is the random, non-observable errors (Groß, 2003). Assumptions of the model include:

1. X is not a random variable i.e. no relationship with ϵ.
2. $E(\epsilon) = 0$.
3. $Cov(\epsilon) = \sigma^2 I_n$ with $\sigma^2 > 0$ is a constant (homoscedasticity).
4. The elements ϵ_i of ϵ are normally distributed.
5. No autocorrelation of residuals.

While the APS is a well characterized particle counting instrument, there is still some error in its measurements. This may violate the first assumption as the variable x is disturbed by a non-observable random error. Assumptions 2 to 4 presumes the errors ϵ to obey certain rules, which may not be true. Homoscedasticity is especially of concern if the error is not constant over the evaluated range of PM concentrations. The last assumption requires that error terms of different observations should not be correlated with each other. Time series data is commonly autocorrelated, which applies to the case of PM measurements over time. It is possible that high concentrations affect the performance of LLS sensors due to dust deposition on the laser light source. In this scenario, measurements at a particular concentration will be different depending on whether the concentration was high or low in previous time periods.

Violation of any assumptions may lead to confidence intervals, insights, and model relating sensor to APS measurements being biased or misleading. The parametric approach assumes that x and y are related by a mean curve with a prespecified function i.e. line with slope and intercept. By fixing the function to a finite set of parameters, the model might be too restrictive or low-dimensional to fit unexpected features. These assumptions do not apply to non-parametric models, so it can be assured that an accurate estimation of the relationship is always obtained (Claussen, 2012).

Although non-parametric models are accurate, the parametric form is typically more effective if there is no statistical difference between the two. Also, the parametric model is more intuitive, immediately presents the relationship between independent and dependent variables, and easily communicated on paper. Thus it is desirable to compare the two models and use the simpler one if there are no differences (Claussen, 2012).

3.4.2 Procedure

Code was written using R programming language to solve for the non-parametric regression curve and perform bootstrap sampling of a particular dataset. The program result indicates whether there is a difference statistically between parametric and non-parametric regression. The code can be found in Appendix B.1 and its procedure is described in this section.

Similar to Equation 3.1, the non-parametric regression model is written simply as:

$$y = \hat{m}(x) + \epsilon \tag{3.2}$$

where $m(x)$ is an unknown regression function and only assumed to be ”smooth”. Using sensor and reference measurements X and Y respectively, the Kernel estimator method was used to determine this function:

$$\hat{m}(X) = \frac{\sum_{i=1}^{n} K(z_i) y_i}{\sum_{i=1}^{n} K(z_i)} \tag{3.3}$$

where

$$z_i = \frac{x_i - X}{h} \tag{3.4}$$

Here z_i is the scaled, signed distance between the ith x observation and value X for which an estimate is to be obtained. The bandwidth was chosen using cross validation techniques. The value is always greater than zero, depends only on the sample size n, and controls the amount of smoothing of the regression curve. $K(z)$ is the Kernel function which assigns greater weight to observations made at x_i's close to X. The Gaussian Kernel was used, which is simply the standard normal density function:

$$K(z) = \frac{1}{\sqrt{2\pi}} e^{-z^2/2} \tag{3.5}$$

The regression function is essentially a weighted average of data near x. Weights are assigned following a normal distribution, with higher weight given to observations close to x. The window size of data near x to be considered is controlled by the bandwidth h.

Using the parametric model $\hat{Y} = 1_n \alpha + \beta X$ determined from Section 3.3.1, the set of data $\{(x_i, \hat{y}_i)\}_{i=1}^{n}$ is obtained. This represents the response of the sensor that would have been obtained with observations X if it had been calibrated with the parametric model. Non-parametric regression was also performed on the data set as follows:

$$\hat{m}_{np}(X) = \frac{\sum_{i=1}^{n} K(z_i) \hat{y}_i}{\sum_{i=1}^{n} K(z_i)} \tag{3.6}$$

The test statistic T was then determined from the two non-parametric curves:

$$T = max[\{abs(\hat{m}(x_i) - \hat{m}_{np}(x_i))\}_{i=1}^{n}] \tag{3.7}$$

The error between sensor response and non-parametric curve was calculated as:

$$E = \{y_i - \hat{m}(x_i)\}_{i=1}^{n} \tag{3.8}$$

The mean μ, variance σ^2, and third moment of error γ was calculated for data set E. Then, the following set of non-linear equations was solved to determine A, B, and p:

$$Ap + B(1-p) = 0 \tag{3.9}$$

$$A^2p + B^2(1-p) = \sigma^2 \tag{3.10}$$

$$A^3p + B^3(1-p) = \gamma \tag{3.11}$$

A and B were the errors used for bootstrapping. The bootstrap was repeated 1,000 times with the first step generating an array of errors E_{bs} from a two point distribution. The length of E_{bs} was n, and the value of each element was either A or B with probability p and $1-p$, respectively. A set of y values for the bootstrap were calculated as follows:

$$Y_{bs} = \{\hat{m}_{np}(x_i) + E_{bs,i}\}_{i=1}^{n} \tag{3.12}$$

Using Y_{bs}, non-parametric regression was performed:

$$\hat{m}_{bs}(X) = \frac{\sum_{i=1}^{n} K(z_i) y_{bs,i}}{\sum_{i=1}^{n} K(z_i)} \tag{3.13}$$

Linear regression was also performed on the dataset Y_{bs} and X, resulting in the following model:

$$\hat{Y}_{bs} = 1_n \alpha_{bs} + \beta_{bs} X \tag{3.14}$$

This was followed by non-parametric regression of $\hat{Y}_{bs}$:

$$\hat{m}_{np,bs}(X) = \frac{\sum_{i=1}^{n} K(z_i)\hat{y}_{bs,i}}{\sum_{i=1}^{n} K(z_i)} \tag{3.15}$$

At the end of the jth bootstrap loop, the maximum difference between parametric and non-parametric curves were recorded:

$$T_j^* = max[\{abs(\hat{m}_{bs}(x_i) - \hat{m}_{np,bs}(x_i))\}_{i=1}^{n}], \quad j = 1, 2, ...1, 000 \tag{3.16}$$

After completion of bootstrapping, the 95th percentile Q_{95} of T^* was found. If the test statistic $T < Q_{95}$, then the null hypothesis was accepted as there was no difference between the two methods. Otherwise, the null hypothesis was rejected as a difference existed.

3.4.3 Results

When the analysis was completed for a dataset $\{(x_i, y_i)\}_{i=1}^{n}$, the null hypothesis was often rejected. As a result, every series in Figures 3.5 and 3.6 was split into two subsets $x_i < 100$ and $x_i >= 100$. This resulted in a total of 96 datasets, and each was analyzed separately. While measurements based on mass or number concentrations would be split up disproportionally, the value was chosen arbitrarily for the sole purpose of gaining deeper insight into the data. Table 3.4 lists the datasets for which the null hypothesis was accepted. All 74 other datasets were rejected.

The results of Table 3.4 show that the ordinary least squares (OLS) method is too restrictive for modeling LLS sensor and APS response. Often times the parametric model was rejected for both low ($x_i < 100$) and high ($x_i >= 100$) concentration ranges of a particular dataset. Occasionally, the linear model accurately described a dataset only for high or low concentration ranges.

Table 3.4: List of datasets with accepted null hypothesis.

Sensor	**Particle**	**PM**	x_i
Fluke 985 #/cm^3	NaCl	10	< 100
	NaCl	2.5	< 100
Handheld 3016 #/cm^3	NaCl	10	< 100
	NaCl	2.5	< 100
	Road Dust	10	< 100
	Road Dust	2.5	< 100
DC 1100 Pro #/cm^3	NaCl	10	< 100
	NaCl	2.5	< 100
	Road Dust	10	$>= 100$
	Road Dust	2.5	$>= 100$
Node µg/m^3	NaCl	10	< 100
PMS A003 Std µg/m^3	Road Dust	2.5	$>= 100$
PMS A003 Atm µg/m^3	Road Dust	2.5	$>= 100$
PMS 7003 Num #/cm^3	NaCl	10	< 100
	NaCl	2.5	< 100
PMS 7003 Std µg/m^3	Road Dust	10	< 100
SDS 021 µg/m^3	Road Dust	2.5	$>= 100$
DN7C3CA006 µg/m^3	NaCl	2.5	< 100
	NaCl	2.5	$>= 100$
	Road Dust	2.5	$>= 100$
DN7C3CA006 #/cm^3	Road Dust	2.5	< 100
	Road Dust	2.5	$>= 100$

The only datasets where the null hypothesis was accepted for both concentration range was DN7C3CA006 NaCl PM$_{2.5}$ (versus APS mass concentrations) and DN7C3CA006 Road Dust PM$_{2.5}$ (versus APS number concentrations). For this reason, the analysis was repeated without breaking up these two datasets to determine if a single linear model could represent the data. The result was the null hypothesis being rejected both times.

Overall, the analysis has indicated that a single linear model would not represent the relation between LLS sensor and APS response accurately. At best, linear models would only be sufficient for a portion of concentration ranges. However, this is likely inadequate because PM concentrations vary between the full 0 to 1,000 µg range evaluated. An accurate model valid over the full concentration range is necessary. Thus future studies and modeling of LLS sensor and reference instruments should explore the validity of non-linear parametric models using the same methods described in Section 3.4.2.

To illustrate the non-parametric curve, an example plot is shown in Figure 3.9 (left) for the PMS A003 Atm, Road Dust, $PM_{2.5}$, $x_i >= 100$ dataset. The experimentally observed data and parametric line is also shown. The null hypothesis for this dataset was accepted, so there was no difference between the parametric and non-parametric curves, statistically. A histogram of the corresponding bootstrap test statistic is also shown in Figure 3.9 (right). Each T^* occurrence was the result of a bootstrap sample and the vertical red line shows the maximum absolute error T. The histogram shows the error between parametric and non-parametric models of each bootstrap was less than the error T for the actual observed data, over 95% of the time.

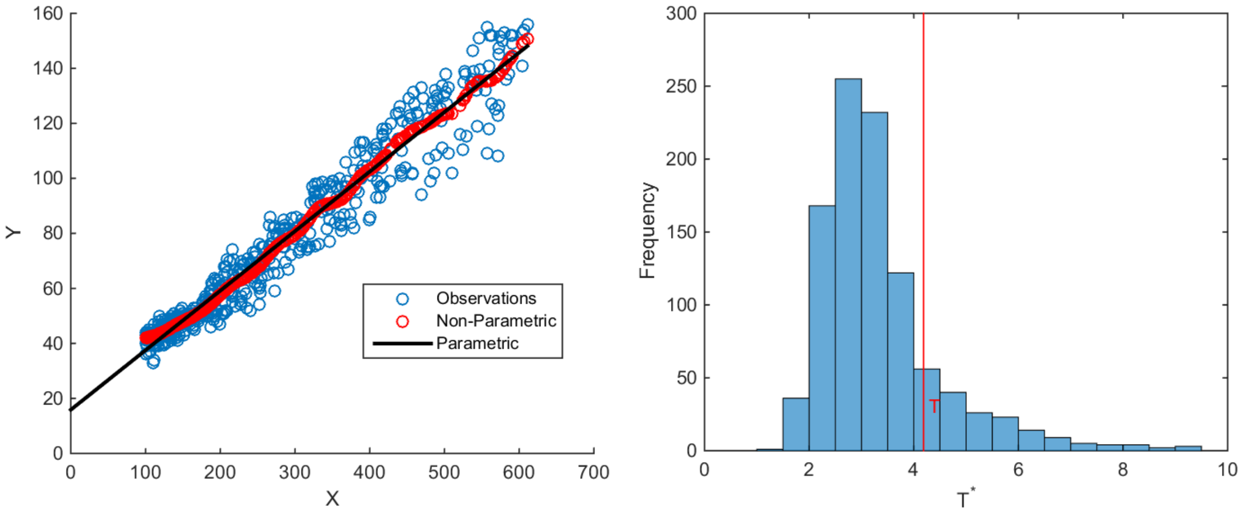

Figure 3.9: Verification results for PMS A003 Atm, Road Dust, $PM_{2.5}$, $x_i >= 100$ data.

An example parametric model whose null hypothesis was rejected is shown in Figure 3.10. This dataset corresponded PMS A003 Atm, Road Dust, $PM_{2.5}$, $x_i < 100$. As shown on the histogram on the right, the test statistic T was greater than all bootstrap T^* occurrences resulting in rejection.

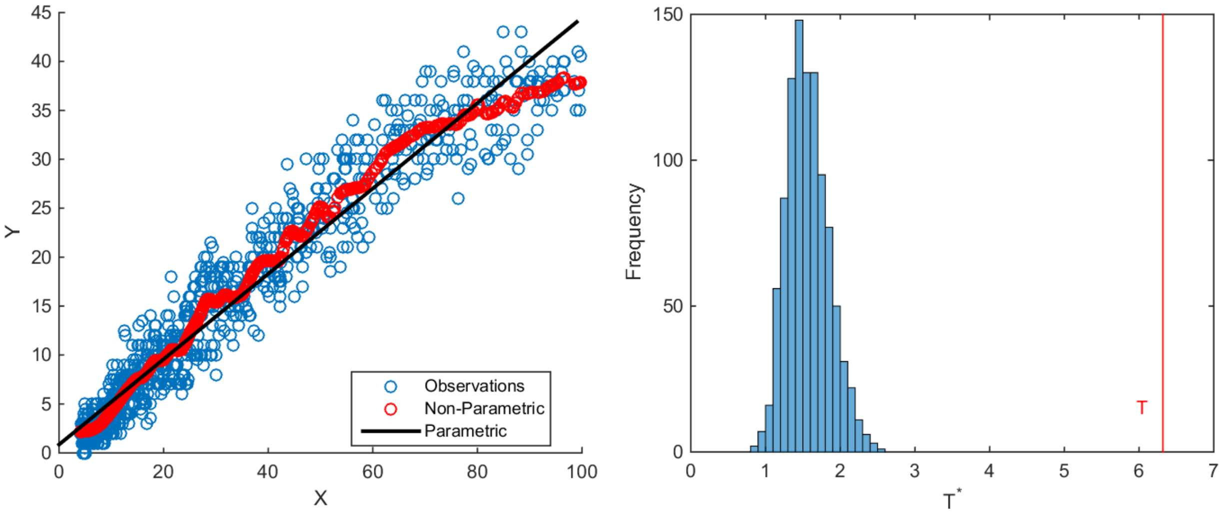

Figure 3.10: Verification results for PMS A003 Atm, Road Dust, $PM_{2.5}$, $x_i < 100$ data.

From a visual perspective, the parametric and non-parametric curves in Figure 3.9 coincided well. In Figure 3.10, predictions of the non-parametric curve frequently differed with the line by a much greater degree, especially in the range $80 < X < 100$. By using the parametric model, underestimations likely would be made for PM measurements in this concentration range. Additionally, the coefficient of determinations for the accepted and rejected parametric models were 0.95 and 0.94, respectively. Both values are extremely close and indicate strong correlations, which might lead one to judge both models as accurate without further information. By comparing with non-parametric models, more insight was gained and the parametric model was revealed to be less accurate. These results demonstrate the importance of verifying the OLS method to reduce bias when calibrating LLS based sensors.

3.5 Study of a Custom Portable Particle Counter

The market lacks accurate and well characterized low cost sensors as shown by the study completed. To address this need, the PPC was developed. Since the study showed LLS sensors performed with precision but lack of accuracy, the strategy was to properly calibrate an existing off the shelf sensor. Thus the PMS A003 sensor was chosen to be used in the PPC apparatus for its performance, high resolution, and small size. Details of the PPC's mechanical and electrical design can be found in Appendix C. This section describes the work completed to calibrate the instrument and results of its evaluation.

3.5.1 Assessment Procedure

As realized in the literature review and study completed, LLS sensors are sensitive to particle source. To better understand this disadvantage, the PPC was evaluated against the APS for several different real and laboratory generated particle sources. The aerosols tested with the PPC are as follows:

- Potassium chloride (KCl)
- Ammonium sulfate ($(NH_4)_2SO_4$)
- Magnesium sulfate ($MgSO_4$)
- NaCl
- Sucrose
- Road dust
- Residential
- Machine shop
- Outdoors

The setup and assessment procedure for comparing the PPC with APS in laboratory tests was similar to those described in Sections 3.2.2 and 3.2.3. As before, a 10 to 1,000 $\mu g/m^3$ concentration range was evaluated with three peaks. Ionic compound and sucrose particle sources were again generated with the atomizer. Evaluations with real aerosols were completed by simply operating the PPC and APS in the environment for at least 30 minutes. During testing at the residential setting, ambient PM concentration was increased by cleaning and dusting the room. The University of Waterloo Engineering Student Machine Shop was the location for evaluation in a machine shop setting, and outdoor testing was completed on campus.

The PPC was analyzed in-depth by also comparing measurements of each size bin, the median particle diameter, and geometric standard deviation (GSD) with APS. The GSD was calculated as follows:

$$ln\,\sigma_g = \left[\frac{\sum_1^6 F_i(ln\,d_{pi} - ln\,CMD)^2}{N-1}\right] \tag{3.17}$$

where F_i is the number concentration for the size bin, d_{pi} is the midpoint diameter of the size bin, CMD is the count median diameter, and N is the total particle concentration. Measurements from the six size bins provided by the PPC was used to calculate its measured GSD, while values for APS was provided automatically.

The low limit of detection (LLD) was also assessed for the PPC. The device was placed in the wooden chamber and clean air was supplied by the Filtered Air Supply 3074B for approximately 30 minutes. The LLD can then be calculated as:

$$LLD = \frac{3\sigma_{blk}}{k} \tag{3.18}$$

where σ_{blk} is the standard deviation of measurements taken at clean conditions and k is the slope of linear calibration curve with APS.

As previously noted, overflow frequently occurred with the PMS A003 during laboratory tests. Measurements would restart at zero as PM concentrations continued to increase and eventually overflow again. It was later realized by adding 65,535 to values of the first overflow, and 2×65,535 to the second overflow, a continuous curve could be obtained for PMS A003 measurements over the entire 0 to 1,000 µg/m^3 range. This adjustment was made for all tests completed in this section.

3.5.2 Results

A plot of PPC versus APS number concentration measurements for PM_{10} is shown in Figure 3.11 (left) with all tested particle sources. Figure 3.11 (right) shows a magnified view of the left plot to better show the test data for real particle sources. Note that the same legend applies for all plots in this section. Due to difficulties in controlling PM levels of real particle sources, only a low concentration range could be evaluated. A summary of the linear regression is shown in Table 3.5. Due to non-linearity observed with atomizer generated particles, linear regression was also performed on a subset of data where APS measurements were less than 1,000 particles/cm^3. In this interval the response was observed to be linear.

The standard deviation of measurements taken at clean conditions σ_{blk} was calculated to be 0.197 for PM_{10} particle counts. Since the calibration slope k can be various values depending on the particle source, the LLD was calculated for every particle source tested and shown in Table 3.5. Slopes from the $x < 1000$ column was used for the calculation. Excluding the outdoors dataset, the average LLD was 1.12 particles/cm^3.

The PPC does not seem to be as sensitive to particle source compared to just the PMS A003 sensor; the relation between PPC and APS response was quite similar regardless of particle source. Both laboratory generated and real aerosol curves were similar. The slopes for atomizer generated particles only ranged from 0.32 to 0.36 when considering the full range of data in Table 3.5. The slope for road dust particles was 0.55, and the large discrepancy can be attributed to the non-linear curve of atomizer generated particles. When considering the subset of data where $x < 1000$, the non-linearity of atomizer generated particles is eliminated, and slopes ranged from 0.46 to 0.59 for all

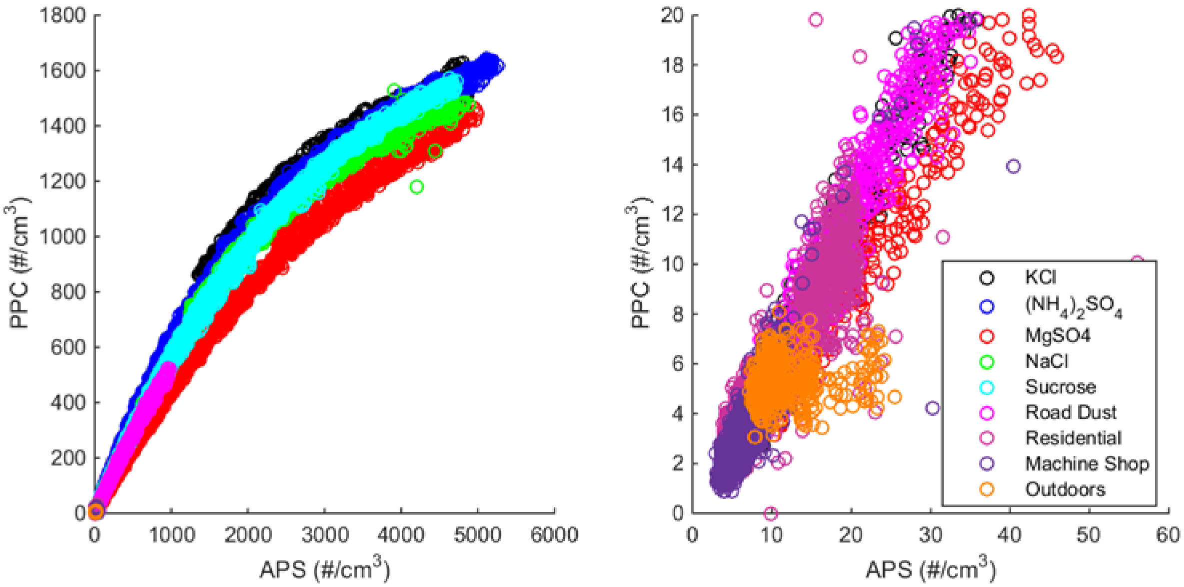

Figure 3.11: Plot of PPC versus APS for PM_{10} (left) and a magnified view (right).

Table 3.5: Summary of linear regression between the PPC and APS and calculated LLD.

Particle Source	**All Data**		$x < 1000$		**LLD (#/cm^3)**
	Regression	R^2	Regression	R^2	
KCl	$y = 0.36x + 110$	0.95	$y = 0.59x + 6.85$	0.99	0.99
$(NH_4)_2SO_4$	$y = 0.34x + 144$	0.95	$y = 0.59x + 9.25$	0.98	1.00
$MgSO_4$	$y = 0.32x + 66.9$	0.98	$y = 0.46x + 3.48$	0.997	1.30
NaCl	$y = 0.35x + 129$	0.95	$y = 0.56x + 14.7$	0.997	1.05
Sucrose	$y = 0.35x + 138$	0.97	$y = 0.56x + 15.6$	0.99	1.05
Road Dust	$y = 0.55x + 4.39$	0.997	See All Data		1.07
Residential	$y = 0.51x + 0.44$	0.79	See All Data		1.16
Machine Shop	$y = 0.43x + 0.59$	0.56	See All Data		1.36
Outdoors	$y = 0.037x + 4.87$	0.029	See All Data		15.9

aerosol sources. For responses in the real environment, the scatter points can be seen to line up well with laboratory generated particles as shown in Figure 3.11 (right). Except for the Outdoors environment, slopes for Residential and Machine Shop lied within those for laboratory generated particles. However, it should be noted that the concentration range evaluated for real aerosols was extremely small. While the current results looks promising in that there is little sensitivity between real and laboratory aerosols, they may change when the PPC is evaluated over a larger range.

To further illustrate the lower sensitivity to particle source, road dust and NaCl data for the PMS A003 (from Section 3.3.1) and PPC were plotted in Figure 3.12. The road dust and NaCl curves for the PPC were almost coincident, while they were much further apart for the PMS A003. The lower sensitivity can be attributed to the pump included in the PPC. Road dust particles are larger than NaCl on average, so the small fan of the PMS A003 may not provide enough vacuum to sample aerosol without bias.

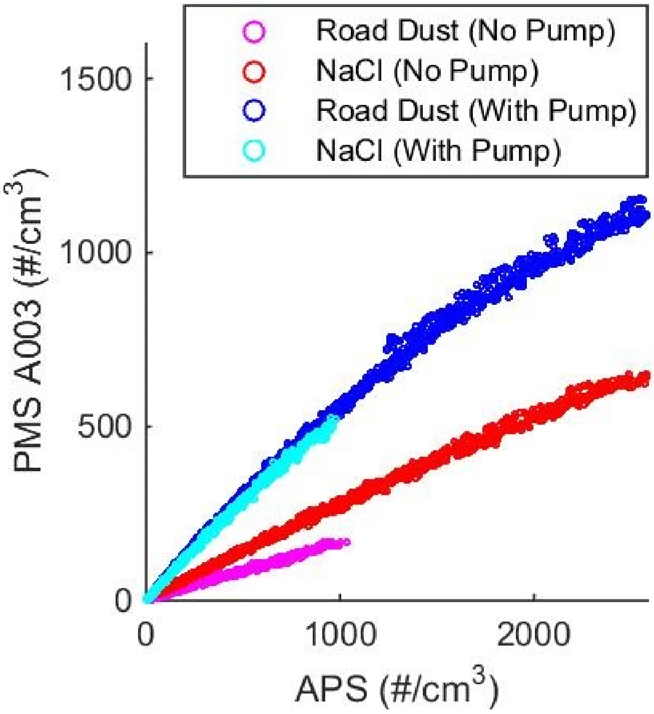

Figure 3.12: Effect of the pump on raw sensor measurements.

The NaCl and road dust curves were much more similar for the PPC compared to just the PMS A003 sensor. Recalling Table 3.2, the PMS A003 slopes for PM_{10} road dust and NaCl were 0.17 and 0.26, respectively. For the PPC, PM_{10} road dust and NaCl slopes were closer at 0.55 and 0.56, respectively. The reason is most likely due to the PPC pump allowing a greater volume of air to be sampled. Since road dust particles are larger than

NaCl on average, a greater fraction of particles may not have been drawn into the PMS A003. By reducing sensor sensitivity to particle source, a higher confidence interval is obtained when it is unknown. Despite a improvement, measurement uncertainty is still high if the particle source is unknown. For a given APS concentration, there is still a large range of possible PPC responses.

At higher number concentrations as obtained by the atomizer generated particles, the underestimation by the PPC increases. Non-linear regression should be used to calibrate the sensor if a high rated concentration limit for the PPC is desired. Although a low correlation was observed for outdoor particle sources, the cause is likely due to the low concentration range evaluated. Evaluation of the PPC in more polluted environments and wider concentration range should be completed. With the current information available, it is known that the PPC response is not sensitive to real or laboratory generated particles. Thus the curve for real aerosols can be extrapolated for higher concentrations using data from the laboratory generated aerosols.

The PMS A003 was one of the highest resolution LLS sensors evaluated as it outputs number concentration measurements in six size bins. As a result, further analysis was completed to determine if the measurement of each size bin is comparable to APS. Figure 3.13 shows a comparison of PPC versus APS measurements broken down by each of its size bins. Note that by summing the first five size bins, the PM_{10} plot shown in Figure 3.11 is obtained.

The PPC's measurements by size bins shows higher sensitivity to particle source compared to PM_{10}. The most extreme can be seen with the 5.0-10.0 and >10.0 µm size bins, where slopes essentially range from zero for residential to infinity for road dust. The PPC frequently did not detect larger sized particles in real environments. It also appeared to mistakenly size some road dust particles larger than they actually were as the APS did

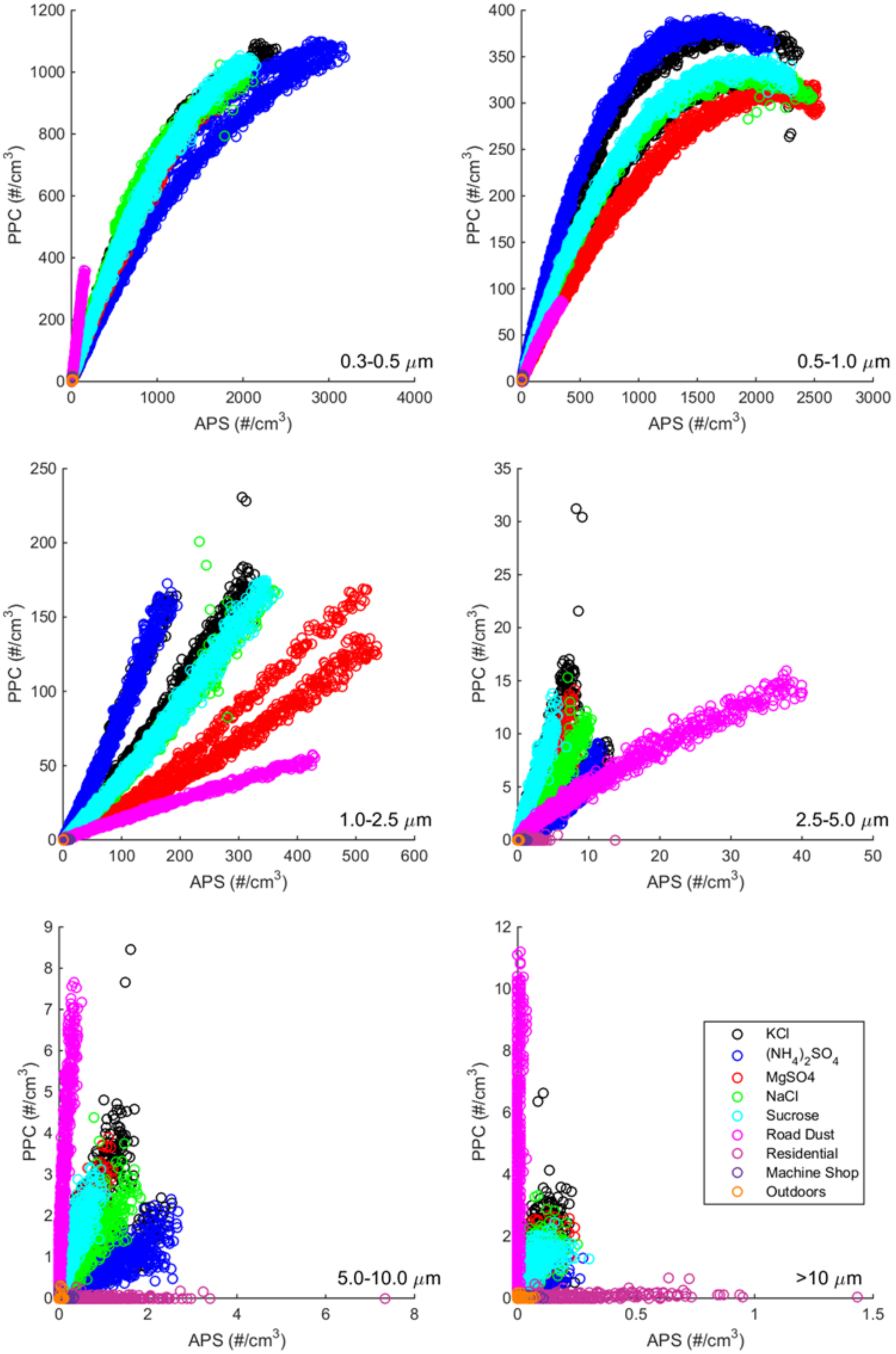

Figure 3.13: Plot of PPC versus APS measurements by size channel.

not detect any greater than 5.0 µm. The 0.3-0.5 µm channel appeared to show the least sensitivity to particle source. Interestingly, at high concentrations, PPC measurements begin to decrease as actual particle concentrations continue to increase for the 0.5-1.0 µm bin. This further complicates calibration as for a given PPC measurement, there can be two possible real concentration. Since the 0.3-0.5 µm channel exhibited the least particle source sensitivity and contained the greatest concentrations, the bias of the larger size channels become hidden when expressing measurements as PM_{10}. The results show that the PMS A003 does not have as high of a resolution as it appears due to an inability to size particles correctly.

The median particle diameter measured by the PPC was always 0.4 µm (midpoint diameter of the due to its limited resolution. Surprisingly, the value ranged from 0.64 to 4.25 µm for the APS, which was always greater and within the detection limit of the PPC. Nonetheless, the GSD was calculated for the PPC using this value and a comparison with APS is made in Figure 3.14. The analysis provides further insight into the ability of the PPC to measure PSD using its six channels.

For laboratory generated particles, the PPC overestimated GSD compared to APS. By visual inspection, all curves for atomizer generated particles were close, while road dust was shifted to the left. A correlation did not appear to exist for real aerosols, which was likely due to the low concentrations evaluated. The results show that the PPC is capable of detecting changes in particle GSD, but due to limitations on resolution and accuracy is not able to predict the correct value. In addition, a dependence on particle source can be seen with the GSD comparison with APS.

The relation between PMS A003 number and mass concentration measurements was also investigated. The manufacturer did not disclose this information due to confidentiality reasons. Assuming spherical particles, mass concentration M is related to number

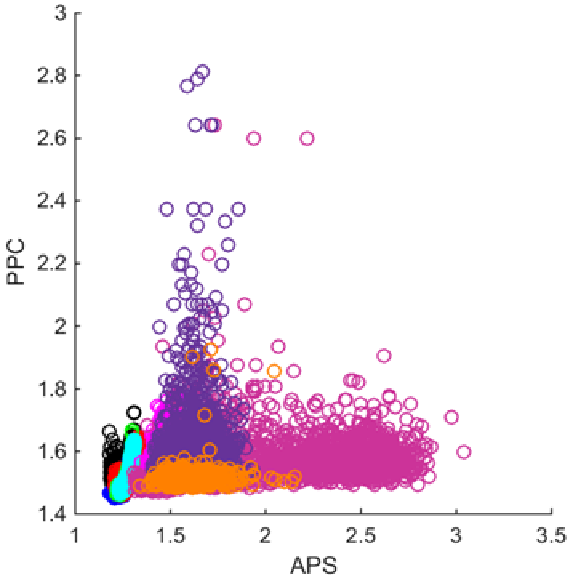

Figure 3.14: Plot of PPC versus APS GSD (left) and a magnified view (right).

concentration N by the following equation:

$$M = \frac{1}{6}\pi\rho_p \sum_{i=1}^{n} N_i d_{m(i)}^3 \tag{3.19}$$

where ρ_p is the density of the particle, n is the number of size bins, N_i is the number concentration of the ith size bin, and $d_{m(i)}$ is the midpoint diameter of the ith size bin. For every PPC sample, the measured ”Atmospheric” PM_{10} mass concentration was plotted against measured PM_{10} volume concentration i.e. using Equation 3.19 and setting $\rho_p = 1$. The results are shown in Figure 3.15.

The results of Figure 3.15 show that Equation 3.19 was not used to calculate PM mass concentration from measured number concentrations. If the method was used, the plot obtained would have been a straight line with slope equal to the particle density assumed. Also, different curves were obtained depending on particle source. The user does not input a density for the PMS A003 to use in calculations, so all curves should be coincident. However, all curves for atomizer generated particles were similar, suggesting

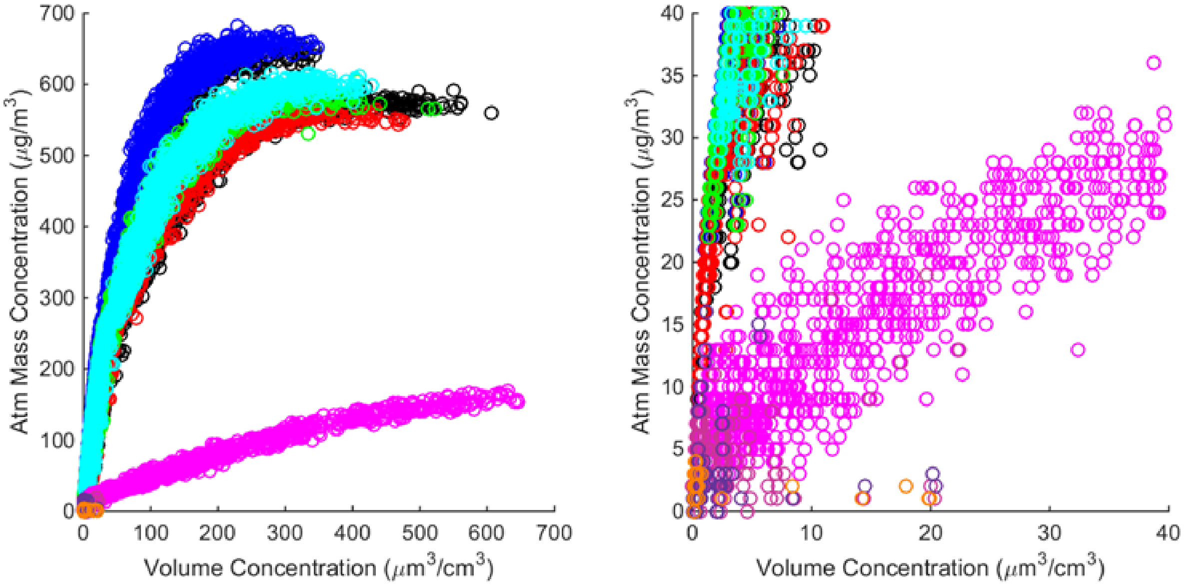

Figure 3.15: Plot of PPC mass versus volume concentration (left) and a magnified view (right).

different weights are placed on the size bins for calculating volume concentration. To confirm mass concentration measurements made by the APS, the same procedure was completed using its measured mass and number concentrations. When plotted, a perfect straight line was obtained, confirming that Equation 3.19 was used by APS software. Thus to reduce uncertainty, mass concentrations should be obtained from the PPC by first calibrating number concentration and applying Equation 3.19, instead of calibrating its mass concentration output directly.

3.5.3 Calibration

The PPC was calibrated for both number and mass concentration measurements. Size range wise, only PM_{10} and $PM_{2.5}$ was calibrated, giving a total of four models. Size bins were not calibrated individually due to the poor performance determined in Figure 3.13. By lowering the resolution to PM_{10} and $PM_{2.5}$, the effects of particle source sensitivity was reduced. A high resolution was not critical since many air pollution standards set targets based on PM_{10} and $PM_{2.5}$.

Although the manufacturer specified units for PMS A003 number concentrations measurements, they were not considered for the calibration. Raw sensor readings were treated as a unitless signal, which once substituted into the calibration function, yields the correct particulate concentration in #/cm^3 or µg/m^3. This strategy was selected since a repeatable relationship was observed between LLS sensor responses (regardless of units) and APS measurements.

It is important to note that calibration of the PPC is specific to a particular mechanical design. Higher flow rates through the PMS A003 sensor result in raw readings of greater magnitude, for the same ambient particulate concentration. Unlike a bare sensor, the housing, pump, and tubing of the PPC affects the flow rate through the PMS A003 which in turn alters the response. Changing any of these mechanical aspects would require an entirely different calibration model.

Number Concentration

As determined from Section 3.4.3, linear models do not accurately describe the relationship between LLS sensors and APS. Two third degree polynomials relating PPC to APS PM_{10} and $PM_{2.5}$ number concentrations were compared with the non-parametric regression model following the same method described in Section 3.4.2. The results indicated that the parametric and non-parametric models were equivalent statistically, so the polynomial was used for calibration.

Data from all tested particle sources were combined into one large dataset for the regression. A disadvantage of this method is that more weight is given to atomizer generated particles as more tests were conducted using this source. These types of particles may not reflect the response of real aerosols as closely. However, there were no alternative strategies to obtain data for real aerosols over a wider concentration range with the limited resources available. Also, since each data point in the regression is treated equally, more weight is assigned to particle sources with larger number of observations. However, this was considered negligible compared to the previous bias.

The third degree polynomial fitted to the PM_{10} and $PM_{2.5}$ data is shown in Figure 3.16. A summary of the output statistics is shown in Figure 3.6. The coefficients correspond to an equation of the form $y = \beta_3 x^3 + \beta_2 x^2 + \beta_1 x + \beta_0$, and the confidence interval is 95%. Generally, PM_{10} and $PM_{2.5}$ calibration curves for number concentration are similar since only a small fraction of particles are between 2.5-10.0 µm diameter count wise.

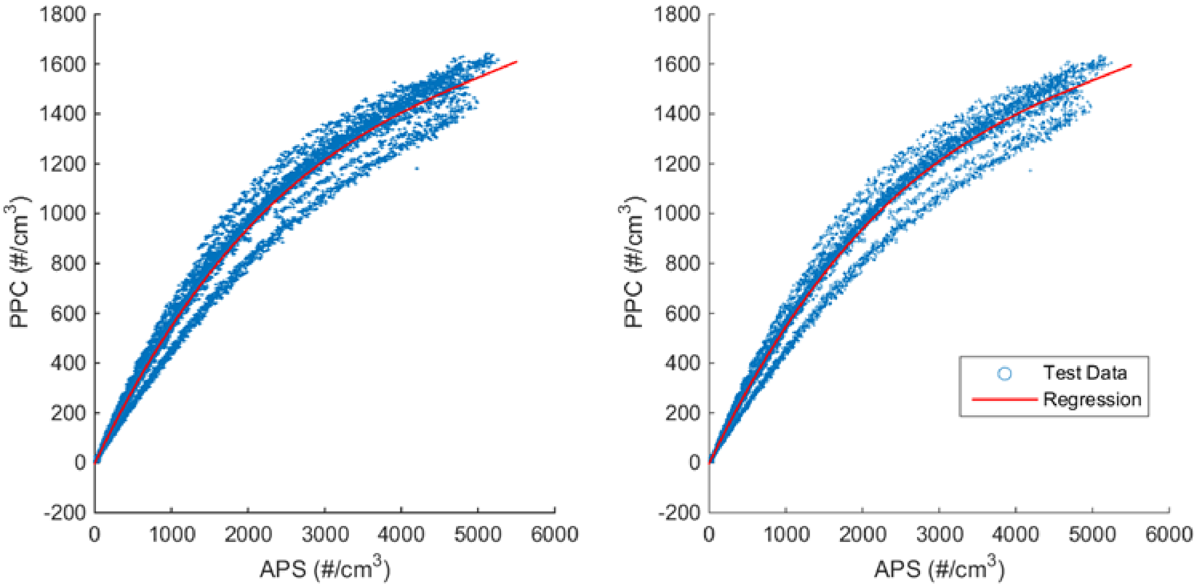

Figure 3.16: Calibration curve for all PM_{10} (left) and $PM_{2.5}$ (right) data.

To calibrate readings from the PPC to match more closely with APS, the inverse function of the polynomial curves were found. The equation can be implemented in a microcontroller to evaluate raw PPC readings and provide more accurate estimates. Figure 3.17 shows the number concentration results that would have been obtained from the experiments had the calibration been applied. The 95% prediction interval is for the calibrated PPC and APS measurement dataset. The PPC response is linear for all

Table 3.6: Summary of number concentration regression statistics.

Statistic	**PM$_{10}$**	**PM$_{2.5}$**
R^2	0.99	0.99
RMSE	44.1	44.2
Coefficients		
x^3	$5.94 \times 10^{-9} \pm 3.10 \times 10^{-10}$	$5.90 \times 10^{-9} \pm 3.14 \times 10^{-10}$
x^2	$-9.55 \times 10^{-5} \pm 2.03 \times 10^{-6}$	$-9.57 \times 10^{-5} \pm 2.05 \times 10^{-6}$
x	$0.64 \pm 3.35 \times 10^{-3}$	$0.64 \pm 3.37 \times 10^{-3}$
Intercept	-2.25 ± 0.99	-2.21 ± 1.00
p-value	0	0

concentration ranges and a closer one to one match with APS is obtained, illustrated by the 45° line.

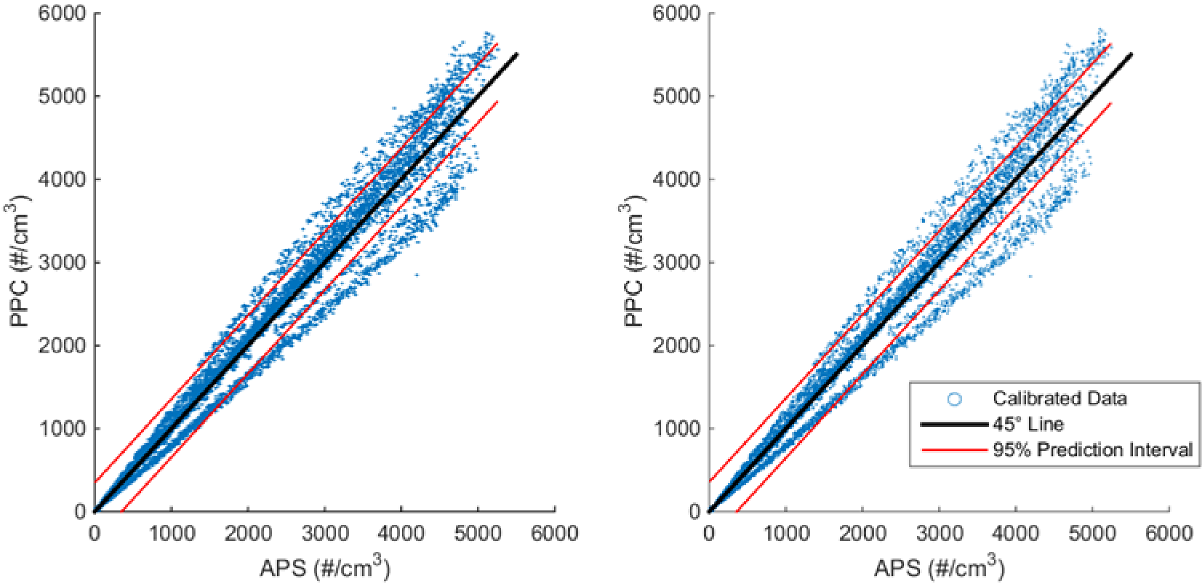

Figure 3.17: PM$_{10}$ (left) and PM$_{2.5}$ (right) number concentration of a calibrated PPC.

Even after calibration, the 95% prediction interval is quite large as values can range by 700 and 720 particles/cm^3 for PM$_{10}$ and PM$_{2.5}$, respectively. The wide range of possible responses for a given APS measurement is due to multiple particle sources being averaged in the model. A more specific curve for a particular particle source would not be representative of all the potential end uses of the PPC. It is difficult to predict the particles in an environment, so the developed model gives the best estimate without this knowledge. The interval can be reduced by evaluating the PPC with APS in the specific application and performing the same calibration procedure. However, caution should still be exercised because particle sources in an environment can change over time.

Mass Concentration

Raw mass concentration measurements from the PMS A003 were not calibrated with APS since the method by it was derived from number concentration was unclear. Instead, number concentration values from the size bins (predictors) were correlated with APS mass measurement using multi-variable linear regression. The GSD measured by PPC was not used as a predictor since there did not appear to be a correlation with APS in Figure 3.14. Particle density was included as an independent variable since it is a known predictor and was also confirmed to yield more accurate predictions. While the densities of laboratory generated particles were well documented, the property was unclear for real aerosols. As suggested by Tuch et al. (2000) and Weijersa et al. (2004), a density of 1.65 g/cm^3 was used based on experimental findings. The same densities were used by APS to calculate its mass concentration estimates.

From Equation 3.19, APS PM$_{10}$ and PM$_{2.5}$ mass measurements should be related to PPC size channels by the regression model:

$$M_{10} = \beta_5 \rho_p x_5 + \beta_4 \rho_p x_4 + \beta_3 \rho_p x_3 + \beta_2 \rho_p x_2 + \beta_1 \rho_p x_1 + \beta_0 \tag{3.20}$$

$$M_{2.5} = \beta_3 \rho_p x_3 + \beta_2 \rho_p x_2 + \beta_1 \rho_p x_1 + \beta_0 \tag{3.21}$$

where x_1, x_2, x_3, x_4, and x_5 are the 0.3-0.5, 0.5-1.0, 1.0-2.5, 2.5-5.0, and 5.0-10.0 µm PPC size channel measurements, respectively. β_i's are the model coefficients, and ρ_p is the particle density. However, it was unknown how the PMS A003 determined measurement values for each size bin, and whether interactions between size channels existed. As a result, a linear regression model with interactions was selected for the calibration i.e. model contains an intercept, linear terms, all products of pairs of distinct predictors, and no squared terms (The MathWorks Inc., 2017). The more complex model was found to have a lower root mean squared error (RMSE) and higher R^2 values.

Using the developed model, calibrated mass concentration measurements can be obtained from PPC number concentrations. Again, the equations can be easily implemented in a microcontroller to provide the user with more accurate estimates. Figure 3.18 shows the mass concentration results that would have been obtained from the experiments had the calibration been applied. The 95% prediction interval is for hte calibrated PPC and APS measurement dataset.

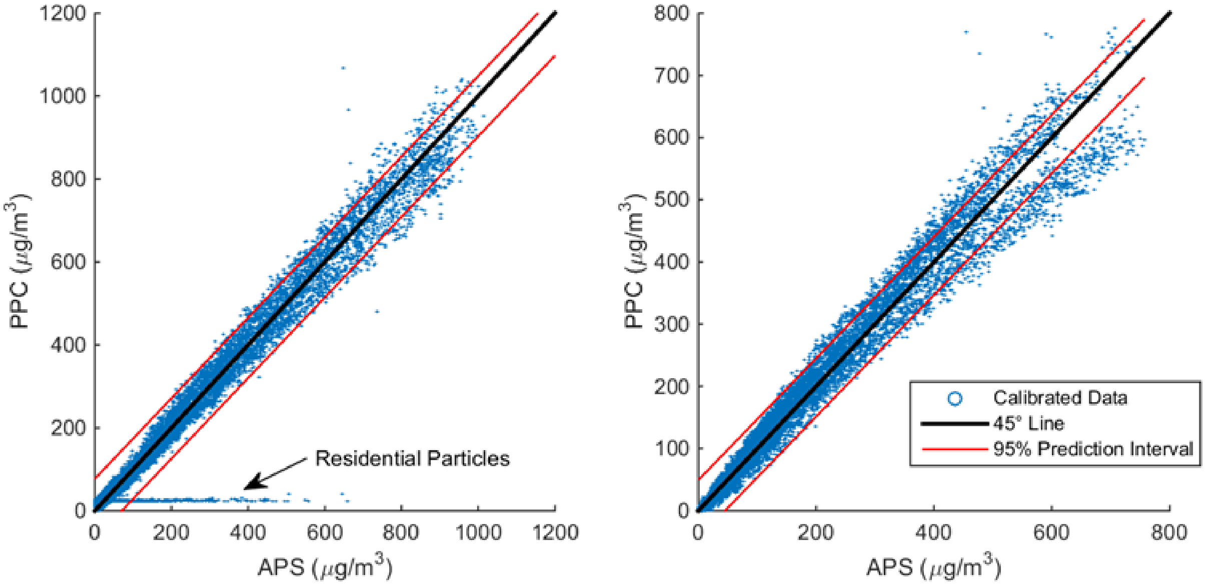

Figure 3.18: PM_{10} (left) and $PM_{2.5}$ (right) mass concentration of a calibrated PPC.

A summary of the regression statistics is shown in Table 3.7. The calibrated PPC reading is obtained by a summation of the coefficient and predictor product in the table. The coefficient confidence interval is 95%. Although the x_5 and $x_5\rho_p$ terms in the PM_{10} model were flagged as insignificant with p-values greater than 0.05, it was still included as removing the terms did not change any statistics. The PPC response was linear for all concentration ranges and matched well with APS, as illustrated by the 45° line.

Table 3.7: Summary of mass concentration regression statistics.

Statistic	**PM_{10}**	**$PM_{2.5}$**
R^2	0.97	0.98
RMSE	37.7	24.2
Coefficients		
$x_5\rho_p$	6.97 ± 11.2	
$x_4\rho_p$	8.07 ± 5.63	
x_4x_5	4.33 ± 2.06	
$x_3\rho_p$	-12.3 ± 2.10	-12.8 ± 0.97
x_3x_5	-3.10 ± 0.78	
x_3x_4	0.74 ± 0.27	
$x_2\rho_p$	-11.3 ± 2.33	-12.2 ± 0.95
x_2x_5	-2.16 ± 0.83	
x_2x_4	0.76 ± 0.22	
x_2x_3	-0.018 ± 0.01	$0.00243 \pm 9.38 \times 10^{-4}$
$x_1\rho_p$	5.68 ± 1.12	6.02 ± 0.46
x_1x_5	1.11 ± 0.41	
x_1x_4	-0.43 ± 0.11	
x_1x_3	$0.011 \pm 1.78 \times 10^{-3}$	$-7.86 \times 10^{-3} \pm 2.36 \times 10^{-4}$
x_1x_2	$2.64 \times 10^{-4} \pm 9.12 \times 10^{-5}$	$136 \times 10^{-4} \pm 3.89 \times 10^{-5}$
ρ_p	-32.8 ± 2.46	-10.2 ± 1.52
x_5	-4.85 ± 26.9	
x_4	34.4 ± 13.1	
x_3	28.6 ± 4.02	35.2 ± 2.00
x_2	26.7 ± 4.54	22.4 ± 2.00
x_1	-13.2 ± 2.17	-11.2 ± 0.96
Intercept	78.9 ± 4.75	18.7 ± 2.97
p-value	0	0

Despite the PPC's low sensitivity to particle source, the prediction interval ranged by 150 and 90 µg/m^3 for PM_{10} and $PM_{2.5}$, respectively. Also, PM_{10} residential aerosols could not be calibrated as seen by the annotation in Figure 3.18 (left). The reason is likely due to the PPC being unable to draw in and detect the large particles. The method of generating particles through cleaning and dusting the surroundings may also play a role in producing large agglomerates. As seen from Figure 3.13, the majority of residential aerosols were greater than 5.0 µm in diameter and no response was obtained by the PPC. This outlier can be seen to cause a bias in the prediction plot. Nevertheless, the calibrated measurements are a definite improvement from the raw readings.

Chapter 4
Conclusions and Future Work

4.1 Research Completed

Studies evaluating the performance of LLS sensors were reviewed. It was found that parametric models were always used to correlate sensors with a reference instrument, which may lead to bias if certain assumptions are violated. Also, sensor measurements were generally found to be inaccurate and in need of calibration. While the sensor response for a particular particle source studied was presented in the reviewed literature, a method to ensure measurements were accurate for all end uses was not provided. This was determined to be a pressing issue for LLS based sensors due to their dependence on particle source. Thus the objective of this work was to experimentally evaluate multiple LLS sensors against a reference instrument and properly model the relationship. Using the knowledge gained, a custom apparatus for PM monitoring would then be developed.

Eight commercial LLS particle sensors were randomly selected for the evaluation. The APS 3321 was used as the reference instrument as it is well characterized and measurements are not dependent upon particle optical properties. Tests were conducted in a homemade wooden chamber with laboratory generated NaCl and road dust particles. Sensors were found to exhibit high linearity at low particulate concentrations and repeatability, but did not accurately predict actual concentrations. Measurements were also strongly dependent on particle material and size.

Sensor measurements were related with APS using linear regression and non-parametric models. Due to the possibility of parametric model assumptions being violated, comparisons were made between the two models. It was found that statistical differences often existed, which means that linear models are often inadequate for calibrating LLS sensors and should not be used. Higher order polynomials offer the possibility of using parametric models for calibration, which is desirable because it is easier for the general public to understand.

A custom apparatus utilizing the PMS A003 sensor was designed for PM monitoring. The device includes features to allow end users to easily operate the instrument. Since it was known that sensors were strongly dependent on particle source, further testing was completed with several different particle compositions. This was completed to gauge the maximum range of responses and determine the "average" response. Calibration models were developed for PM_{10} and $PM_{2.5}$ number and mass concentration measurements. The 95% prediction interval for PM_{10} and $PM_{2.5}$ number concentration was ±350 and ±360 particles/cm^3, respectively. For PM_{10} and $PM_{2.5}$ mass concentration, the intervals were ±75 and ±45 µg/m^3, respectively.

4.2 Recommendations for Future Work

Evaluation of eight LLS sensors demonstrated that the performance varied considerably between each instrument. This was expected since measurements are affected by sensor design parameters such as laser wavelength, incident angle, optics, flow rate, casing shape, and software algorithm. As a result, development of a model to calibrate all sensors from different manufacturers would likely not yield improved performance. To ensure the confidence of data from low cost sensors, a standardized calibration method should be developed for manufacturers to follow. Such a procedure would involve verifying sensor measurements matches a reference instrument in various real environments over a range of PM concentrations. Experimental setup and methods should be clearly defined to assure consistency. This strategy would ensure all sensors meeting the standard provide similar and accurate measurements in different conditions regardless of how they were designed.

While adoption of a standard by the industry may take several years, a shorter term solution may be to develop a custom monitoring device. The studies completed with the PPC in this work is a step in this direction. Performance of the PPC with laboratory generated aerosols was an improvement compared to just the PMS A003 sensor. Further work is required to verify its performance in real environments over a wider concentration range. A lack of resources only allowed the PPC to be evaluated in the Canada Ontario region, where the outdoor air is clean year-round. For example, the maximum hourly $PM_{2.5}$ concentration at a monitoring station in Downtown Toronto was 36 $\mu g/m^3$ in 2016 (Ontario Ministry of the Environment and Climate Change, 2010b). Nevertheless, the PPC as an effective air quality monitor appears promising. At the low concentrations evaluated in real environments, the response was similar to laboratory generated aerosols. In addition, the dependence on particle source was not strong. The method used to calibrate the PPC in this work will likely apply for real aerosols as well. Once the response in real environments is known, a more relevant calibration model can be developed using the same procedure described in this work for greater accuracy. The method and results of calibrating the PPC can also be provided to consumers, which will secure their confidence in the data obtained.

Further improvement is still required for the PPC with regards to cost, size, and convenience for end use as described in Appendix C. This will likely change the PPC physically in future designs and invalidate the calibration model developed. More specifically, modifications to the casing shape, flow rates (pump and fittings), or flow paths (tubing and its routing) have a significant effect on raw sensor readings. As a result, it is important to completely recalibrate the PPC in all environments every time a change is made to these parameters.

Bibliography

Adachi, M., Kousaka, Y., and Okuyama, K. Unipolar and bipolar diffusion charging of ultrafine aerosol particles. *Journal of Aerosol Science*, 16(2):109–123, 1985.

Amaral, S., de Carvalho, J. A., Costa, M., and Pinheiro, C. An overview of particulate matter measurement instruments. *Atmosphere*, 6:1327–1345, 2015.

Anderson, W. A. *ChE 572: Air Pollution Control*. 2016.

Austin, E., Novosselov, I., Seto, E., and Yost, M. G. Laboratory evaluation of the shinyei ppd42ns low-cost particulate matter sensor. *PLoS ONE*, 10:e0137789, 2015.

Biskos, G. *Theoretical and Experimental Investigation of the Differential Mobility Spectrometer*. Phd dissertation, University of Cambridge, 2004.

Breysse, P. N. and Lees, P. S. J. Air sampling for particulate matter, 2006. URL `http://ocw.jhsph.edu/courses/PrinciplesIndustrialHygiene/PDFs/Lecture9.pdf`.

Chen, D. and Pui, D. A high efficiency, high throughput unipolar aerosol charger for nanoparticles. *Journal of Nanoparticle Research*, 1(1):115–126, 1999.

Cheng, S., Ranade, M., and Gentry, J. Experimental design of high volume electrostatic charger. *Aerosol Science and Technology*, 26(5):433–446, 1997.

Claussen, P. E. C. Regression: When a nonparametric approach is most fitting, 2012.

Cyrys, J., Dietrich, G., Kreyling, W., Tuch, T., and Heinrich, J. $Pm_{2.5}$ measurements in ambient aerosol: comparison between harvard impactor (hi) and the tapered element oscillating microbalance (teom) system. *The Science of the Total Environment*, 278: 191–197, 2001.

Dhaniyala, S. Particle charging, 2003. URL `http://web2.clarkson.edu/class/me538/sol/Particle_Charging.pdf`.

Dhaniyala, S. Aerosol measurement techniques, 2017. URL `http://webspace.clarkson.edu/projects/crcd/me637/downloads/P_Aerosol_Meas_Suresh.pdf`.

Efimov, A. A., Ivanov, V. V., Bagazeev, A. V., Beketov, I. V., Volkov, I. A., and Shcherbinin, S. V. Generation of aerosol nanoparticles by the multi-spark discharge generator. *Technical Physics Letters*, 39:1053–1056, 2013.

Engel-Cox, J., Oanh, N. T. K., van Donkelaar, A., Martin, R. V., and Zell, E. Toward the next generation of air quality monitoring: Particulate matter. *Atmospheric Environment*, 80:584–590, 2013.

Flagan, R. C. *Powder Technology 4.1 Aerosol Particle Generation.* CRC Press/Taylor & Francis, 2007.

Gao, J., Wang, T., Zhou, X., Wu, W., and Wang, W. Measurement of aerosol number size distributions in the yangtze river delta in china: Formation and growth of particles under polluted conditions. *Atmospheric Environment*, 43:829–836, 2008.

Grimm, H. and Eatough, D. J. Aerosol measurement: The use of optical light scattering for the determination of particulate size distribution, and particulate mass, including the semi-volatile fraction. *Journal of the Air & Waste Management Association*, 59: 101–107, 2009.

Groß, J. *Linear Regression.* Springer, 2003.

Grob, B., Burtscher, H., and Niessner, R. Charging of ultra-fine aerosol particles by an ozone-free indirect uv photo-charger. *Aerosol Science and Technology*, 47(12):1325 –1333, 2013.

Han, I., Symanskia, E., and Stock, T. H. Feasibility of using low-cost portable particle monitors for measurement of fine and coarse particulate matter in urban ambient air. *Journal of the Air & Waste Management Association*, 67:330–340, 2017.

Harrison, R. and Yin, J. Particulate matter in the atmosphere: which particle properties are important for its effects on health? *The Science of the Total Environment*, 249: 85–101, 2000.

Holstius, D. M., Pillarisetti, A., Smith, K. R., and Seto, E. Field calibrations of a low-cost aerosol sensor at a regulatory monitoring site in california. *Aerosol Measurement Techniques*, 7:1121–1131, 2014.

Huang, C. H. Field comparison of real-time pm2.5 readings from a beta gauge monitor and a light scattering method. *Aerosol and Air Quality Research*, 7:239–250, 2007.

Intra, P. and Tippayawong, N. An overview of differential mobility analyzers for size classification of nanometer-sized aerosol particles. *Songklanakarin Journal of Science and Technology*, 30(2):243–256, 2008.

Intra, P. and Tippayawong, N. An overview of unipolar charger developments for nanoparticle charging. *Aerosol and Air Quality Research*, 11(2):187–209, 2011.

Jaklevic, J. M., Gatti, R. C., Goulding, F. S., and Loo, B. W. A β-gauge method applied to aerosol samples. *Environmental Science & Technology*, 15:680–686, 1981.

Jiao, W., Hagler, G., Williams, R., Sharpe, R., Brown, R., Garver, D., Judge, R., Caudill, M., Rickard, J., Davis, M., Weinstock, L., Dauphinee, S. Z., and Buckley, K. Community air sensor network (cairsense) project: evaluation of low-cost sensor performance in a suburban environment in the southeastern united states. *Atmospheric Measurement Techniques*, 9:5281–5292, 2016.

Kelly, K., Whitaker, J., Petty, A., Widmer, C., Dybwad, A., Sleeth, D., Martin, R., and Butterfield, A. Ambient and laboratory evaluation of a low-cost particulate matter sensor. *Environmental Pollution*, 221:491–500, 2017.

Kim, J. T. and Chang, J. S. Generation of metal oxide aerosol particles by a pulsed spark discharge technique. *Journal of Electrostatics*, 63:911–916, 2005.

Lee, Y. C., Jeng, F. T., and Chen, C. C. Technique for aerosol generation with controllable micrometer size distribution. *Chemosphere*, 73:760–767, 2008.

Lewis, A. and Edwards, P. Validate personal air-pollution sensors. *Nature*, 535:29–31, 2016.

Liu, C. N., Chen, S. C., and Tsai, C. J. A novel multifilter pm_{10}–$\mathrm{pm}_{2.5}$ sampler (mfpps). *Aerosol Science and Technology*, 45:1480–1487, 2011.

Liu, C. N., Lin, S. F., Awasthi, A., Tsai, C. J., Wu, Y. C., and Chen, C. F. Sampling and conditioning artifacts of $\mathrm{pm}_{2.5}$ in filter-based samplers. *Atmospheric Environment*, 85:48–53, 2014.

Manikonda, A., Zíková, N., Hopke, P., and Ferro, A. Laboratory assessment of low-cost pm monitors. *Journal of Aerosol Science*, 102:29–40, 2016.

Marple, V. A., Liu, B. Y. H., and Rubow, K. L. A dust generator for laboratory use. *American Industrial Hygiene Association*, 39:26–32, 1978.

Matter, D., Mohr, M., Fendel, W., Schmidt-Ott, A., and Burtscher, H. Multiple wavelength aerosol photoemission by excimer lamps. *Journal of Aerosol Science*, 26(7):1101–1115, 1995.

Medved, A., Dorman, F., Kaufman, S., and Pöcher, A. A new corona-based charger for aerosol particles. *Journal of Aerosol Science*, 31:616–617, 2000.

Middha, P. and Wexler, A. S. Particle focusing characteristics of sonic jets. *Aerosol Science and Technology*, 37:907–915, 2003.

Mäkelä, J. M., Aalto, P., Gorbunov, B. Z., and Korhonen, P. Spark distributions from aerosol spark generator. *Journal of Aerosol Science*, 23:233–236, 1992.

Northcross, A. L., Edwards, R. J., Johnson, M. A., Wang, Z. M., Zhu, K., Allene, T., and Smitha, K. R. A low-cost particle counter as a realtime fine-particle mass monitor. *Environmental Science Processes & Impacts*, 15:433–439, 2013.

O'Connor, S., O'Connor, P. F., Feng, H. A., and Ashley, K. Gravimetric analysis of particulate matter using air samplers housing internal filtration capsules. *Gefahrst Reinhalt Luft*, 74:403–410, 2014.

Ontario Ministry of the Environment and Climate Change. Fine particulate matter, 2010a. URL `http://www.airqualityontario.com/science/pollutants/particulates.php`.

Ontario Ministry of the Environment and Climate Change. Search: Air pollutant data, 2010b. URL `http://airqualityontario.com/history/index.php`.

Patashnick, H. and Rupprecht, E. G. Continuous pm-10 measurements using the tapered element oscillating microbalance. *Journal of the Air & Waste Management Association*, 41:1079–1083, 1991.

Saprykina, A. Airborne nanoparticle sizing by aerodynamic particle focusing and corona charging. Master's thesis, University of Calgary, 2009.

Schrobenhauser, R., Strzoda, R., Fleischer, M., Hartmann, A., and Amann, M. C. Detection of the mass of fine particulate matter using light scattering and inertial filtering in a miniaturized sensor setup. *Measurement Science and Technology*, 25: 035103, 2014.

Schwab, J. and Zenkel, M. Filtration of particulates in the human nose. *The Laryngoscope*, 108:120–124, 1998.

Singh, S., Sapra, B. K., Khan, A., Kothalkar, P. K., and Mayya, Y. S. Development of a variable configuration cascade impactor for aerosol size distribution measurement. *Atmospheric Environment*, 44:795–802, 2010.

Solomon, P. A. and Sioutas, C. Continuous and semicontinuous monitoring techniques for particulate matter mass and chemical components: A synthesis of findings from epa's particulate matter supersites program and related studies. *Journal of the Air & Waste Management Association*, 58:164–195, 2008.

Sorensen, C. M. and Fischbach, D. J. Patterns in mie scattering. *Optics Communications*, 173:145–153, 2000.

Tan, Z. *Air Pollution and Greenhouse Gases*. Springer, 2014.

Tan, Z., Givehchi, R., and Saprykina, A. Submicron particle sizing by aerodynamic dynamic focusing and electrical charge measurement. *Particuology*, 2014.

The David Suzuki Foundation. The air we breathe, 2014. URL `http://www.davidsuzuki.org/issues/health/science/air-quality/the-air-we-breathe/`.

The MathWorks Inc. Create linear regression model, 2017. URL `https://www.mathworks.com/help/stats/fitlm.html#inputarg_modelspec`.

The University of Manchester. Optical particle counters, 2016. URL `http://www.cas.manchester.ac.uk/restools/instruments/aerosol/opc/`.

Thomas, J. W. The diffusion battery method for aerosol particle size determination. *Journal of Colloid Science*, 10:246–255, 1955.

Tröstl, J., Tritscher, T., Bischof, O. F., Horn, H.-G., Krinke, T., Baltensperger, U., and Gysel, M. Fast and precise measurement in the sub-20 nm size range using a scanning mobility particle sizer. *Journal of Aerosol Science*, 87:75–87, 2015.

TSI Inc. *Model 3321 Aerodynamic Sizer Spectrometer*, 2004.

TSI Inc. *Model 3076 Constant Output Atomizer*, 2005.

TSI Inc. Condensation particle counter model 3775, 2012a. URL `http://tsi.com/uploadedFiles/_Site_Root/Products/Literature/Spec_Sheets/3775_2980343.pdf`.

TSI Inc. Scanning mobility particle sizer™ (smps™) spectrometer diffusion loss algorithm, 2012b. URL `http://www.tsi.com/uploadedFiles/_Site_Root/Products/Literature/Application_Notes/SMPS-001_Diffusion_Algorithm-A4.pdf`.

TSI Inc. *Fluidized Bed Aerosol Generator Model 3400A*, 2014.

TSI Inc. Choosing the right cpc for your application, 2015. URL `http://www.tsi.com/uploadedFiles/_Site_Root/Products/Literature/Application_Notes/CPC-002-appnote.pdf`.

Tuch, T., Mirme, A., Tamm, E., Heinrich, J., Heyder, J., Brand, P., Roth, C., Wichmann, H. E., Pekkanen, J., and Kreyling, W. G. Comparison of two particle-size spectrometers for ambient aerosol measurements. *Atmospheric Environment*, 34:139–149, 2000.

Turner, J. H., Lawless, P. A., Yamamoto, T., Coy, D. W., Greiner, G. P., McKenna, J. D., and Vatavuk, W. M. Sizing and costing of electrostatic precipitators. *Air & Waste Management Association*, 38:458–471, 1988.

Volckens, J. and Peters, T. M. Counting and particle transmission efficiency of the aerodynamic particle sizer. *Journal of Aerosol Science*, 36:1400–1408, 2005.

Vosburgh, D. J. H., Klein, T., Sheehan, M., Anthony, T. R., and Peters, T. M. Design and evaluation of a personal diffusion battery. *Aerosol Science and Technology*, 47: 435–443, 2013.

Wang, Y., Li, J., Jing, H., Zhang, Q., Jiang, J., and Biswas, P. Laboratory evaluation and calibration of three low-cost particle sensors for particulate matter measurement. *Aerosol Science and Technology*, 49:1063–1077, 2015.

Watson, J. G., Chow, J. C., Chen, L. W. A., Kohl, S. D., Casuccio, G. S., Lersch, T. L., and Langston, R. Elemental and morphological analyses of filter tape deposits from a beta attenuation monitor. *Atmospheric Research*, 106:181–189, 2012.

Webb, P. A. *A Primer on Particle Sizing by Static Laser Light Scattering*. Micromeritics, 2000.

Weijersa, E., Khlystovb, A. Y., Kosa, G. P. A., and Erismana, J. W. Variability of particulate matter concentrations along roads and motorways determined by a moving measurement unit. *Atmospheric Environment*, 38:2993–3002, 2004.

Winkel, A., Rubio, J. L., Veld, J. W. H., Vonk, J., and Ogink, N. W. Equivalence testing of filter-based, beta-attenuation, teom, and light-scattering devices for measurement of pm_{10} concentration in animal houses. *Journal of Aerosol Science*, 80:11–26, 2015.

World Health Organization. Who air quality guidelines for particulate matter, ozone, nitrogen dioxide and sulfur dioxide. Technical report, 2005.

World Health Organization. Air pollution levels rising in many of the world's poorest cities, 2016a. URL `http://www.who.int/mediacentre/news/releases/2016/air-pollution-rising/en/`.

World Health Organization. What is ionizing radiation?, 2016b. URL `http://www.who.int/ionizing_radiation/about/what_is_ir/en/`.

Appendix A

Overview of Aerosol Measurement Techniques

Table A.1 lists the aerosol measurement techniques reviewed, and summarizes the main advantages and limitations of each. Evidently a wide range of techniques are available and present various advantages in terms of cost, accuracy, particle size measurement range, and limitations.

Filter Based Manual Sampling

FBMS involves pumping an aerosol stream through filters housed within air samplers and collecting the airborne particles. After a period of time, the filter is removed and laboratory analysis is performed. In gravimetric analysis, the mass of PM collected is measured by weighing the filter before and after sampling. The weight difference yields the total collected PM (O'Connor et al., 2014). The PM concentration can be calculated by dividing collected PM mass by air volume, which is known from the product of calibrated air flow rate and sampling time (Breysse and Lees, 2006). Accurate measurements require minimization of electrostatic effects, control of moisture and volatiles sorption, temperature stability, and care in sample handling (O'Connor et al., 2014). Particle losses due to evaporation (Liu et al., 2014) and wall deposition are also of concern. Additional analysis can be performed with the samples to determine chemical compositions of the collected PM.

Liu et al. (2011) developed a multifilter PM_{10}-$PM_{2.5}$ sampler (MFPPS) where four PM_{10} and four $PM_{2.5}$ samples are simultaneously collected. The motivation for collecting multiple samples was due to the need of various laboratory analysis. The design consists

Table A.1: Summary of instruments for measuring PSD.

Instrument	Advantages	Limitations
LLS	• Real time measurements. • Portable and inexpensive. • Can measure several size bins simultaneously.	• Affected by drift. • Needs to be calibrated for different aerosols.
FBMS	• Collected particles can be analyzed chemically. • Accurate and precise. • Directly measures PM mass.	• Low time resolution. • Filter requires careful handling and conditioning. • Measurements not real time.
BAM	• Real time measurements. • Reduced sample handling. • Accuracy equivalent to gravimetric methods.	• Requires radioactive materials. • Affected by humidity if inlet is unheated, but loss of semi-volatiles if heated.
TEOM	• Real time measurements. • Directly measures PM mass. • Sensitive to all particles.	• High capital cost. • Affected by humidity if inlet is unheated, but loss of semi-volatiles if heated.
CI	• Configurable for applications. • Portable. • Can measure size bins simultaneously.	• Limited number of size channels. • Requires low vacuum pump.
DB	• Real time measurements. • Potential for portability.	• Requires a separate counter. • Upper size limit of ∼300 nm.
APS	• High counting efficiency for solid particles. • Can measure multiple size bins simultaneously. • Usable for different conditions.	• High capital cost. • Requires knowledge of particle density. • Measures mass indirectly; potential for conversion error.
SMPS	• Accurately measures nanoparticle PSD. • Widely used instrument.	• May use radioactive materials. • Affected by particle shape. • High response time.

of: (i) an annular inlet with PM_{10} impactor; (ii) Y-type fitting leading to four PM_{10} filter holders and $PM_{2.5}$ impactor; (iii) four filter holders behind the $PM_{2.5}$ impactor; (iv) orifices behind the filter holders to maintain flow rate uniformity through all flow paths; (v) ambient temperature and pressure sensors; and (vi) two mass flow controllers. Effort was made to reduce particle wall loss by ensuring smooth flows in the device. The MFPPS was tested along side the dichotomous PM_{10} sampler (Andersen Model SA-241) and EPA WINS $PM_{2.5}$ sampler (Thermo Model 2000-FRM). The measurements made by MFPPS was found to agree well with the other two samplers.

Beta Attenuation Monitor

In beta attenuation monitors, β-particle spectrums from a radioisotope source pass a thin film where PM is collected. By measuring the number of electrons transmitted, PM mass on the film can be determined. The flux through a thin uniform foil is expressed as:

$$I = I_0 e^{-\mu x} \tag{A.1}$$

where I_0 is the incident flux, μ is the mass absorption coefficient (cm^2/g), and x is the thickness of the film (g/cm^2). As seen from the equation, increasing PM deposition or x directly leads to less electrons transversing the film. The values of I_0 and μ are normally determined by measuring I as a function of x for several known standards. This method is advantageous over direct weighings for PM measurements since handling of fragile filter samples is minimized, the risk of contamination is reduced, and the automated analysis of many samples can be facilitated (Jaklevic et al., 1981). In addition the electron transmission has a weak dependence on particle composition (Watson et al., 2012).

BAMs consist of a radioisotope source, sample, and detector as shown in Figure A.1. Jaklevic et al. (1981) developed a BAM with similar configuration as shown in the Figure. The source used was ^{147}Pm in a 2.54 cm diameter cylindrical holder and detector was an Ortec Model CA-018-300-300 silicon surface barrier detector. The distance between source and detector was 0.7 cm. Their method was shown to be equivalent in accuracy compared to gravimetric methods with proper instrumental design and calibration.

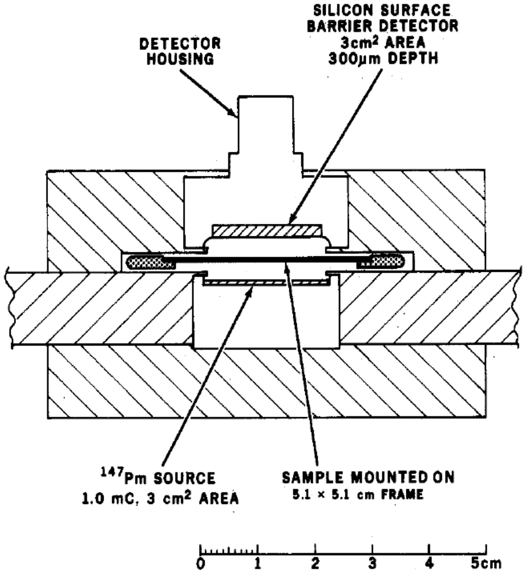

Figure A.1: Schematic diagram of a BAM (Jaklevic et al., 1981).

Tapered Element Oscillating Microbalance

The TEOM technique uses a hollowed tapered tube with one end wider and fixed as shown in Figure A.2. A filter is placed on the other end and air is passed through. This end is maintained in oscillation by feedback electronics. As particles deposit on the filter, the frequency of oscillation changes and this is detected by a precision frequency counter. PM mass can be determined directly and when combined with flow rate information, the device provides accurate measurements of particle concentration in real time (Patashnick and Rupprecht, 1991). Readings from TEOM is very sensitive to ambient humidity due to water vapor collecting on the filter and altering the oscillation frequency. To eliminate this effect, the sampler inlet and filter is heated to around 50 °C. However this can cause a loss of particles collected on the filter if it is volatile (Cyrys et al., 2001).

Cascade Impactor

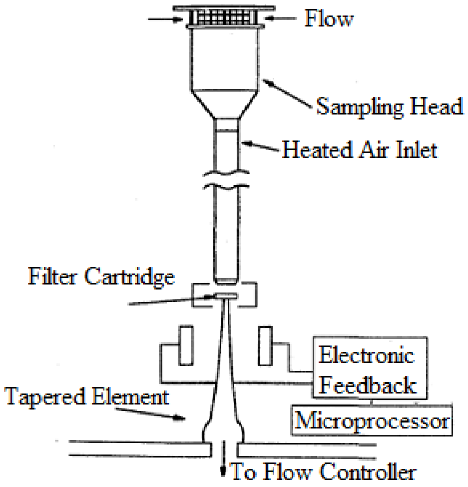

Figure A.2: Schematic diagram of a TEOM (Patashnick and Rupprecht, 1991).

Conventional cascade impactors consist of a nozzle for acceleration of aerosols and a flat, rigid impaction surface (substrate). When the air passes through the nozzle and is directed towards the substrate, it changes direction abruptly to flow around the obstacle. Particles above a certain aerodynamic diameter (cut-off size of the impactor) have enough inertia that it will not follow the streamlines and will collide with the substrate. Smaller particles continue flowing towards subsequent impactors with lower and lower cut-off sizes until it is eventually captured (Singh et al., 2010).

The main parameter which predicts whether or not a particle impacts the substrate is the dimensionless Stokes number defined by Equation 2.5. In this application, u_0 is the average velocity at a nozzle exit, and the characteristic dimension d_c is the nozzle diameter. The parameters which can be practically varied to collect different sized particles are nozzle diameter and Cunningham slip correction. CIs which operate at atmospheric pressure are able to separate particles down to 0.4 μm and low pressure impactors cover particles from 30 nm to 30 μm (Singh et al., 2010).

Singh et al. (2010) developed a Variable Configuration Cascade Impactor (VCCI) which can be assembled and adapted for different applications, as shown in Figure

A.3. There is a maximum of 11 impactor stages, with a critical orifice placed after the seventh stage to control flow through the device and maintain low pressure. The device operates at atmospheric and low pressure, and can be used as a PM_x impactor. The three configurations at which the device can be operated is summarized in Table A.2. A significant limitation of the VCCI is that measurements were not real time. Substrates with captured particles must be further analyzed in the laboratory to obtain mass concentrations. In addition the size resolution is not high because the maximum number of bins is limited to the number of impactors.

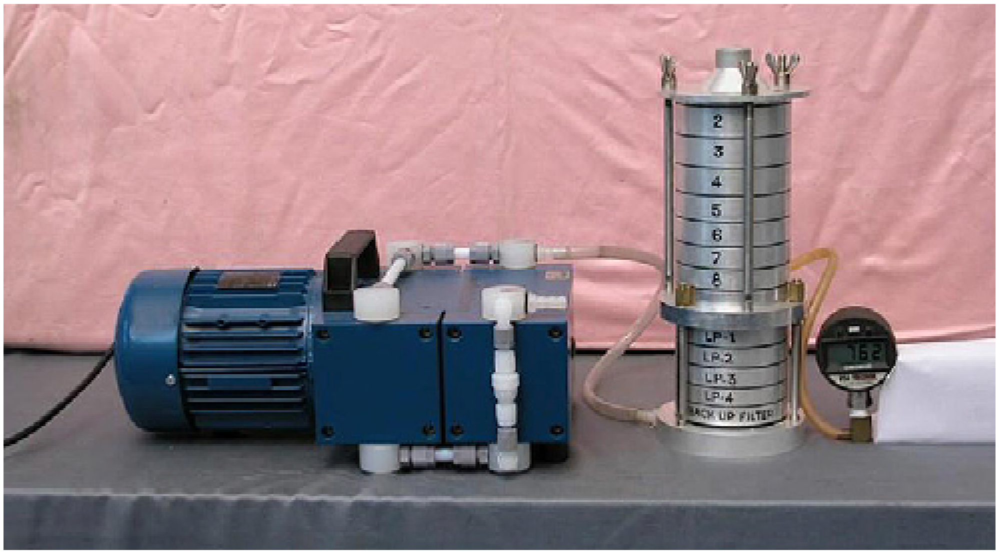

Figure A.3: Photograph of the VCCI developed by Singh et al. (2010).

Table A.2: Configurations of the VCCI developed by Singh et al. (2010).

Configuration	Set-up	Particle Size Range
Low-Pressure	All eleven stages and critical orifice present.	0.1 - 21.3 μm
Atm. Pressure	Top seven and back up stage present.	0.53 - 10 μm
PM_x	Selected stages from top seven removed.	Various PM_x

Diffusion Battery

The DB takes advantage of the random Brownian motion of submicron particles to measure their size. The general working principle involves passing aerosol through a channel. As the particle travels, Brownian movement causes it to displace from the fluid streamline; the average displacement is proportional to the square root of travel time. The magnitude of Brownian motion also increases with decreasing particle size. A fraction of particles are displaced sufficiently to reach the channel walls. It is assumed that those particles will adhere. The smaller the particle, the fewer will exit the channel. Therefore by counting the number of exiting particles the size can be determined (Thomas, 1955).

Vosburgh et al. (2013) developed a personal DB which could be placed in a backpack and used for personal sampling of aerosols from 17 to 286 nm. The DB consisted of a sampling tube, solenoid valve controller, screen type DB, solenoid valves, electrical battery, and detector as shown in Figure A.4 (left). Four stages were implemented, and solenoid valves automatically switched between stages as shown in Figure A.4 (right). This changes the airflow path through different number of screens where particles collect (due to diffusion) and are not counted by the detector. The penetration of particles through each of the stages depended on their size. A condensation particle counter acted as the detector to count particles exiting the stages and estimate the particle number concentrations. The DB was compared against a scanning mobility particle sizer (SMPS), and results were within 25% for 5 of 12 polydisperse combustion aerosols tested.

Aerodynamic Particle Sizer

APS measures particle sizes from 0.5 to 20 μm and with multiple size channels. Aerosol is accelerated through an orifice and a particle's aerodynamic size determines its rate of acceleration; small particles accelerate more rapidly than larger ones due to lower inertia. Particles pass two laser beams and produce two pulses of scattered light. The time delay between the pulses determines the particle's velocity, which can be related to aerodynamic diameter (TSI Inc., 2004). Aerosol entering the APS is separated into two flow paths as shown in Figure A.5. One is passed through a high efficiency filter and recombines with the unfiltered aerosol to act as the sheath flow. Air is accelerated through a nozzle and

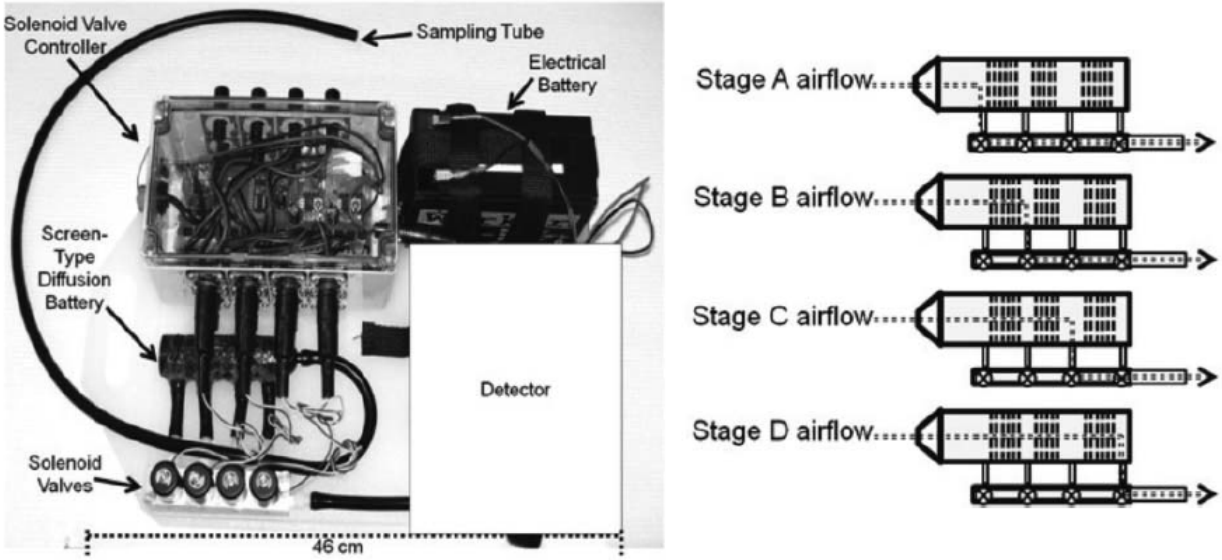

Figure A.4: Photograph of the personal DB (left) and stage schematic (right) developed by Vosburgh et al. (2013).

enters the sensing zone. Inside the optical chamber, moving particles cause the two pulses of light due to two incident laser diode beams (Volckens and Peters, 2005).

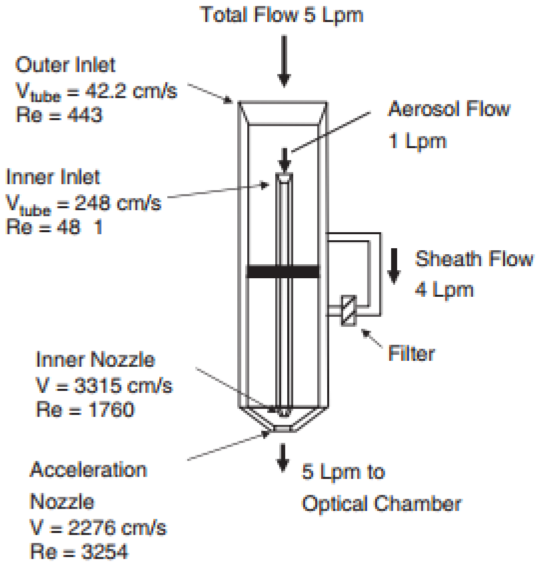

Figure A.5: Schematic of the aerosol flow in APS (Volckens and Peters, 2005).

Volckens and Peters (2005) investigated the counting efficiency of the commercially available APS 3321 (TSI Inc., MN U.S.). The researchers found counting efficiencies to range from 85 to 99% for solid particles. For liquid droplets, the efficiencies declined from 75% at 0.8 μm drops to 25% for 10 μm drops. Losses of larger particles were found to occur due to impact with the inner nozzle and additional unknown mechanisms downstream. The higher efficiencies for solid particles was because of their tendency to bounce off interior surfaces, instead of adhering like liquid droplets. Lastly, APS derives mass concentrations from the particles counted- it was found that small sizing errors produce substantial errors when converted to mass concentrations.

Scanning Mobility Particle Sizer

SMPS consist of a differential mobility analyzer (DMA) for classification and a condensation particle counter (CPC) or Faraday cup for counting.

Inlet aerosol samples can have any charge distribution, so to successfully classify particles by DMA, their charge distribution must be known. The problem is typically solved by neutralizing the aerosol sample through bipolar diffusion using radioactive material or soft x-ray. The charge on particles as a function of size is known from the Fuchs' limiting sphere charge distribution model Biskos (2004).

After neutralization, particles enter the DMA, which work based on the physical principle that the trajectory of charged particles in an electric field depends on their size. The general operating schematic of a DMA is shown in Figure A.6. The design involves two concentric metal electrodes, with the inner electrode maintained at a set negative voltage ranging from 1 to 10 kV. The outer electrode grounded, and this creates the electric field which particles transverse. At the top of the DMA, charged polydisperse aerosol and particle free sheath air flow down the annular space between the electrodes. The aerosol is introduced from the outer electrode, and surrounds the sheath air. Both streams are assumed to be laminar, and no mixing occurs. Positively charged particles are attracted to the negative electrode, and they move through the sheath air. Most particles collect on the inner electrode, and the location of deposition depends on their size. However, those within a very narrow size range will enter a slit at the bottom of the electrode, and exit the DMA as a monodisperse aerosol (Intra and Tippayawong, 2008).

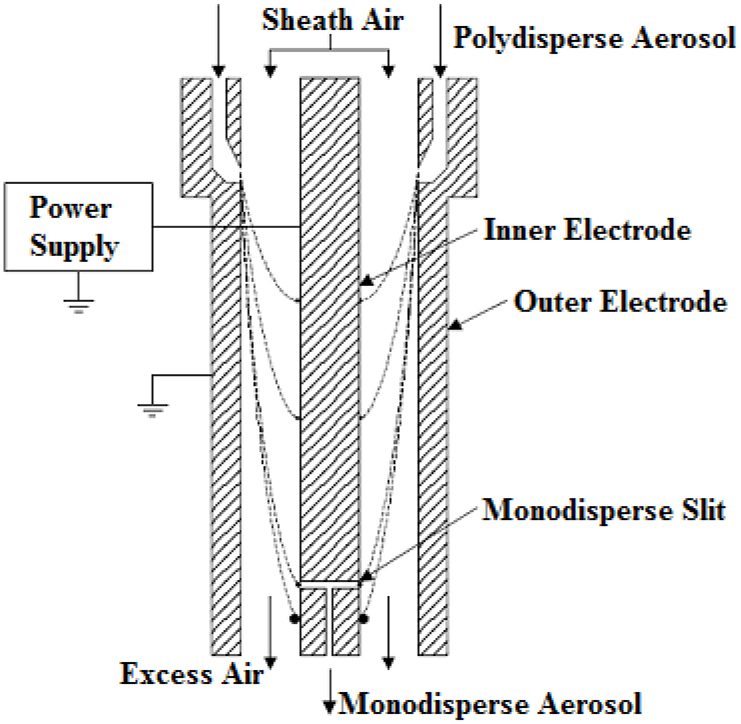

Figure A.6: Operating schematic of a DMA (Intra and Tippayawong, 2008).

The size of particles entering the slit can be predicted if their electrical mobility is known. In the DMA, charged particles experience an opposing viscous drag and electrical force. By using Stoke's law to calculate the drag force, the electrical mobility can be calculated as:

$$Z_p = \frac{v}{E} = \frac{n_p e C_c}{3\pi\mu d_p} \tag{A.2}$$

where Z_p is the electrical mobility, v is the gas velocity, E is the electrical field strength, n_p is the number of charges per particle, e is the elementary electrical charge (1.602×10^{-19} C), C_c is the Cunningham slip correction factor, μ is the gas viscosity, and d_p is the particle diameter (Intra and Tippayawong, 2008). Electrical mobility can also be found from the DMA geometry and operating conditions, and is given by:

$$Z_p = \frac{Q_s + Q_a}{2\pi LV} ln\left(\frac{R_2}{R_1}\right) \tag{A.3}$$

where Q_s is the sheath air flow rate, Q_a is the aerosol flow rate, R_2 and R_1 are the inner and outer electrode radii respectively, L is the effective electrode length, and V is the applied voltage (Intra and Tippayawong, 2008). Combining equations A.2 and A.3, the expression for particle diameter can be found as:

$$d_p = \frac{2n_p eVLC_c}{3\mu(Q_s + Q_a)ln(R_2/R_1)} \tag{A.4}$$

By coupling Equation A.4 with calibration experiments, the particle diameter of the monodisperse aerosol exiting the DMA can be found. For example, TSI SMPS Spectrometers use a diffusion loss algorithm to account for particles adhering to surfaces (TSI Inc., 2012b). The electrode voltage can be adjusted to change the size of particles exiting the DMA, so counting over the entire size range is possible.

CPCs count particles by condensing a liquid, typically an alcohol or water, onto the particles to enlarge them. Nanoparticles are typically too small to scatter light and enable detection, so by increasing its size, counting is possible using optical methods. The aerosol sample first enters a heated saturater where a condensing liquid is vaporized into the stream. The mixture then enters a cooled condenser and here the particles act as condensation nuclei for the vapor. As liquid condenses on the particles, they grow in size allowing detection optically (TSI Inc., 2012a). In this step, every particle passes though a laser beam and causes a flash of light. Each pulse is counted as a particle by the CPC (TSI Inc, 2015).

An alternative to CPC is to measure the current produced by charged particles. In such scenarios, particles are charged with unipolar ions instead of bipolar ions before entering the DMA to improve detection limits. Particles are captured by a Faraday cage and the current is measured by an electrometer. Number concentration of an aerosol sample can be determined through the following relation:

$$N = \frac{I}{qQ} \tag{A.5}$$

where I is the current measured by the electrometer (A), q is the average charge on each particle in the sample (C), and Q is the aerosol flow rate (m^3/s) (Biskos, 2004). Note that if particles were charged by diffusion, q can be found from Equation D.3.

Appendix B
Various Software Code

B.1 Non-Parametric Regression and Bootstrap

```
# Original code provided by Yixuan Li
rm(list = ls())
# Insert Libraries
library(MASS)
library(e1071)
library(nleqslv)
library(R.matlab)
# Input data
# Matlab data is organized into a 48 row cell structure
# Each row corresponds to an experimental X, Y dataset
# Columns 1 and 2 contains X and Y data, respectively
Data <- readMat('C:/Users/Bentan/Google Drive/Masters/Particle Sensor
   Evaluation/Sensor_Data_Organized.mat')
attach(Data)
# Define the variables
B = 1000
dt = 1
# Array for storing whether the null hypothesis was accepted for each dataset
Results <- matrix(NA, 48, ncol = 1)
# Datasets 1-40 and 45-48 can be solved entirely by this program
# Datasets 41-44 requires external program to solve for A1, A2, and p
for (r in 1:40){
       # After import from Matlab to R the columns of the cell array get
          stacked
       X <- as.numeric(unlist(Data$Data[[r]]))
       Y <- as.numeric(unlist(Data$Data[[r+48]]))
       df<-data.frame(X=X,Y=Y)
       # Change to X<100 and rerun code to analyze the data at low
          concentrations
       df<-subset(df,X>=100)
       X <- df$X
       Y <- df$Y
       # Bandwidth Calculation
```

```
bw <- bw.ucv(X)
# A. Calculation of T stat
# A.1 Y Estimate using kernel method
Mhat.data <- matrix(NA, nrow = length(X), ncol = 1)
for(i in 1:length(X)){
       K = dnorm((X-X[i])/bw)
       Mhat.data[i] = sum(K*Y)/sum(K)
}
# A.2 Calibration of a OLS model
model <- lm(Y~X)
Y.hat <- model$coefficient[1]+model$coefficient[2]*X
# A.3 Y Estimate for parametric model using nonpara method.
Mhat.np.data <- matrix(NA, nrow = length(X), ncol = 1)
for(i in 1:length(X)){
       K = dnorm((X-X[i])/bw)
       Mhat.np.data[i] = sum(K*Y.hat)/sum(K)
}
# A.4. T Result
T<- max(abs(Mhat.data- Mhat.np.data))
# Calculate the mean,variance and the third moment of the error
NMfun<-function(x, variance, skew){
       y <- rep(NA, length(x))
       y[1] <- x[1]*x[3]+x[2]*(1-x[3])
       y[2] <- x[1]^2*x[3]+x[2]^2*(1-x[3])-variance
       y[3] <- x[1]^3*x[3]+x[2]^3*(1-x[3])-skew
       return(y)
}
error <- Y - Mhat.data
mean(error)
variance <- moment(error,order=2,center=TRUE)
skew <- moment(error,order=3,center=TRUE)
xstart <- c(-50, 50, 0.5) # Initial guess for values of A1, A2, and p
NMfun(xstart, variance, skew)
# Solve the system of equations:
# A1p+A2(1-p)=0; (A1^2)p+(A2^2)(1-p)=variance; (A1^3)p+(A2^3)(1-p)=skew
solver <- nleqslv(xstart, NMfun, method="Newton", variance=variance,
   skew=skew, control=list(maxit=1000000,stepmax=0.01,allowSingular=
   TRUE))
# For datasets 41-44 these values were solved for and set manually
A1=solver$x[1]
A2=solver$x[2]
p=solver$x[3]
error.new <- c(A1,A2) # Based on the estimation error
Tstar <- c()
# Start the 1000 sample bootstrap
for (i in 1:B){
```

```
            Y.bootstrap <- c()
            # Generate bootstrap error based on 2 point distribution
            bootstrap.error <- sample(error.new,length(X),replace=TRUE,prob=
                c(p,1-p))
            Y.bootstrap <- Mhat.np.data + bootstrap.error
            # B.1 Nonparametric estimate using bootstrap sample
            kernel.bootstrap =c()
            for(j in 1:length(X)){
                    K = dnorm((X-X[j])/bw)
                    kernel.bootstrap[j] = sum(K*Y.bootstrap)/sum(K)
            }
            # B.2 Parametric estimate using bootstrap sample
            # Step 1: Calibrate model with Career.High.bootstrap
            Y.ft <- lm(Y.bootstrap~X)
            Yhat.bootstrap <- Y.ft$coefficient[1]+Y.ft$coefficient[2]*X
            # Step 2: Use non-parametric method
            Y.nonpara.bootstrap <- c()
            for(h in 1:length(X)){
                    K = dnorm((X-X[h])/bw)
                    Y.nonpara.bootstrap[h] = sum(K*Yhat.bootstrap)/sum(K)
            }
            # B.3 Tstar
            Tstar[i] <-max(abs(kernel.bootstrap-Y.nonpara.bootstrap))
        }
        # Find 95% quantile and test hypothesis
        Q3 <- quantile(Tstar,prob = 0.95)
        {if(T<Q3) {
                Results[r]=1 # Null hypothesis accepted
                }
        else {
                Results[r]=0 # Null hypothesis rejected
                }
        }
        # Confirm a solution was found for A1, A2, and p
        print(solver$message)
}
print(Results)
```

B.2 Fluent Cunningham Drag Force UDF

```
/*Original code modified from the following source:*/
/*the following implements a diameter-dependent Cunningham slip correction
   factor*/
/*Actual drag coeffs used by Fluent have been referenced-chased (Morsi, SA.
   Alexander, AJ. (1972). An investigation of particle trajectories in two-
```

```
   phase flow systems)*/
/*CFDYouself.blogspot.co.uk, JRH, 09.10.15 */
#include "udf.h"
#include "math.h"
DEFINE_DPM_DRAG(cunningham_drag_force, Re, p){
       cell_t c = P_CELL(p);
       Thread *t = P_CELL_THREAD(p);

       real lambda, Kn, Cc;
       lambda = 0.175*133.322*pow(10,-6)*C_T(c, t)/C_P(c, t);
       Kn=2*lambda/P_DIAM(p);
       Cc = 1+1.657*Kn;

       real Cd, drag_force;
       if (Re < 1){
              Cd = 24 / Re;
              drag_force = 18*Cd*Re/(24*Cc);
              return (drag_force);
       }
       else if (Re < 1000){
              Cd = Re*(1+0.15*pow(Re,0.687))/24;
              drag_force = 18 * Cd*Re / (24*Cc);
              return (drag_force);
       }
       else{
              Cd = 0.44;
              drag_force = 18 * Cd*Re / (24*Cc);
              return (drag_force);
       }
}
```

Appendix C
Design of a Portable Particle Counter

C.1 Summary

A custom apparatus for PM monitoring was developed using the PMS A003, an off the shelf LLS based sensor. Design requirements for the prototype include cost, weight, size, ease of use, portability, and ability to accurately measure PM concentration. Since the PMS A003 is not a module, it must be integrated with other components such as a microcontroller, power supply, and display screen. All parts will be contained in a case, which together makes up the apparatus.

While many problems still existed with the first iteration, the most essential functions were verified. The prototype was capable of obtaining measurement data from the PMS A003 and displaying the information on a screen. Data could also be logged in a on-board memory card or uploaded online through Wi-Fi. The main issues resided with the power supply, in which it was inconvenient to turn off the device.

A second design was conceived to move forward with sensor calibration without delay. Although there was not a display screen, the feature was not required for testing purposes. Issues with the power supply were resolved by using a different battery power management board. At the current state, PM monitoring aspects have been verified, and calibrated measurements show good agreement with the reference instrument. The remaining obstacles are related to designing the hardware in a way it is easy to manufacture and further developing software to provide a seamless user experience.

C.2 Design Requirements and Concept

The need for an apparatus to measure particulate concentration arose from the lack of accurate instruments on the market. Since the strategy for resolving this problem was to calibrate a bare off the shelf sensor, developing a platform was required to provide the user with a convenient means of operating the instrument. Examples of user friendly PM monitoring apparatuses are the Fluke 985, Handheld 3016, DC1100 Pro, and Node. Thus these devices were appropriate benchmarks for developing the PPC. The design requirements of the PPC are as follows:

1. Count the number of airborne particles.
    (a) Detect particles up to 10 µm.
    (b) Resolution of at least PM_{10} and $PM_{2.5}$.
    (c) Measurements are ±10% of those measured by a standard instrument.
    (d) Sample every 5 seconds or less.
    (e) Real time and continuous.
    (f) Timestamps are included with measurements.
2. Hardware costs less than $500 CAD.
3. Weigh less than 700 g.
4. Dimensions less than 25 × 12 × 5 cm.
5. Can be battery powered for at least 6 hours.
6. Stores at least 1 year of continuously measured data.
7. Allows retrieval of logged data to personal computer.
8. Look aesthetically pleasing.

The conceptual design of the PPC is shown in Figure C.1 with main hardware components and their connections. At the heart of the device is the microcontroller, which is highlighted in green. Red lines show the direction of current flow, and blue lines show signal connections between components. All hardware used for the design will be enclosed in a plastic casing.

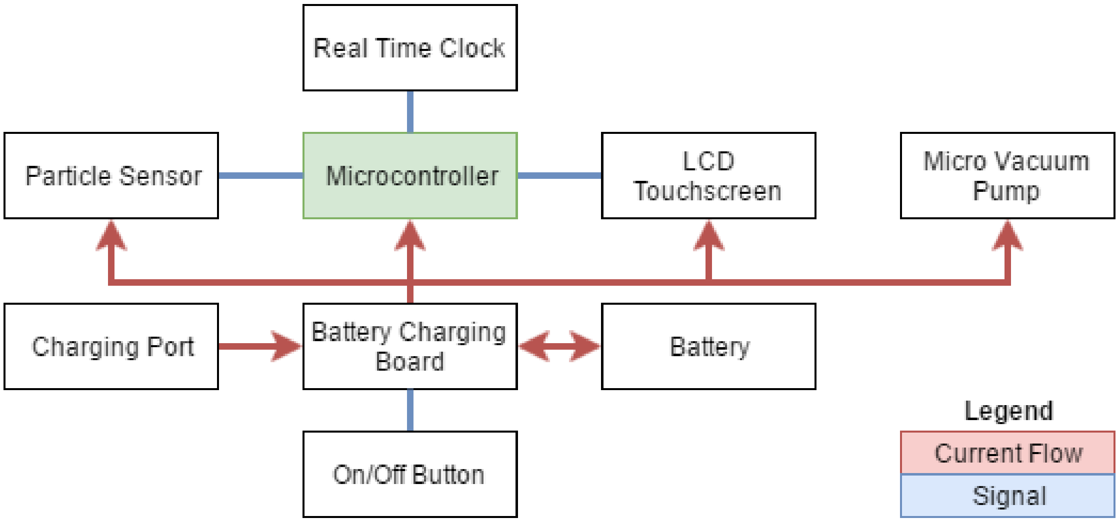

Figure C.1: Diagram of the design concept.

The microcontroller controls most of the components of the PPC. It is required to obtain and process data from the particle sensor, log data to memory storage, allow retrieval of stored data, keep track of the time, communicate with the LCD touchscreen to allow user interaction. Several options exist for obtaining logged data, including Wi-Fi, Bluetooth, and USB connectivity.

A particle sensor based on laser light scattering will be used in the design, as this is essentially the only low cost technique. The sensor will draw in ambient air, count the particles, and relay this information to the microcontroller. The selected sensor should be off the shelf and readily available.

The touchscreen allows the user to interact with the PPC by displaying information, allowing data retrieval and changing settings. An alternative to the LCD screen would be a separate portable device with a screen, such as the user's smartphone. By implementing Bluetooth connectivity communication could be established between the PPC and smartphone eliminating the need for a LCD screen.

A real time clock (RTC) is included because during power off, the microcontroller does not keep track of the time. Timekeeping is thus needed to meet Design Requirement 1f. The RTC assembly will have a coin cell battery which will allow operation even when powered off or the main battery is depleted. Certain microcontrollers have built in RTCs so in those cases only a coin cell battery would be required.

Implementing a micro-pump improves accuracy by increasing air sampling. Sensors typically come with built in fans, but the vacuum and flow rate may too low. Greater flow rates are more accurate because larger particles which would otherwise not be drawn into the device will be counted more efficiently. In addition a larger space around the device will be sampled, reducing outliers. Overall, the pump should lower the sensor's sensitivity to particle source.

To allow portability a battery is required to power the device. A charging port provides a connection for external power sources to recharge the battery. A charging board is also required to protect the battery by preventing excessive current draw, overcharging, and overheating. Lastly, an on/off switch is included to turn on and shut off the device.

C.3 Design Iterations

C.3.1 First Iteration

A photograph of the prototype's first design iteration is shown in Figure C.2 (left) with assembled internal components (right). A complete list of components used is shown in Table C.1, and components used in the custom PCB is shown in Table C.2. The total cost for one prototype is $410, excluding taxes and shipping. Note that certain parts require multiple quantities to be ordered, so the price reflects a bulk purchase.

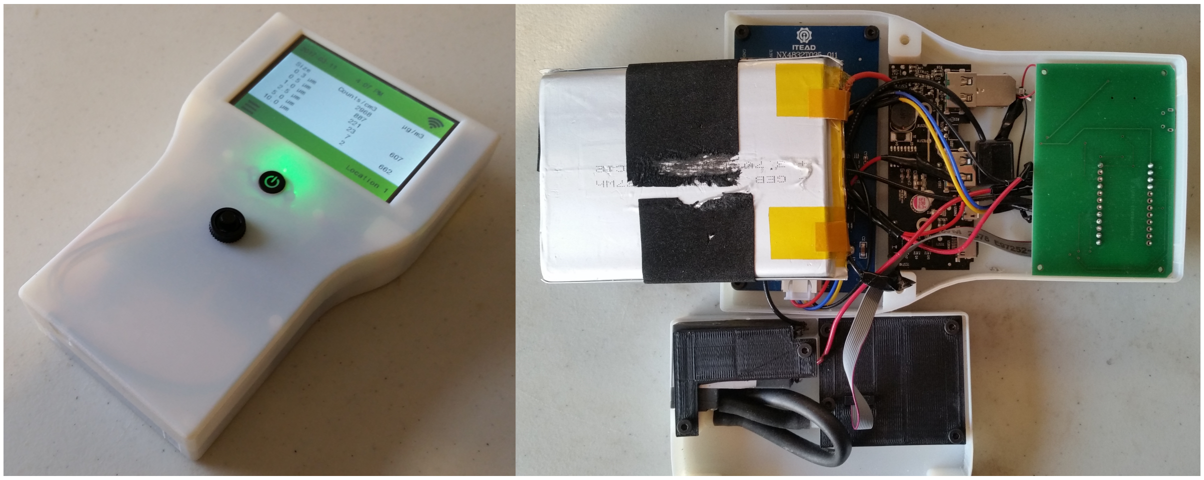

Figure C.2: Photograph of the first design iteration (left) and internal components (right).

Casing

A screenshot of the case CAD model is shown in Figure C.3, with important features labeled. After modeling, files were provided to an external contractor for 3D printing. PolyJet printing technique was used, which allows parts with small detail and excellent surface finishes to be printed. Two additional parts for securing the pump and PMS A003 to the casing were also 3D printed as shown in Figure C.4. Since these parts did not require smooth surfaces, they were printed by a FlashForge fused deposition modeling (FDM) printer in the laboratory. In summary, the casing was designed to have the following:

1. Ability to hold all components listed in Table C.1 compactly.
    (a) Mounts for the PCB, charging board, and LCD touchscreen.
    (b) Securing the battery, mini vacuum pump, and sensor.
    (c) Openings for the on and off buttons, aerosol inlet and outlet, charging port, and LCD touchscreen.
2. Ability to join the two halves together, and have grooves at the mate.

Table C.1: List of components used in the first design iteration.

Component	Manufacturer	Part Number	Qty.	Cost
Casing	Concept Parametric	Custom	1	$210
Mini Vacuum Pump	Shenzhen Faith Co.	Z1312-5006-8500	1	$15
Particle Sensor	Plantower	PMS A003	1	$34
Battery Module	Aukey	PB-N36	1	$26
LCD Touchscreen	ITEAD Ltd.	NX4832T035	1	$37
Microcontroller	Particle	Photon	1	$29
Off Button	Judco Inc.	40-3536-00	1	$2
PCB	Seeed Ltd.	Custom	1	$31
Coin Cell Battery	Sony	CR2032	1	$0.70
Micro SD Card	Kingston	SDC4/8GB	1	$9
Misc. Hardware				
1-72×1/4” Screw	McMaster-Carr	91251A066	6	$0.70
M3×0.5, 6 mm Screw	McMaster-Carr	93070A061	6	$1.40
M4×0.7, 25 mm Screw	McMaster-Carr	91290A176	2	$0.40
Barbed Fitting	McMaster-Carr	5463K53	2	$1.10
1/8” ID Tubing	McMaster-Carr	5034K21	15 cm	$0.30
22 AWG Wire	All Electronics	HW-50	1	$0.50
10 Wire Connector	Harwin Inc.	M50-9100542	1	$11.30
Total				$410

Table C.2: List of components used in the custom PCB.

Component	Manufacturer	Part Number	Qty.
10k Resistor	AVX Co.	009276006021106	3
Female Header	Yageo	RC0805FR-0710KL	2
USB Connector	Hirose Electric Ltd.	ZX62D-B-5P8	1
Male Header	Harwin Inc.	M50-3600542	1
Li-Cell Holder	MPD	BK-912	1
SD Card Holder	Shenzhen Elec. Ltd.	TF-01	1
Piston Connector	Mill-Max Corp.	811-22-002-30-000101	1

3. Snap fits to prevent the case from opening due to material deformation.
4. Walls were as thin as possible while still providing enough rigidity.
5. Airtight aerosol flow from inlet to outlet.
6. Could be 3D printed.
7. Look simple and have rounded edges for aesthetics.

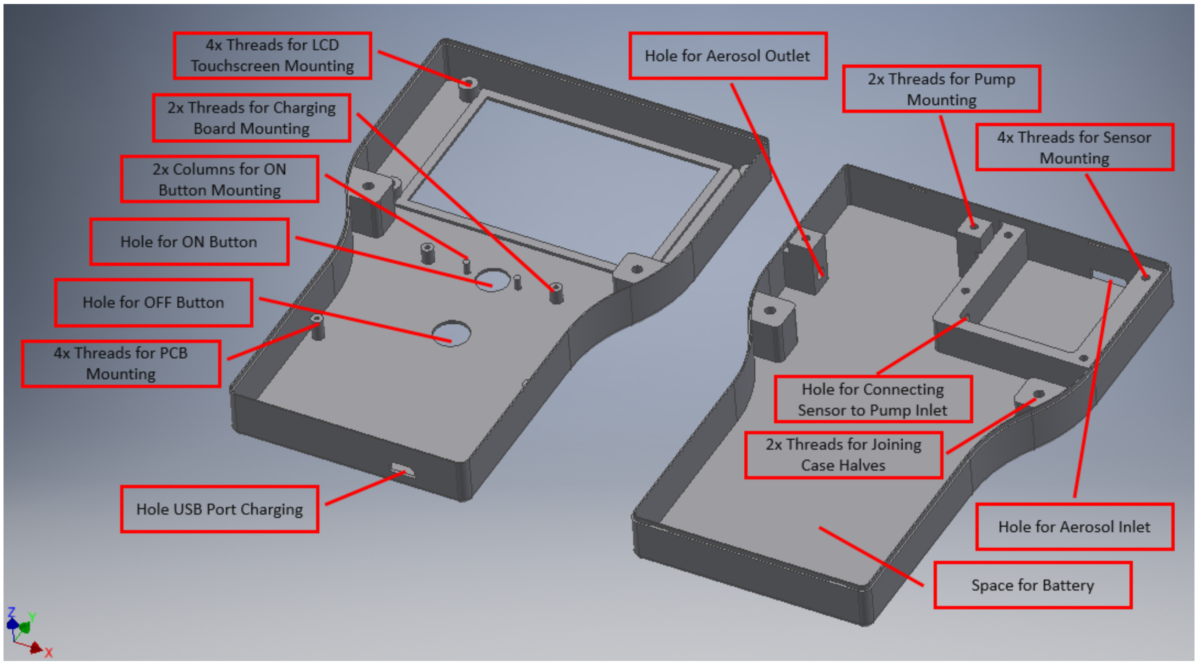

Figure C.3: Screenshot of the CAD model.

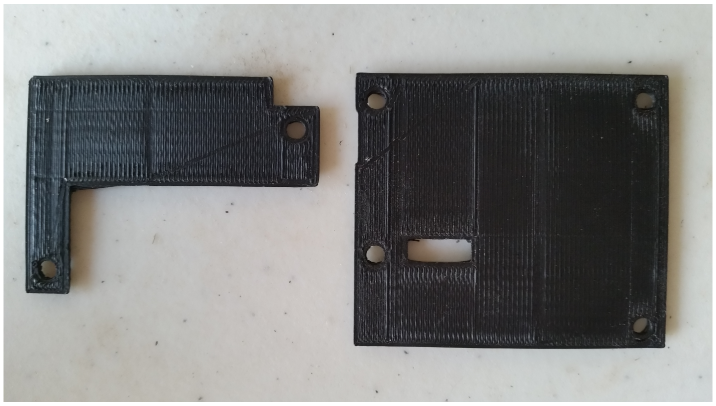

Figure C.4: Parts 3D printed to secure the pump (left) and PMS A003 (right) in the casing.

Mini Vacuum Pump

The mini vacuum pump used was the Z1312-5006-8500 manufactured by Shenzhen Yanhua Faith Technology Co., Ltd. The pump operates at a nominal voltage of 6 V and has a rated vacuum of 50 kPa at 1.5 LPM flow rate. The rated power consumption is 2 W. The pump was selected because its voltage was close to the battery output voltage of 5 V, so no step up or step down would be required. In addition, the physical shape is thin and rectangular allowing it to be compactly placed in the casing. This allowed the pump to be positioned below the LCD screen and keep the sensor casing slim.

Particle Sensor

The particle sensor selected was the PMS A003 manufactured by PlanTower. The device requires 5 V to operate and measurements are output as a serial UART signal. PlanTower sensors were the only ones found to feature six size channels; most sensors typically have one or two channels and provide only mass concentrations. An alternative to the PMS A003 was the PMS 7003 also by PlanTower. Both were tested in the laboratory and demonstrated high linearity with APS 3321. While not essential, the PMS A003 was smaller in size. The deciding factor was due to the positioning of inlet and outlet on the sensor- on the PMS A003, they were on the front and back sides, but on the PMS 7003, both inlet and outlet were on the same face. Since a connection had to be made from the sensor to pump, having the inlet and outlet on opposite sides simplified the design. The inlet could be placed adjacent to a hole on the casing, and the outlet could easily be directed to the pump.

Power

The power supply for the portable particle counter consisted of a lithium ion battery and battery power management board (BPMB). An AUKEY PB-N36 Power Bank was used with the casing removed to decrease its size as shown in Figure C.5. The battery has an output voltage of 5V via USB connection and rated capacity of 20 Ah. The BPMB ensures proper charging and discharging of the battery. The board consisted of a Micro USB port for charging, USB ports for power output, and ON button. The BPMB automatically shuts off when loads are no longer drawing current for approximately six seconds. Battery level is indicated by lights on the board which changes between three colours. In addition, the BPMB allows loads to draw current while the battery is being charged.

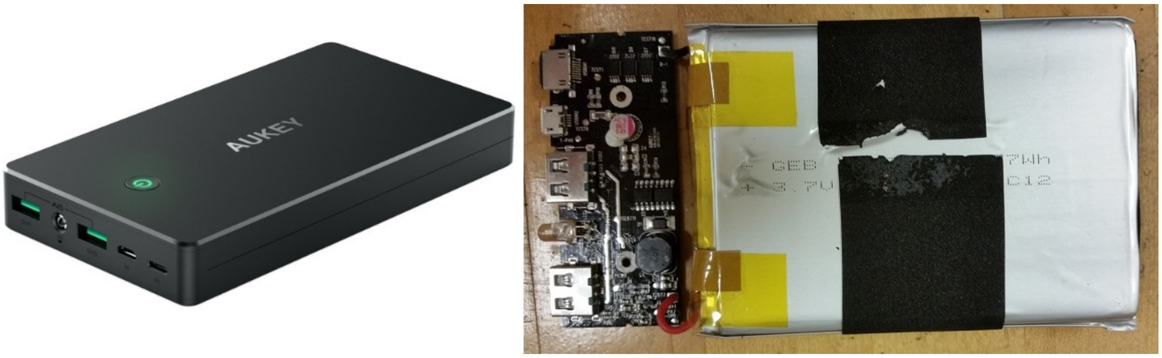

Figure C.5: Photograph of the AUKEY Power Bank with and without its casing.

One major disadvantage of using a power bank is that there is no OFF button functionality. As mentioned earlier, the power bank automatically shuts off when current is not being drawn for approximately six seconds. When used to power the portable particle counter, the load will always draw current until the battery is drained. To address the issue, a normally closed (NC) button (Model 40-3536-00, Judco Inc.) was placed between the battery power supply and loads (microcontroller, LCD screen, particle sensor, and pump). By holding down the button, the circuit is opened. After a few seconds the power bank will turn off and the user is able to release the button. No current will be drawn until the ON button is pressed again.

LCD Touchscreen

The Nextion NX4832T035 manufactured by ITEAD Intelligent Systems Co. Ltd. was chosen as the LCD touchscreen. The screen is a 3.5” TFT resistive touch display, and requires 5 V to operate. UART serial communication is used to communicate with a microcontroller. The Nextion screen was chosen due to two advantages: (i) communication is accomplished with serial UART, and (ii) the screen graphical user interface (GUI) can be programmed with a ”what you see is what you get” editor. By using UART, only two wired connections to the microcontroller is required. Other touchscreens typically use SPI communication, which requires three to four wires. In addition, the GUI editor allows the screen to be quickly programmed.

Microcontroller

The Photon manufactured by Particle was the microcontroller selected. Features include Wi-Fi connectivity, 18 general purpose input/output (GPIO) pins, built in RTC, and open source design. Built in Wi-Fi and RTC were advantages which eliminated the need for separate components. The board can also be programmed wirelessly if connected to the Internet. In addition, the Photon has two UART serial ports- this was the minimum number required in order to connect the PMS A003 and Nextion display.

Accessing the second UART serial port on the Photon adds a bit of complexity to the design. Three surface mounted devices (SMD) must be removed from the Photon, as shown in Figure C.6 (left). The UART pins are accessed on two pads located on the bottom of the Photon shown in Figure C.6 (right). By using the second UART pins, the LED light indicating the status of the Photon is disabled. This is a risk when debugging the Photon and code is not running. However, it can be mitigated by programming the Photon to display the status on a LCD screen and debugging using a separate Photon without the lights removed.

PCB

A custom PCB was designed using EAGLE software and the board layout is shown in

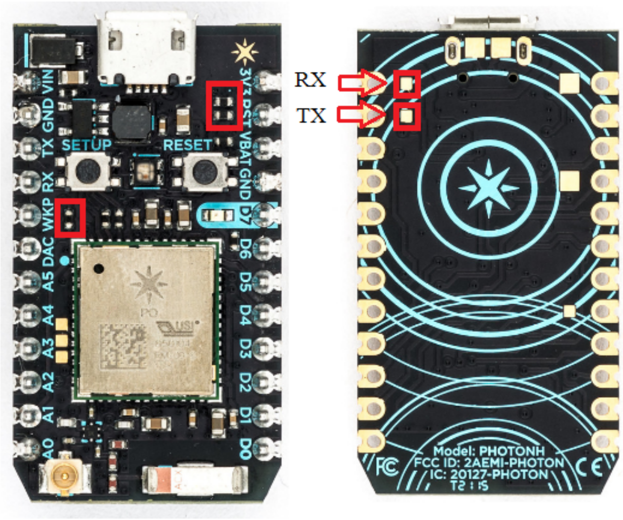

Figure C.6: Photograph showing the three SMDs removed from the Photon (left) and the second UART pins (right).

Figure C.7 (left). Afterwards, files were provided to Seeed Ltd. for manufacturing and the board can be seen in Figure C.7 (right). The board contains a Micro USB port, the Photon, a coin cell battery holder, Micro SD card holder, six pin female headers (2×), a 2×5 male header, three pull up resistors, and two piston header pins. All components except the Micro USB port was electrically connected to the Photon.

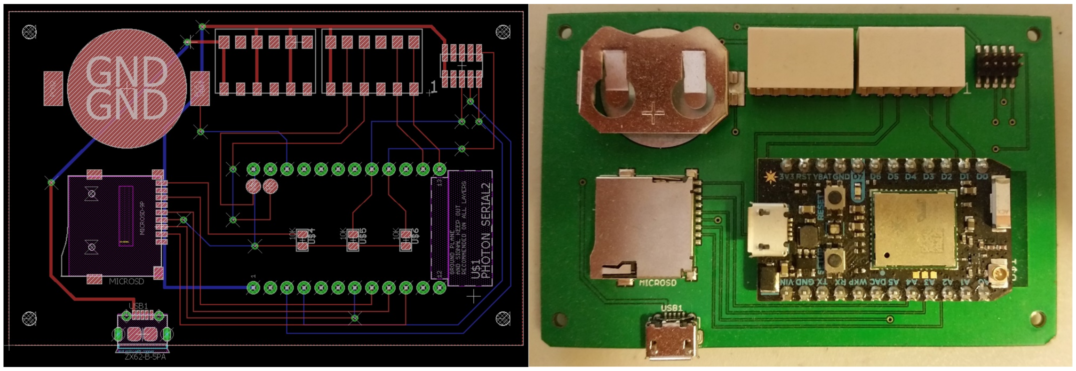

Figure C.7: Photograph of the manufactured custom PCB (right).

The Micro USB port was required for charging the battery. When the PCB is mounted in the case, the USB port will protrude though a hole allowing an external charging cable to be connected. The coin cell battery holder was required for the Photon's built in

RTC. The Micro SD card holder was required for data logging when there is no Wi-Fi connection. The six pin female headers were included so that wires could connect the PCB with the pump, Nextion screen, BPMB Micro USB charging port, and BPMB USB power supply. A 2×5 male header pin was placed on the PCB so that a cable (Product M50-9100542, Harwin Inc.) could directly connect all 10 pins on the PMS A003. Three 10 kΩ resistors were required to pull up the PMS A003 Set and Reset pins, and the Micro SD card detect pin. Two piston pins were placed on the PCB to connect the serial UART pins underneath the Photon as shown in Figure C.6 (right). Lastly, four holes were placed near the PCB corners for mounting in the case.

The wiring schematic of the custom PCB is shown in Figure C.8. The location of Female Header 1 and Female Header 2 on the physical PCB is shown in Figure C.9. The pin numbering of the female headers, 2×5 male header, and PMS A003 is also labeled.

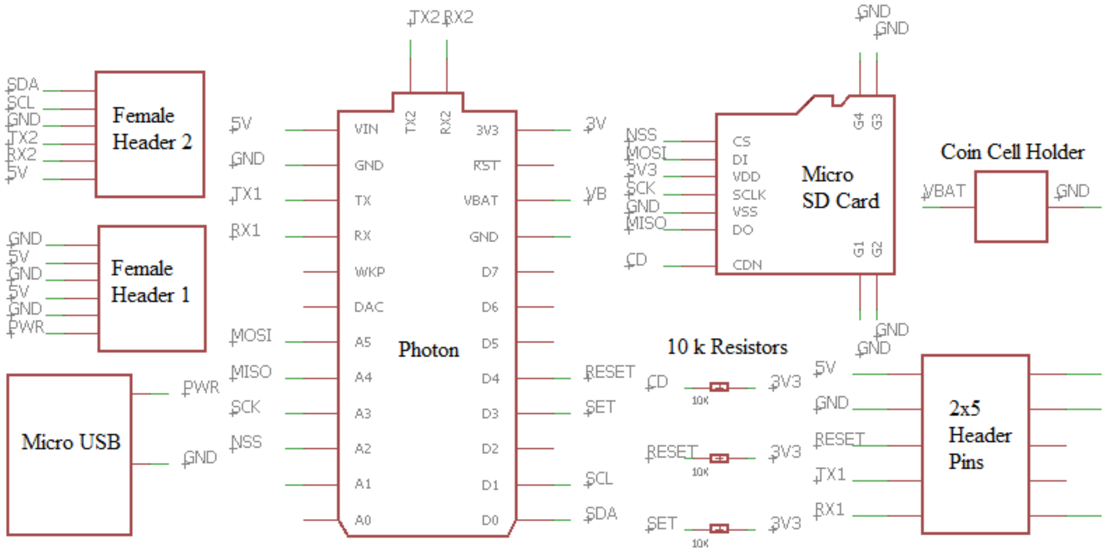

Figure C.8: Wiring schematic of the custom PCB.

The connections between the PCB and other components used in the PPC is shown in Table C.3. Note that the NC switch was placed between the BPMB USB 5 V and Pin 3 on Female Header 1 for OFF button functionality. While Pins 5 and 6 on Female

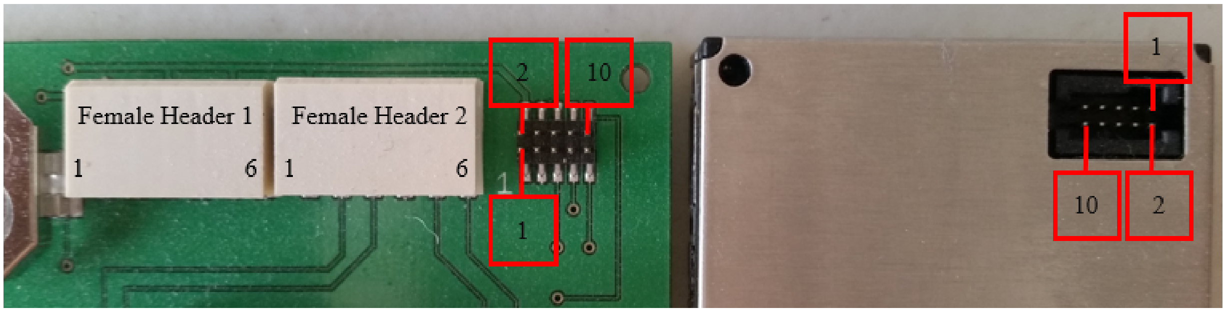

Figure C.9: Location and pins of the female headers, 2×5 male header, and PMS A003.

Header 2 were connected to the Photon, they are not currently being used in the design. Also, note that the TX pin on the Photon is connected to the RX pin on the PMS A003 / Nextion and RX on the Photon is connected to TX on the PMS A003 / Nextion.

A significant error was made in the PCB design where the Ground signal traveling from the Micro USB on the PCB to Female Header 1 Pin 2 to BPMB Micro USB should be separate from all the other Ground pins. This was not known during design of the PCB. Some current will flow even when the power bank is turned off if they are connected. As a result, Pins 1 and 2 on Female Header 1 were not connected to the BPMB Micro USB and battery charging is only possible by connecting to the BPMB Micro USB i.e. the PPC will have to be opened when charging is required. Also, another error was made in which the chip detect pin of the Micro SD card was not connected.

Table C.3: Connections between PCB and components in the PPC.

PCB Component	**Pin #**	**Signal**	**Connected Component**
Female Header 1	1	PWR	BPMB Micro USB
	2	GND	
	3	5V	NC Switch to BPMB USB
	4	GND	BPMB USB
	5	5V	Mini Vacuum Pump
	6	GND	
Female Header 2	1	5V	Nextion LCD Screen
	2	TX2 (w.r.t. Photon)	
	3	RX2 (w.r.t. Photon)	
	4	GND	
2×5 Header Pins	1	5V	PMS A003
	2	5V	
	3	GND	
	4	GND	
	5	RST	
	6	No Signal	
	7	TX1 (w.r.t. Photon)	
	8	No Signal	
	9	RX1 (w.r.t. Photon)	
	10	SET	

C.3.2 Second Iteration

A photograph of the second design iteration is shown in Figure C.10 (left) with assembled internal components (right). During testing of the first prototype, the Nextion screen ceased to function. This screenless design was quickly conceptualized to prevent delays in testing the particle sensor; tests and analysis completed in Section 3.5 were for this version. Changes were also made to improve upon the first design iteration. A complete list of components used is shown in Table C.4. The same custom PCB as in the first iteration was used, so its components can be found in Table C.2.

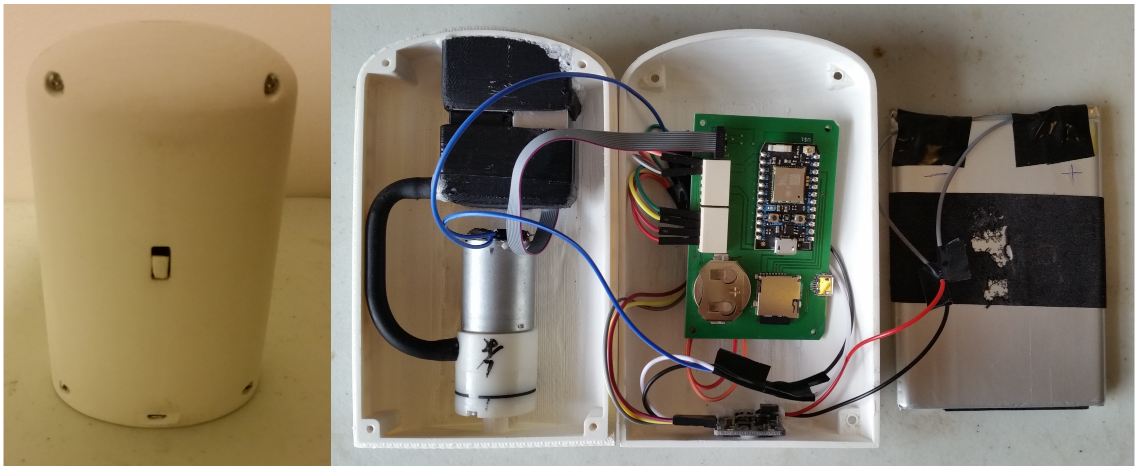

Figure C.10: Photograph of the second design iteration (left) and internal components (right).

Casing

The casing was designed similarly to the previous version. Since the design was only intended for testing the sensor and not for end use, some internal components were not mounted and FDM printing was used. An inlet and outlet adapter for the PMS A003 sensor was also printed. When adhered to the casing, the adapters create an air flow path from the case inlet to outlet and passing through the sensor.

Mini Vacuum Pump

Table C.4: List of components used in the second design iteration.

Component	**Manufacturer**	**Part Number**	**Qty.**	**Cost**
Casing	InkSmith	Custom	1	\$30
Mini Vacuum Pump	Unknown	Unknown	1	\$7
Particle Sensor	Plantower	PMS A003	1	\$34
Battery Module	Aukey	PB-N36	1	\$13
Microcontroller	Particle	Photon	1	\$29
On/Off Switch	CW Industries	GF-1123-0009	1	\$1
PCB	Seeed Ltd.	Custom	1	\$31
Coin Cell Battery	Sony	CR2032	1	\$0.70
Micro SD Card	Kingston	SDC4/8GB	1	\$9
Battery Charger	Adafruit	1000C	1	\$28
Relay	IXYS Integrated Circuits	CPC1002N	1	\$2
Misc. Hardware				
JST Cable	Adafruit	261	1	\$1
4-40×3/4” Screw	McMaster-Carr	92949A113	4	\$0.20
Barbed Fitting	McMaster-Carr	5463K53	1	\$0.60
1/8” ID Tubing	McMaster-Carr	5034K21	15 cm	\$0.30
22 AWG Wire	All Electronics	HW-50	1	\$0.50
10 Wire Connector	Harwin Inc.	M50-9100542	1	\$11.30
Total				\$200

A different vacuum pump was used in the design as shown in Figure C.11. The location of the inlet and outlet allowed the pump to be directly mounted on the casing, eliminating additional tubing. Unfortunately, no manufacturer or part number is marked on the pump, and the information online was removed before being noted. The component can easily be substituted by another 6 V vacuum pump with similar geometry.

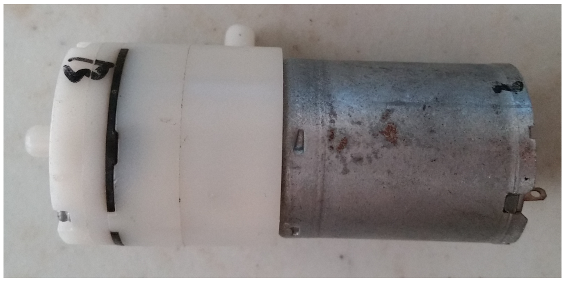

Figure C.11: Photograph of the mini vacuum pump.

Power

The Adafruit 1000C board was used to substitute the AUKEY BPMB in this design. The board includes charging protection for the battery, Micro USB charging port, and step up voltage to 5 V. However, battery discharge protection was not included. The missing feature was considered acceptable for testing the prototype, but will be essential in the final design. One of the batteries from the AUKEY Power Bank was removed for use in the prototype, which results in a rated capacity of 10 Ah. A single switch can also be connected to the board to turn off or on the power. The design resolves one of the main drawbacks of the first iteration by not requiring the user to hold down a second button to turn off the unit.

Relay

A relay was implemented in the second iteration to control power to the pump. By setting a Photon GPIO high or low, power to the pump can be turned on or off. This functionality is already built into the sensor and most LCD screens. It allows the user to pause particle counting while performing other tasks with the microcontroller such as data retrieval. This saves battery power and is a remedy to the loud pump noise.

C.4 Design Issues

Several problems still remain with the current design, which include:

- The effect of humidity on measurements should be investigated. If it is significant, design changes are required to include a humidity sensor.
- The vacuum pump is loud so substitutions should be required.

C.5 Software

Only the most important software functions for the prototype were developed and verified in this work. This includes reading data from the PMS A003, communicating with the Nextion screen, and uploading data online. The Photon is programmed using C language in the Particle online IDE, or offline Atom IDE. Programming the screen is completed in the Nextion Editor, which is similar to the VB.NET or C#. A USB to serial UART adapter or Micro SD card is required to upload code to the Nextion screen.

The Photon's Internet connectivity was verified by uploading sensor data to ThingSpeak, a service allowing users to visualize and analyze live data streams in the cloud. Setting up a ThingSpeak account to work with the PPC and using the tool to analyze data may be challenging for end users. Although plots of the streamed data are displayed, additional analysis requires MATLAB coding, so the platform is not ideal and is not considered further.

Future software development for the PPC should consider:

- Wi-Fi
  - Ability for the user to connect to new Wi-Fi networks.
  - Displaying the Wi-Fi signal strength.
- Settings
  - Adjust screen brightness.
  - Password protection.
- Calibration Algorithm
  - Calibrate the raw sensor data to accurate measurements using developed algorithm.
  - May have to consider humidity, which would require hardware modifications.
  - May require user to indicate the environment the PPC is used in to apply the proper algorithm i.e. indoor, outdoor, residential, industrial, urban, rural etc.
- Data Logging
  - Save all sensor data to the Micro SD card.
  - Automatically delete the oldest data when storage is full.
  - Ability to view stored data.
  - Automatically upload data to cloud storage when Wi-Fi enabled.
  - Ability to specify the location where PPC data was collected.
- Computer Application GUI
  - Ability to claim PPCs owned by the user.
  - Ability to view data collected with the PPC by retrieval from the cloud.
  - Perform various analysis on collected data.

Appendix D
Aerodynamic Particle Focusing and Charge Measurement

D.1 Summary

A dual purpose corona charger for particle charging and generation was developed. The device consisted of mainly off the shelf parts and required limited machining. Operation as a particle charger allows the device to be used in nanoparticle characterization instruments. As a generator, various types of particles can be produced for aerosol research. The mode of operation depends on the needle material installed on the corona charger.

The design of a submicron PSD measurement technique involving aerodynamic particle focusing and charge measurement (APF) was completed. The apparatus consisted of the developed corona charger, a 10 way valve for selecting various operating pressures, a focusing orifice, Faraday cup, and vacuum pump. The required components were procured and assembled. Software was developed to automatically take readings from all operating parameter measurement instruments.

The corona charger could neither be evaluated as a particle generator or charger due to the prolonged process of obtaining safety approvals for its use. Nevertheless, preliminary testing was completed to investigate operating pressures and the ability of the Faraday cup to detect charged particles. Results show that choked flow was not obtained in the device. Evaluation of the Faraday cup produced distinct signals depending on the orifice size selected. The results verifies the charge detection component of the APF, considering that particles were not charged and do not produce a strong signal.

CFD simulations were completed to investigate parameters affecting particle focusing characteristics of an orifice. The base simulation in the work of Middha and Wexler (2003) was replicated and results agreed well. Analysis of the model showed that focusing also depends on the initial position of the particles upstream. In addition, a wide range of particle sizes would be focused into a Faraday cup even with a small aperture of 1 mm diameter. These aspects should be addressed to improve the performance of the APF.

D.2 Introduction

The size range of particles studied by researchers span several orders of magnitude, and no single instrument is able to measure the PSD over the entire spectrum. Recently, an increasing number of studies have focused on aerosols in the nanometer size range. As a result, accurate instruments with lower detection thresholds and short measurement times are crucial for field and laboratory research. Activities related to nucleation experiments, emissions from combustion processes, and engineering of nanoparticles will benefit from improved instrumentation (Tröstl et al., 2015).

Particle charging is an important process in many aerosol applications and a great deal of research has been conducted to develop various types of particle chargers. Electrostatic forces, Brownian motion, and aerodynamic forces are phenomenons which can be exploited to measure nanoparticle size distributions. When a PSD measurement instrument utilizes electrical mobility analysis, a component for charging particles is typically required. The device generates ions to place a known charge on the particles, which can then be classified using electrostatic forces.

Particle generation is also an important process in aerosol research, and certain parameters must be considered when selecting a particle generator. Methods to generate particles include atomization, dispersion of powders, vapor-condensation, pulse spark discharge, and corona discharge. With any PSD measurement instrument developed, calibration and verification of its performance is essential. When conducted in a laboratory environment, aerosols need to be generated for testing. Generation of different particle materials, shapes, and concentrations would be desirable to fully characterize the developed instrument.

D.3 Literature Review

D.3.1 Particle Charging

Particle charging is an important procedure in many aerosol applications. During charging, ions collide with and stick to particles. As a result, the charge carried by the ion is transferred to the particle (Intra and Tippayawong, 2011). The technique is mainly used for air pollution control in electrostatic precipitators, or with instruments for measuring PSD (Grob et al., 2013). For PSD measurement, the objective is to place a known and ideally narrow distribution of electrical charge on particles (Dhaniyala, 2003).

The most important parameter of an aerosol charger is its charging efficiency, which is the fraction of particles it is able to charge. Particles which remain neutral would not be able to be manipulated by electrostatic means i.e. unable to be detected by the PSD measurement device. Other characteristics of the ideal aerosol charger would be:

- High charging efficiency.
- Produce stable and high ion concentrations.
- Not damage the particles.
- Have low particle losses.
- Not contaminate the aerosol.
- Can work at low pressures and in different gases (Intra and Tippayawong, 2011).

D.3.1.1 Classifications

Particle charging can be classified by the charge of ions present, the charging mechanism, or the source of ions, as shown in Figure D.1.

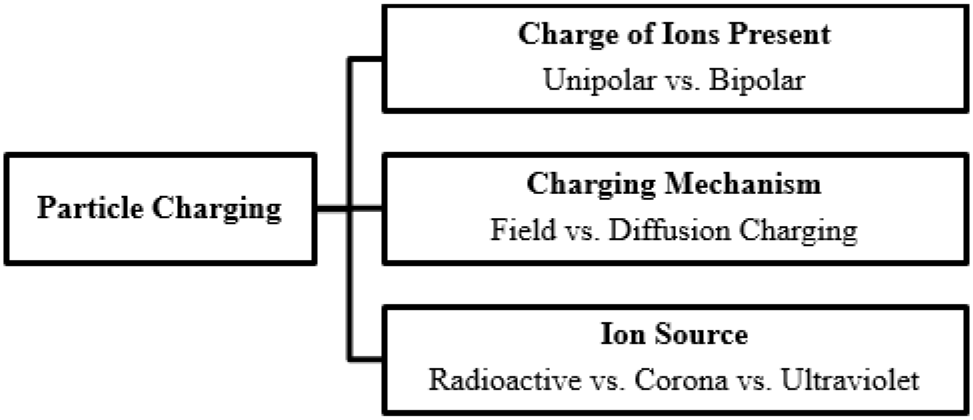

Figure D.1: Classifications of particle charging.

Charge of Ions Present

The polarity of ions present during charging can be (i) positive, (ii) negative, or (iii) both positive and negative. Particle charging is known as bipolar charging when ions of both polarities are present, and unipolar charging with only one polarity present. The advantages of bipolar charging are: (i) a charge equilibrium is established, (ii) the charge distribution is well defined, and (iii) the number of multiply charged particles is limited. However, the charging efficiency is limited and this reduces the detection limit (Grob et al., 2013). Unipolar charging will typically result in higher particle charging efficiencies because charged particles cannot recombine with particles of the opposite polarity (Intra and Tippayawong, 2011).

Charging Mechanism

Possible particle charging mechanisms are field or diffusion charging. Field charging requires the presence of an electrical field (Turner et al., 1988). Ions traveling along field lines collide with the particles and impart a charge to them. Eventually, enough ions are attached to the particle preventing new ions from colliding. In this state, the particle is said to be saturated. Small particles <1 µm are not be efficiently charged using this mechanism because they are not large enough to capture gas ions. The charge on a particle as a function of time it spends in an electric field is given by:

$$q_e(t) = \frac{12\pi\epsilon r_p^2 Et}{t + \frac{4\epsilon}{Ne\mu}} \tag{D.1}$$

where ϵ is the free space permittivity (F/m), r_p is the particle radius (m), E is the external electric field applied to the particle (V/m), t is the time spent charging, N is the ion number concentration near the particle (#/m^3), and μ is the ion mobility. From the equation, it can be seen that the saturation charge depends strongly on particle radius:

$$q_s = 12\pi\epsilon r_p^2 E \tag{D.2}$$

Diffusion charging is associated with the random motion of ions. It is related to the velocity of ions due to thermal kinetic energy. Their random motion causes collisions with particles and imparts a charge to them. This is the mechanism by which smaller particles <1 µm are charged. The charge on a particle due to unipolar diffusion charging as a function of time is given by:

$$q_d(t) = \frac{r_p kT}{e} ln\left[1 + \frac{\pi r_p \bar{c} N e^2 t}{kT}\right] \tag{D.3}$$

where k is the Boltzmann's constant (1.381×10^{-23} J/K), T is the system temperature (K), e is the electron charge, (1.602×10^{-19} C), and $\bar{c}$ is the mean thermal speed of ions (m/s). Unlike field charging, diffusion charging never reaches a limit, but the rate eventually becomes very slow.

Where both mechanisms are present, the total charge on the particle is given by:

$$q_{tot}(t) = q_e(t) + q_d(t) \tag{D.4}$$

Ion Source

To produce ions for charging, electrons must be removed from atoms. Ionization energy is the energy required to accomplish this. The amount of energy depends on the atom and number of electrons already removed (Saprykina, 2009). Radioactive radiation, photoelectric/UV-light sources, and corona charging are three methods which supply ionization energy to produce ions for charging.

Certain radioactive materials such as Americium-241 or Polonium-210 emit α or β -rays as radiation (Dhaniyala, 2003). The radiation contains enough energy so that when it interacts with gas molecules, electrons are removed from their orbit. This causes the gas molecules to become ionized (World Health Organization, 2016b). Bipolar ions are produced and can be used as a neutralizer. Unipolar charging is also possible by applying an electric field to separate positive and negative ions (Intra and Tippayawong, 2011).

Photoelectric chargers use high energy electromagnetic radiation such as ultraviolet light (UV) to charge aerosols. Known as the photoelectric effect, electrons are emitted from the surface of a metal if exposed to UV light with a frequency above a certain value, producing ions. The rate of emission is proportional to the intensity of the incident radiation if it is of a single frequency. Two ways in which UV radiation charge aerosols are by: (i) exposing the aerosol directly to light, and (ii) irradiating a metal to produce electrons for diffusion charging (Intra and Tippayawong, 2011).

In corona charging, a corona discharge is produced by a non-uniform electrostatic field between two electrodes, such as a needle and plate or concentric wire and tube. One electrode may be positive or negative, and the other grounded. In a negative corona, gas molecules break down electrically near the needle or wire. Electrons are stripped from the gas molecule as they have enough energy to escape, forming positive ions. Further away, there is a surplus of repelled electrons which are picked up by gas molecules, especially electronegative gases such as diatomic oxygen (O_2). Negative ions are formed, which get collected by the particles (Intra and Tippayawong, 2011; Anderson, 2016).

D.3.1.2 Existing Particle Charging Devices

Adachi et al. (1985) developed a radioactive unipolar charger, as shown in Figure D.2. The upper and lower walls act as electrodes when a DC voltage is applied to the lower wall. During operation, bipolar ions fill the space around the radioactive source. Either positive or negative ions can be drawn away into the aerosol stream above, depending on the polarity of the applied DC voltage. Particles 4 to 100 nm in diameter were charged in the experiments, and the results were in good agreement with Fuchs' limiting-sphere theory (Intra and Tippayawong, 2011).

In another work, Chen and Pui (1999) developed a radioactive unipolar charger for 3 to 50 nm particles. Bipolar ions were generated in the ion production zone using Polonium-210. An electric field separates positive and negative ions, and focuses the selected unipolar ions towards the center of the charger. A uniform electric field produced by a series of ringed electrodes draws the unipolar ions charging zone. Sheath air also surrounds the aerosol to minimize particle loss (Intra and Tippayawong, 2011).

Matter et al. (1995) developed a charger by exposing particles directly to UV light from an excimer lamp, as shown in Figure D.3. The lamp consisted of two coaxial quartz glass tubes sealed at each end, and could emit wavelengths between 172 and 258 nm depending on the gas filling. Particles flowing through were strongly irradiated and became positively charged. Emitted electrons attach to oxygen molecules and produce negative

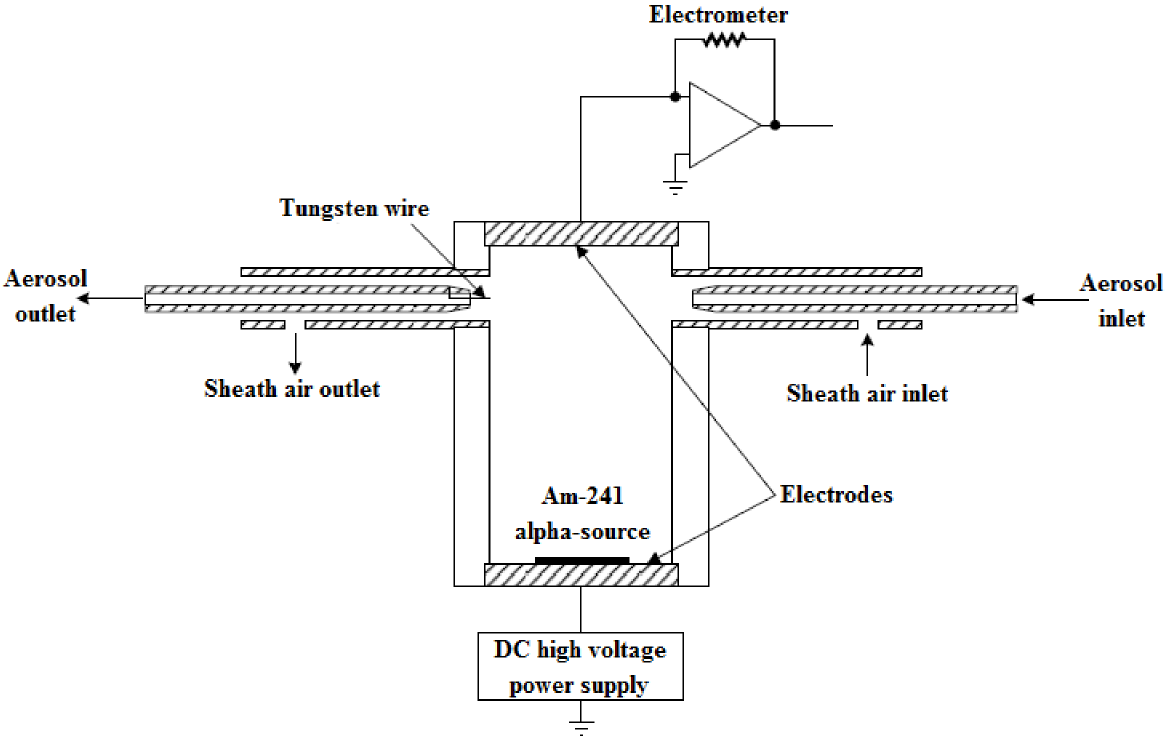

Figure D.2: Schematic of radioactive charger developed by Adachi et al. (1985).

ions. They could be removed with a weak electric field in the precipitator of negative charges. Particles were filtered, and the corresponding current was measured to obtain experimental data. Results showed that there were great variations in charge distribution depending on particle size, composition, and surface state (Intra and Tippayawong, 2011).

Grob et al. (2013) developed a indirect unipolar UV photo-charger for ultra-fine aerosol particles. Glassy carbon was used as the photo-emitter because of its very inert surface, ensuring stable electron emission. The low pressure Mercury lamp radiated UV light having photon energy between the ionization threshold of the particles and photo-emitter surface. A small DC voltage was applied to assist electrons escape the emitter for increased ion concentrations. Unipolar charging then occurs as particles collide with these ions. The charging efficiency was found to be in the range of 20 to 70% for particle sizes of 20 to 100 nm, which is comparable to corona chargers. For the carbon and NaCl particles

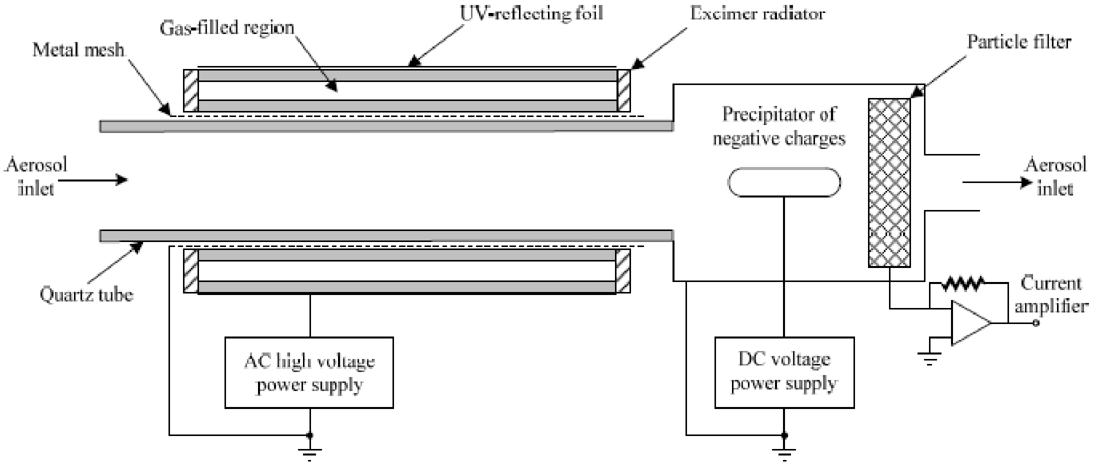

Figure D.3: Schematic of direct photoelectric charger developed by Matter et al. (1995).

studied, no direct photoelectron emission was observed, but this was not the case with particles from a flame soot generator. It was believed that the soot particles had an ionization energy low enough to be directly ionized, or some light with higher energies were not completely absorbed by the lamp.

Cheng et al. (1997) developed a corona charger employing gold wires as shown in Figure D.4. The aerosol flowed parallel to the wires, six of which were mounted around a Teflon rod holder and maintained at over 5 kV. Gold was used as the wire material due to its resistance to oxidation. Electrostatic particle losses to the wall were minimized by the transpiring air flow. A sheath air flow prevented particles from entering the high ion density region. The authors were able to achieve particle losses below 5% using sufficient transpiring air flow rate (Intra and Tippayawong, 2011).

Medved et al. (2000) developed a needle based corona charger as shown in Figure D.5. Unipolar ions were generated at a platinum corona needle tip located in a chamber, where an airflow pushed the ions through an orifice into the turbulent charging zone. Aerosol enters the charging zone through a separate opposing flow and this creates turbulent conditions. The design was found to charge particles more efficiently due to diffusion and the two jets mixing. Finally charged particles leaves the chamber through an outlet (Intra

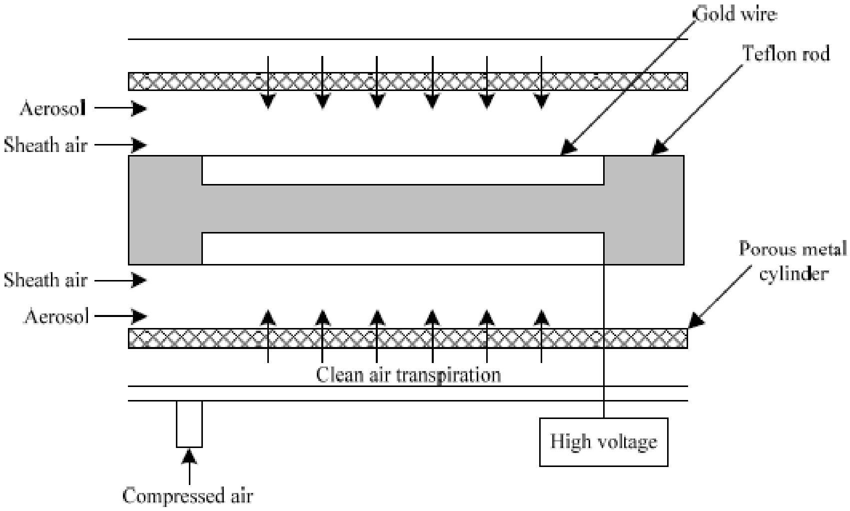

Figure D.4: Schematic of corona charger developed by Cheng et al. (1997).

and Tippayawong, 2011).

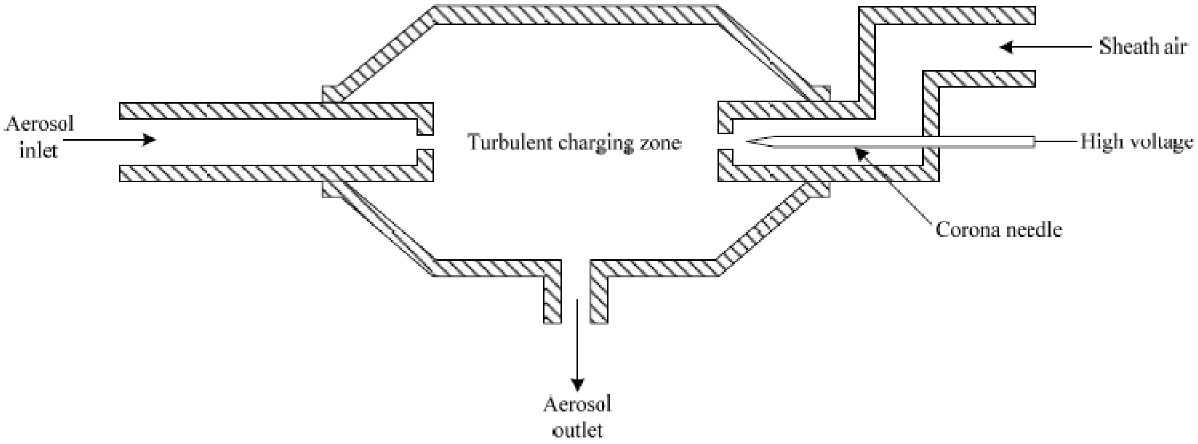

Figure D.5: Schematic of corona charger developed by Medved et al. (2000).

D.3.2 Particle Generation

Particle generation is commonly required in filter testing, instrument testing, and research. The effectiveness of air pollution control devices are highly dependent on the size distribution of aerosols. During development or evaluation of PSD measurement instruments, laboratory generated aerosols are typically used to gauge their performance before further testing. Thus systems which produce aerosols with reproducibility, reliability, durability, and stability would be useful in these applications (Lee et al., 2008). Several parameters must be considered when selecting a generator for an application:

- Dispersity
    - Polydisperse vs. Monodisperse
- Phase
    - Solid vs. Liquid
- Material
    - i.e. Road Test Dust, Sodium Chloride (NaCl), Gold
- Size Distribution
    - i.e. Log-Normal, Bimodal
- Size Range
- Concentration
- Flow Rate

Atomization

The Aerosol Generator 3076 manufactured by TSI Inc. (Shoreview, MN, USA) produces particles through atomization. As shown in Figure D.6, compressed air expands through an orifice to form a high-velocity jet. A liquid mixture containing the material to atomize is drawn into an atomizing section, and is atomized by the jet. Larger droplets collide with the wall opposite the jet and excess liquid is drained away. The result is a fine spray leaving the Atomizer at the top.

Different materials such as NaCl, sugar, uranine, methylene sucrose, dioctyl phthalate, olive oil, or oleic acid can be used as the solute to generate polydisperse particles. The Model 3076 can also be used to generate monodisperse particles by atomizing a hydrosol containing monodisperse solid particles such as polystyrene latex. Generated particles have a size range of 0.01 to 2.0 µm and concentrations greater than $10^7/\text{cm}^3$.

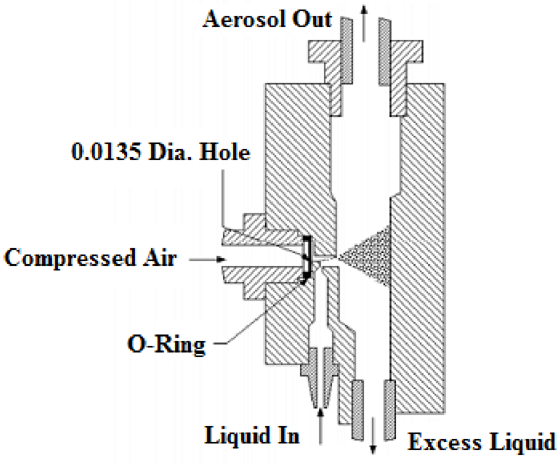

Figure D.6: Schematic of the Model 3076 atomizer assembly block (TSI Inc., 2005).

Dispersion of Powders

Materials in powder form can be dispersed to generate aerosols. If good particle dispersion and constant concentration are not important, methods such as blowing dust from a tube with air or stirring dust in a blender can be used. Deagglomeration of particles may also be another important consideration when powders are used (Marple et al., 1978). Most powder dispersion systems consist of a constant rate feeder and entrainment apparatus. The Wright dust feeder is an example where compacted powder in a rotating cup is scraped and entrained into a carrier gas flow. An impactor removes large agglomerated particles from the gas (Flagan, 2007).

Marple et al. (1978) developed a dust generator using a fluidized bed to throughly deagglomerate the particles. Powder to be aerosolized is placed in a holding chamber and transported by a chain conveyor into the fluidized bed. The bed consisted of a 1.5 cm thick layer of 100 µm brass beads placed in a 5.1 cm diameter chamber. Beads are supported by a mesh screen placed above an air plenum. Air flows through the fluidized bed, disperses the powder, and carries it to the elutriation chamber. Brass beads fall back into the bed due to their large size.

Coal, silica, potash, rock, and Arizona road dust have been successfully generated by the researchers. The Fluidized Bed Aerosol Generator Model 3400A manufactured by TSI Inc. is a commercial product of this device. Generated particles have a size range of 0.5 to 40 µm and concentrations of 10 to 100 mg/m^3 (TSI Inc., 2014).

Vaporization-Condensation

In vapor-condensation methods, metals or salts are heated using electrical resistance heaters, induction furnaces, or infrared ovens to temperatures at which they will evaporate. The hot gases are cooled and solid particles form due to condensation and nucleation of the vapors. Particle sizes are generally below 1 µm, and rapid cooling favors formation of smaller particles <0.1 µm (Flagan, 2007).

Pulse Spark Discharge

The pulse spark discharge method generates particles by evaporation and condensation of an electrode material (Efimov et al., 2013). In the spark generator developed by Mäkelä et al. (1992) electrode materials such as copper, silver, gold, carbon, and nickel-chrome could be used. Carrier gas flowed between two sharp electrodes placed approximately 5 mm from each other. Pulses with a frequency of 1-200 Hz was generated between the electrodes. A power supply generates voltages in the range of 30 kV and spark discharges atomizes the electrode material. Average diameters of the generated particles could be varied by adjusting the distance between electrodes. In the study, nanoparticles with mean diameters from 2 to 15 nm were synthesized.

Kim and Chang (2005) developed a generator with a high precision trigger pulse circuit and an ignition coil to obtain stable and reproducible spark discharge, as shown in Figure D.7. The discharge section was a 80 mm ID, 250 mm long cross pyrex tube. Two 2 mm diameter copper electrodes were placed in cross flow with the air. The gap distance was varied from 10 to 30 mm and the pulse frequency used in the experiments was 50 Hz.

Peak voltages and currents were in the range of 40 kV and 0.7 mA, respectively. The average diameter of generated particles could be controlled from 0.2 to 4.0 µm.

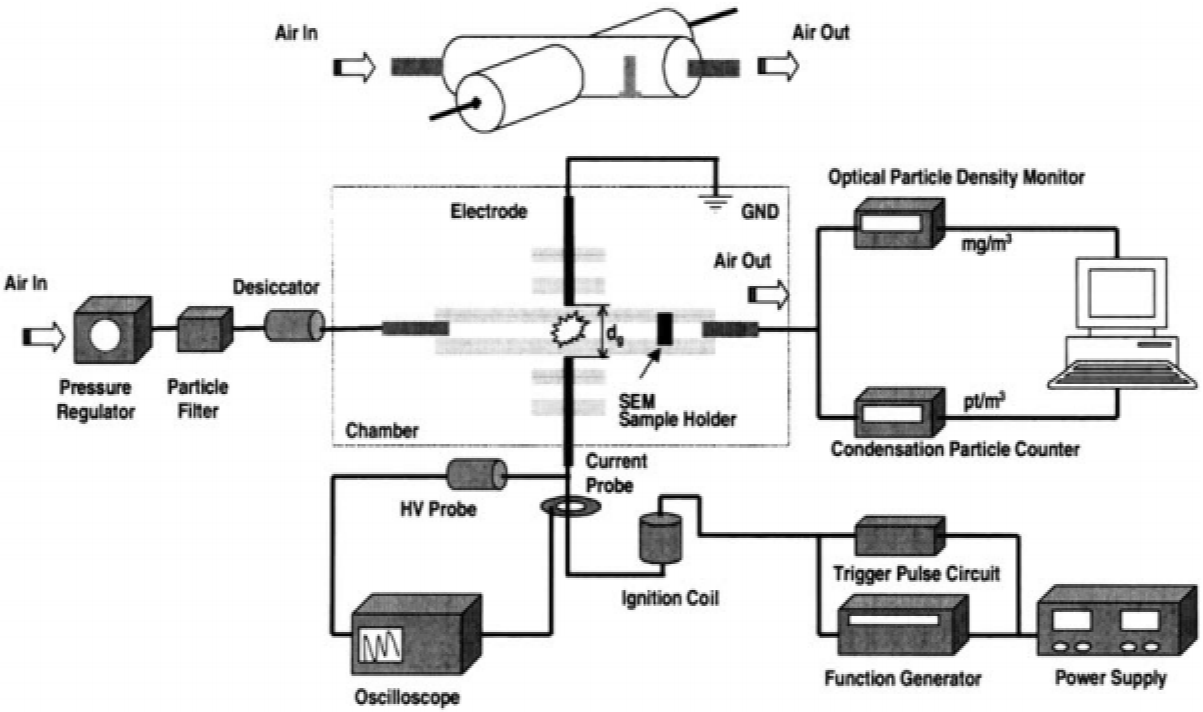

Figure D.7: Setup for the spark discharge generator developed by Kim and Chang (2005).

Corona Discharge

It is known that particles are generated during corona charging as described in Section D.3.1.1. In the work of Medved et al. (2000), the researchers made an effort to reduce the amount of ultrafine particles generated by their corona charger. A platinum needle tip was used, which does not corrode, oxidize, or vaporize easily to form particles. Investigation of particle generation by the device showed low production. While this phenomenon is undesirable in PSD measurement applications, it can be exploited for particle generation.

Saprykina (2009) investigated particle generation in a needle and plate corona charger, and found that it occurred for voltages over 4 kV in negative coronas. Particles with mean diameters of 9 to 110 nm were generated and concentrations were as high as 150,000/cm^3.

Energy dispersive x-ray analysis (EDX) revealed the presence of gold, oxygen and carbon in the generated particles. This was not unexpected since the corona needle was made of gold. It was suggested that electrical forces propelled ions to collide with the needle and knock off material to form the particles.

Similar to pulse spark discharge, particles of various compositions could be generated by substituting the electrode material. In this application, metals which do corrode, oxidize, or vaporize easily would be desirable.

D.3.3 Aerodynamic Particle Focusing

Aerodynamic particle focusing (APF) is a method for nanoparticle characterization using aerodynamic forces. Aerosol is first charged and then focused through an orifice. Particles with a specific Stokes number travel along the axis, while other particles follow a curved trajectory. An electrometer measures the charge of focused particles, which is related to concentration. By changing the upstream pressure, particles with different Stokes number are focused and a PSD can be obtained.

An APF prototype has been previously developed by Saprykina (2009). In the previous study, NaCl nanoparticles were generated for experimental testing and the prototype was calibrated against a commercial SMPS. The APF was capable of measuring particles with diameters from 39 nm to 281 nm. The overall average accuracy was 10% for particle diameter, and 29% for the corresponding number concentration. Conditions for nanoparticle generation and filtration in the corona charger was also investigated, and it was found a operation voltage below 4 kV minimized these phenomenons.

An expression for the focused particle diameter as a function of operating parameters is now derived. The Stokes number of focused particles is given by Equation 2.5. Here, the characteristic dimension d_c is the orifice diameter and u_o is the gas sonic velocity.

The maximum particle diameter d_p^m which is focused corresponds to when C_c equals 1:

$$Stk = \frac{\rho_p (d_p^m)^2 u_o}{18 \mu d_c} \tag{D.5}$$

Setting Equations 2.5 and D.5 equal, the following expression for optimally focused particle diameter is obtained:

$$d_p = \sqrt{\frac{(d_p^m)^2}{C_c}} \tag{D.6}$$

Using the expression $C_c = 1 + 1.657Kn = 1 + 1.657(\frac{2\lambda}{d_p})$ for Cunningham slip correction and substituting in Equation D.6:

$$d_p = \sqrt{(1.657\lambda)^2 + (d_p^m)^2} - 1.657\lambda \tag{D.7}$$

From gas molecular dynamics, the mean free path λ is calculated as:

$$\lambda = \frac{\mu}{P\sqrt{2M/\pi RT}} \tag{D.8}$$

where P is the pressure before the focusing orifice, M is the molecular weight of the gas, R is the universal gas constant (8.314 J/K·mol), and T is temperature. Substituting Equations D.5 (rearranged for d_p^m) and D.8 into D.7, the final expression for d_p is obtained:

$$d_p = \sqrt{\left(\frac{1.657\mu}{P\sqrt{2M/\pi RT}}\right)^2 + \left(\frac{18\mu d_c Stk^*}{\rho_p u_o}\right)^2} - \left(\frac{1.657\mu}{P\sqrt{2M/\pi RT}}\right) \tag{D.9}$$

From Equation D.9, changing the pressure is the most convenient method to change d_p. It is difficult to design a variable diameter orifice to vary d_f or Stk^*. Other parameters such as u_o is fixed because focusing only takes place in choked flow (Saprykina, 2009).

Upstream of the focusing orifice, unipolar diffusion charging would place a charge on the particles given by Equation D.3. Field charging can be neglected for small particles.

The particle number concentration N_p ($\#/\mathrm{m}^3$) is directly proportional to current measured due to the focused particles:

$$N_p = \frac{I}{Qq_d(t)e} \tag{D.10}$$

where I is the measured current and Q is the gas flow rate in the focusing orifice (Tan et al., 2014). Substituting Equation D.3 into D.10, an expression for concentration in terms of measurable and known quantities is obtained:

$$N_p = \frac{I}{(d_p kTQ/2)\ln\left[1 + (\pi d_p \bar{c} N e^2 t/2kT)\right]} \tag{D.11}$$

Using this relation requires particles to be maximally charged. Thus a charger producing a high concentration of unipolar ions is desirable. The ion concentration and time spent charging will depend on the specific charger employed.

D.3.4 Knowledge Gap and Research Needed

While particle charging is an important process in aerosol research, there lacks commercially available devices. Those on the market are expensive and their performance under various operating conditions are not well characterized. Chargers developed by researchers are difficult to replicate and manufacture as parts require machining. Radioactive chargers require handling of radioactive material which presents hazards and certification difficulties. UV chargers require careful control of electrical fields to produce sufficient concentrations of ions. From the reviewed charging devices, corona chargers appear easiest to build and operate. If components can be procured off the shelf, costs and manufacturing complexity would be further reduced.

The process of particle generation for aerosol studies can be improved by providing a greater availability of particle sources. This would allow researchers to evaluate the effects of a wider range of particles for the application of interest. For each type of particle generation device, only certain materials can be used, such as fine powders for fluidized beds or specific homogeneous mixtures for atomizers. Using a corona charger for particle generation provides new possibilities since the needle material can be easily substituted to generate particles with different compositions. In addition, the corona charger can also be used for charging particles which offers two important processes for aerosol research in one device. Although the process is similar to pulse spark discharge, the method is easier to operate since a function generator is not required. Thus, there exists the need for a well characterized particle charging and generation device that is easy to manufacture.

Several limitations still existed with the APF after conclusion of the study, including particle losses due to filtration in the corona charger, deposition in the system, and defocusing. The prototype was also unable to differentiate between particle shapes and agglomerates. Theoretically particles as small as 3 nm could be focused, with a bandwidth of about 2 nm. Special devices such as rectangular lenses before focusing, and skimmers afterwards should yield improvements. CFD modeling would be beneficial for better understanding of effective particle focusing. A more powerful vacuum pump would achieving lower pressures and measure particle sizes below 40 nm. To obtain a more continuous PSD, more pressure reducing orifices or a pump with variable performance should be employed. The corona charger can also be modified or substituted with other devices capable of producing high ion concentrations with low particle filtration. Thus there exists the need to further refine the APF for improved performance in characterizing nanoparticles.

D.4 Materials and Method

D.4.1 Corona Charger

A corona charger was designed comprising of mostly off the shelf parts as shown in Figure D.8. This configuration of the corona charger was used in all experimental tests in this work. At the center of the device is a 5-way cross with 1.33” CF flanges (A&N Corporation, Model 133-075-5X). The cross is a standard part and is available from a variety of manufacturers. CF flange to Swagelok adapters (A&N Corporation, Model 133X25SWG) were connected to two opposite ends of the cross, which served as inlet and outlet for airflow. The needle and ground plate was placed perpendicular such that cross flow was obtained during operation. A glass view port (A&N Corporation, Model 133-ZVP) was connected to the top of the cross. This allowed confirmation of the distance between needle and plate during operation, and ensured contact is not made as a safety feature.

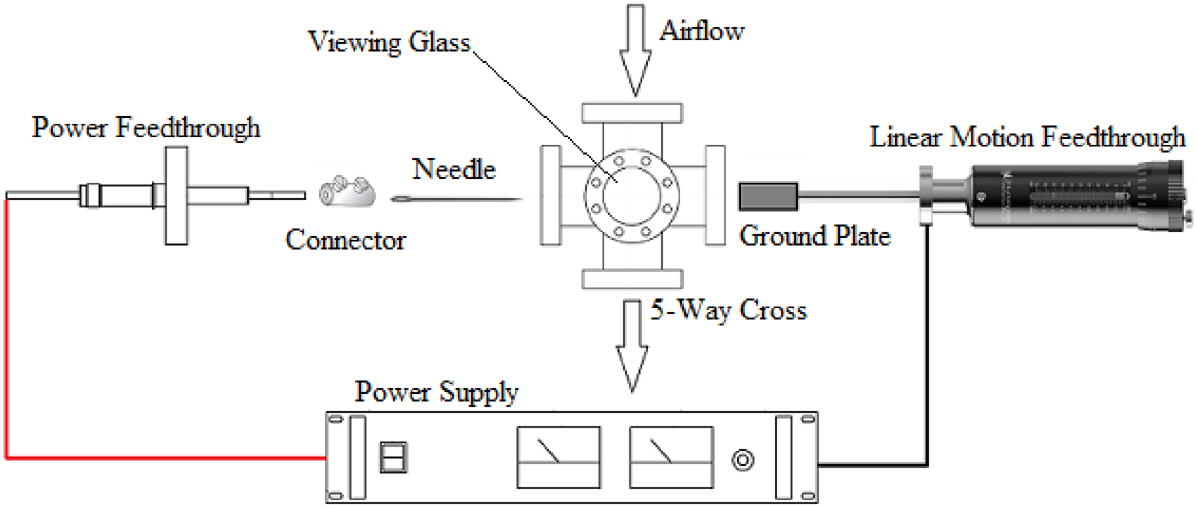

Figure D.8: Schematic diagram of the corona charger.

The atmospheric side of a 20 kV power feedthrough (MPF Products Inc., Model

A0533-2-CF) was connected to the high voltage output of the power supply (Glassman High Voltage, Model PS/EL30R01.5). The copper conductor on the vacuum side of the power feedthrough was connected to an in-line barrel connector and then to the needle. The copper was cut such that when assembled, the needle tip is approximately at the center of the 5-way cross.

A grounded linear motion feedthrough (Huntington Mechanical Labs, Model L-2111-1) was used to adjust the distance between needle and ground plate. A 10 mm diameter, 20 mm long steel rod was attached to the end of the feedthrough shaft to act as the ground plate. A x mm blind hole was drilled in the center of the steel rod so that the shaft tip could be inserted. Glue was used to bond the ground plate to feedthrough shaft. The shaft was cut such that when fully extended, the ground plate was approximately 1 mm from the needle tip. The feedthrough has a stroke of 1".

As seen from the schematic, the corona charger design is comprised of mainly readily available, off the shelf parts. Only two simple cuts to the power feedthrough conductor and motion feedthrough shaft is required. The only machining needed is for a simple ground plate, making the design easy to manufacture. Operation as a particle charger or generator depends on the needle used in the device. When particle charging is desired, a needle material resistant to oxidation such as gold or platinum should be used to reduce particle production. On the contrary, if particle generation is required a more easily oxidized needle material should be used instead.

D.4.2 APF Prototype

A schematic of the designed APF is shown in Figure D.9. Note that the device would begin with the corona charger in Figure D.8, but is not shown in Figure D.9. The setup begins with air entering a flow meter (TSI Inc., Model 4045) and then a 10-way multi-position valve (VICI, Model EMTVLSD10MWE2). The valve consisted of one inlet, and 10 possible outlet paths. Each outlet path was connected to a brass orifice (O'Keefe Controls, Type M) with diameters of 6, 8, 10, 12, 14, 16, 18, 20, 22, and 24 thousandths of an inch. Every orifice was then installed onto a 2.75" CF flange manifold.

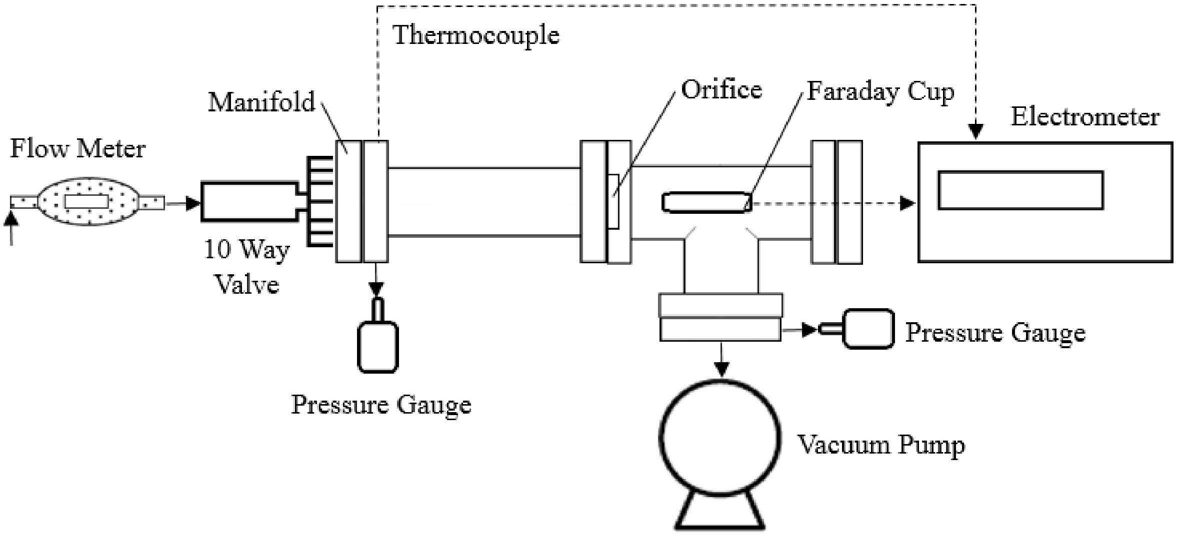

Figure D.9: Schematic of the APF.

Proceeding the manifold was a custom ordered 8" long low pressure channel with 0.75" tube diameter. The flange on the opposite end of the channel was a 2.75" to 1.33" zero-length reducer. Both 2.75" and 1.33" mates were on the same side of the flange. This allowed a 1.33" end flange to be connected as the orifice, as well as a 2.75" tee fitting. The orifice was machined from an off the shelf part to be approximately 2 mm thick and contain a 3 mm hole.

A Faraday cup (Kimball Physics, Model FC-66) was placed approximately 10 mm in front of the focusing orifice on the downstream side. It was connected to an electrometer (Keithley, Model 6517B) via BNC coaxial cable and electrical feedthrough flange. At the end of the system was the vacuum pump (Agilent Technologies, Model DS40M). The pump's performance was expected to be equal or better than the one used in the work of Saprykina (2009). Pressure gauges (MKS Instruments, Model 910 DualTrans) were also installed before and after the orifice. Temperature inside the low pressure channel was measured with a Type K thermocouple connected to the electrometer.

The flow meter, electrometer, multi-position valve, and pressure gauges were all connected to a computer for data acquisition and control. All instruments communicated via RS-232 and adapters were used to convert to USB. A program was written using VB.NET to sample and log data, and control the multi-position valve.

D.4.3 Assessment Procedure

The proposed test setup for evaluating the corona charger as a particle generator is shown in Figure D.10. Compressed air is supplied to an air filter and dryer (TSI Inc., Filtered Air Supply 3074B). A mass flow meter (TSI Inc., Mass Flowmeter 4045) measures the flow rate and pressure of the air supply. The corona charger is set up as in Figure D.8, with outlet to the SMPS+E (GRIMM Aerosol Technik, Model 7.80).

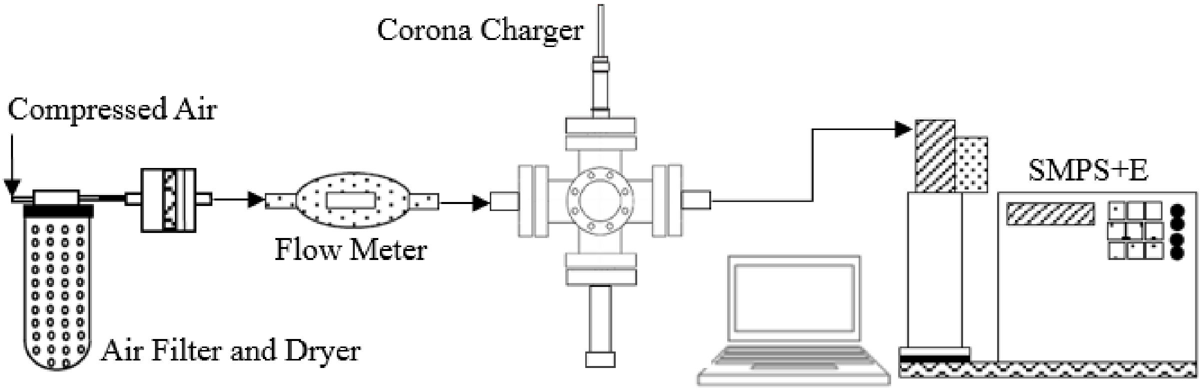

Figure D.10: Test setup for evaluating corona charger particle generation.

Extreme difficulty lied in obtaining high voltage safety approval to operate the corona charger due to stringent regulations. These delays prevented the corona charger from being evaluated in this work as both a particle generator and charger for the APF. Thus only preliminary experiments were conducted to evaluate the performance of the APF.

Also during the experiments, only eight out of the ten orifices were available for testing.

Since particle focusing only occurs under choked flow conditions, pressures inside the device was investigated. The APF was operated and pressures before and after the orifice was recorded for different orifices selected on the multi-position valve. Choked flow was verified if the downstream to upstream pressure ratio was less than 0.528.

The ability of the Faraday cup to detect particles was also verified. NaCl nanoparticles were generated in a similar manner as shown in Figure 3.4. However, aerosol leaving the diffusion dryer entered the flow meter as shown in Figure D.9 instead of a test chamber. The APF was operated and the current measured by the electrometer was recorded for different orifices selected on the multi-position valve. The procedure was repeated for a total of nine times.

D.4.4 APF Preliminary Results

The upstream and downstream pressures in the APF versus orifice size selected is shown in Figure D.11. While low pressures were achieved, the downstream to upstream pressure ratios were far from the critical value of 0.528. The reason may be due to the pump having insufficient flow rate. Although a solution to achieve choked flow was to reduce the diameter of the orifice hole, the remedy would result in less particles entering the Faraday cup and exceed the limit of detection of the electrometer.

The current measured by the electrometer versus orifice size selected is shown in Figure D.12. Considering that particles were not charged, a response was still obtained, which indicates that the electrometer has a sufficient limit of detection for the application. Precise measurements were observed throughout the nine iterations, verifying the ability of the Faraday cup to detect charged particles.

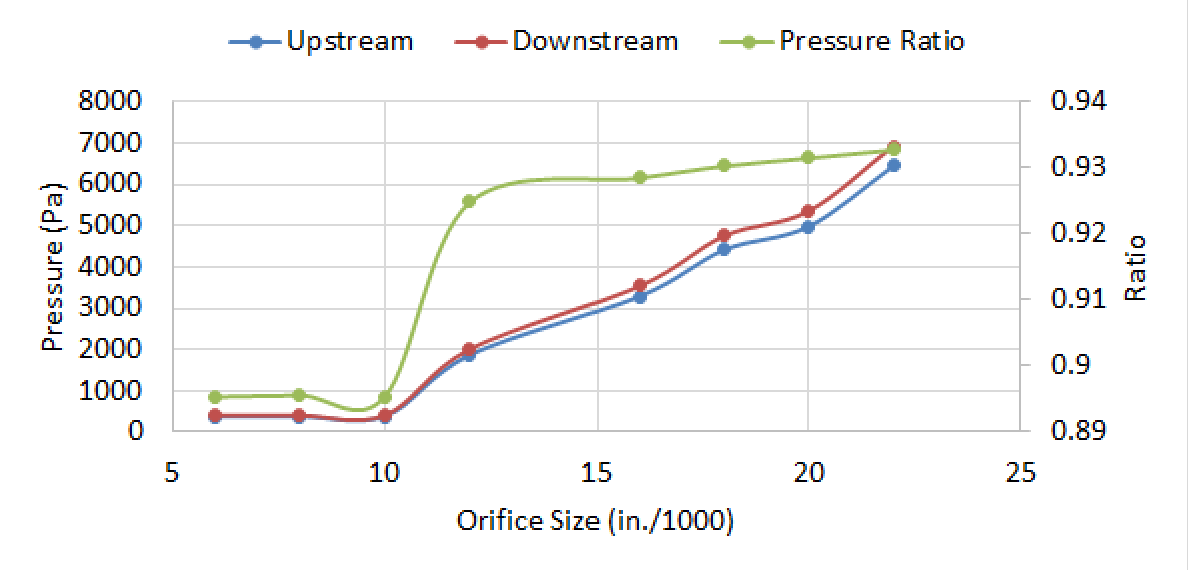

Figure D.11: Plot of pressures in the APF versus orifice size.

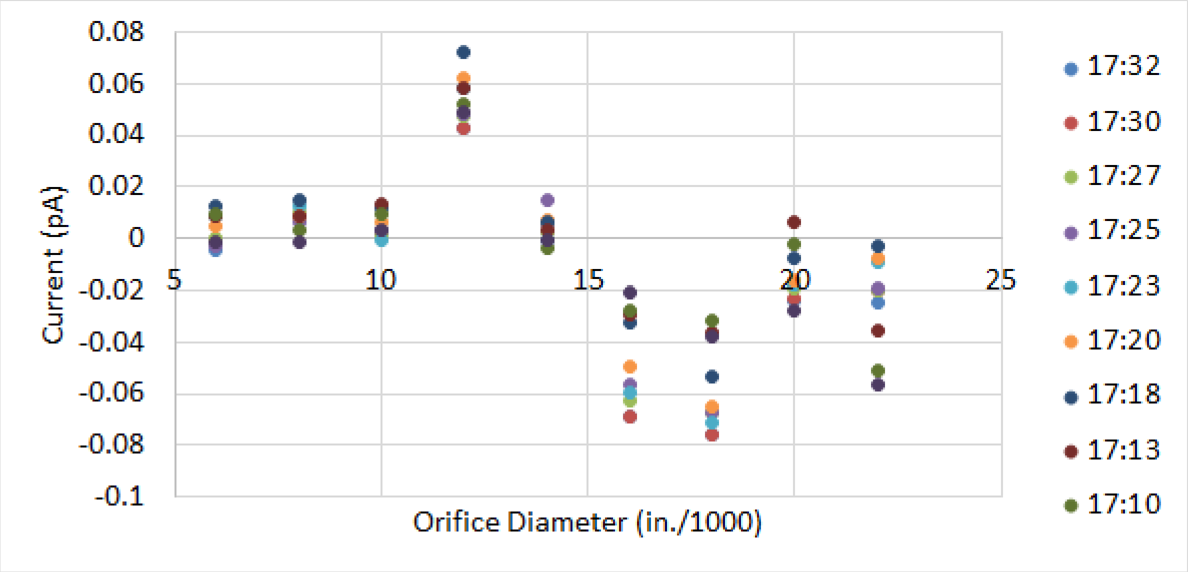

Figure D.12: Plot of current measured versus orifice size.

D.5 CFD Simulations

CFD simulations were completed to gain additional insight into the focusing effect of the orifice and potentially make improvements to its geometry. The ideal orifice would focus only particles within a narrow size range. In addition, all particles within the size range would be focused regardless of their position upstream. It follows that particles outside the size range would experience large deflections from the centerline immediately after the orifice. Middha and Wexler (2003) studied precisely this effect, where nanoparticle laden choked flow through an orifice was simulated using CFD. This work attempts to reproduce the results of Figure 3b from Middha and Wexler (2003). The model will be used as a baseline for future studies improving the performance of APF.

D.5.1 Methods

Geometry

The geometry and dimensions of the domain is shown in Figure D.13. The orifice was 3 mm in diameter and 1.6 mm thick. A length of 50 mm before and after the orifice was simulated, and the inner diameter of the tube was 35 mm in diameter. Dotted lines in the Figure show how the domain was divided into four areas of different mesh densities, which are labeled. The model was simulated as a 2D axisymmetric problem.

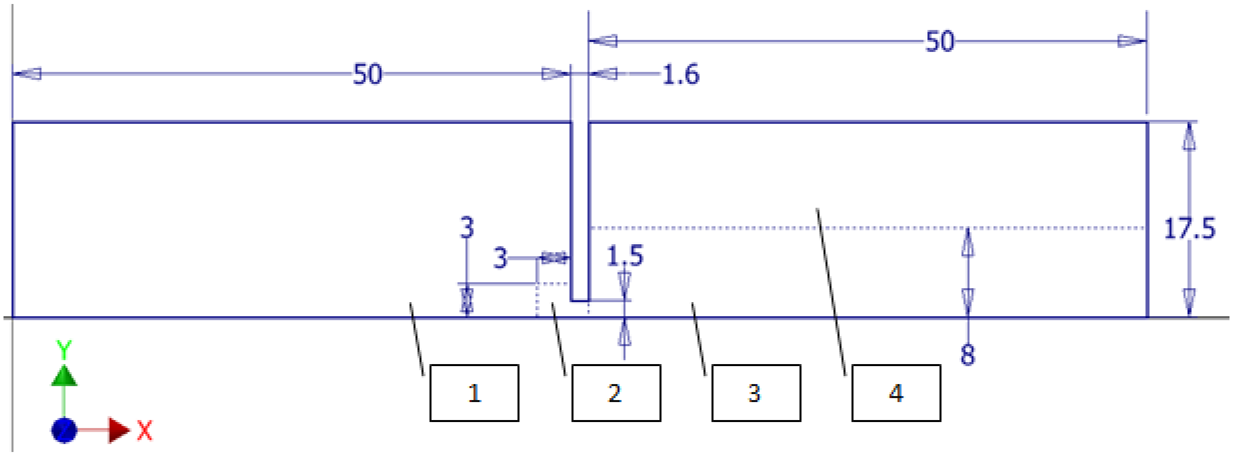

Figure D.13: Geometry and dimensions of the CFD model (mm).

Mesh

A screenshot of the model mesh is shown in Figure D.14. Referring to Figure D.13, elements in area 1 were set to 0.6×0.6 mm. Area 2 elements were set to 0.2×0.2 mm due to flow acceleration in the x and y directions. Area 3 elements were 0.5×0.2 mm due to high velocity gradients in the y direction. Lastly, area 4 elements were 0.5×0.5 mm with a bias factor of 5 in the vertical direction. Face meshing was applied to the entire mesh to obtain elements with less skew. The maximum orthogonal skew and aspect ratio was 0.15 and 3.82, respectively. In total, there were 9,500 elements in the domain.

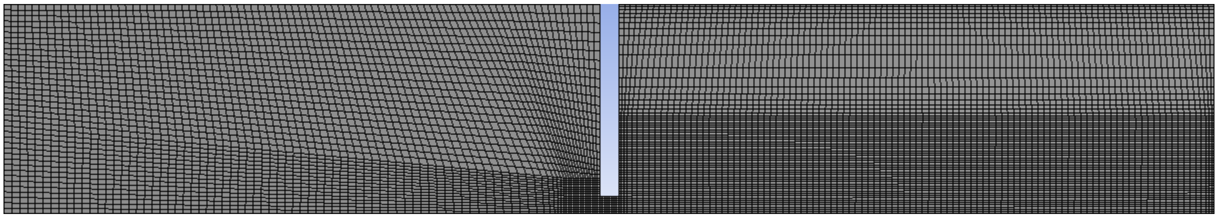

Figure D.14: Screenshot of the model mesh.

Solution Setup

Details of Fluent settings for solving the flow are as follows:

- General
  - Solver type: Density-based
  - Time: Steady
  - 2D Space: Axisymmetric
- Models
  - Energy: On
  - Viscous: Realizable k-e, Standard Wall Function, Compressibility Effects
- Boundary Conditions
  - Inlet: 2700 Pa, 1% turbulent intensity, 35 mm hydraulic diameter
  - Outlet: 50 Pa, 5% backflow turbulent intensity, 35 mm backflow hydraulic diameter
  - Walls: No slip, 0.5 roughness constant

The flow solution was verified by ensuring all residuals were less than 10^{-4}, the outlet average velocity and mass flow rates were constant, and the mass and energy conservation imbalance was less than 0.1%. A grid independence study was also performed by repeating the simulation with a finer mesh. All element dimensions of the original mesh was reduced by 20%, resulting in 14,500 elements. The velocity magnitude at 1,000 points on the axis was found for both meshes, and differences were less than 2.4%.

The discrete phase was assumed to not affect the fluid flow due to the small particle size. As a result, the steady state particle paths could be solved for after obtaining the flow solution. Using the single injection type, 15 particle diameters from 2 to 320 nm were released at the inlet at various radial positions. The particle material was chosen as Carbon, and this selection only determines the density used in calculations. The pre-defined drag law models in Fluent did not take into account the Cunningham slip correction factor for submicron sized particles, so a user defined function (UDF) was used instead. The UDF code can be found in Appendix B.2.

D.5.2 Results and Discussion

The contours of velocity magnitude in the flow is shown in Figure D.15. As expected, subsonic flow occurs before the orifice, and becomes supersonic afterwards. Pathlines of particles injected at the inlet is shown in Figure D.16 and the colours represent velocity. Two particles were trapped in the flow and do not exit the outlet. A focusing effect can be seen as more particles are closer to the axis after the orifice.

The radial position of nanoparticles at the outlet was obtained from Fluent. The Stokes number corresponding to every particle size simulated was calculated using Equation 2.5. The values of constants ρ_p, u_0, μ, and d_c were 2,000 kg/m^3, 340.29 m/s, 1.7894×10^{-5} kg/m·s, and 0.003 m, respectively. The Cunningham slip was calculated with the following correlation (Middha and Wexler, 2003):

$$C_c = 1 + Kn[1.257 + 0.4exp(-1.1/Kn)] \tag{D.12}$$

Results were found to best match those of Middha and Wexler (2003) when a 3.3 µm

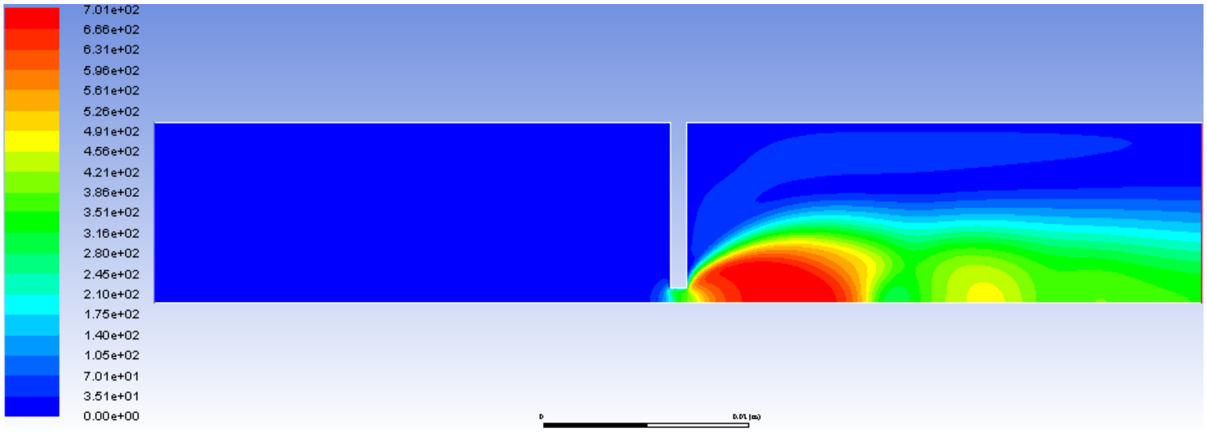

Figure D.15: Contours of velocity magnitude in the flow.

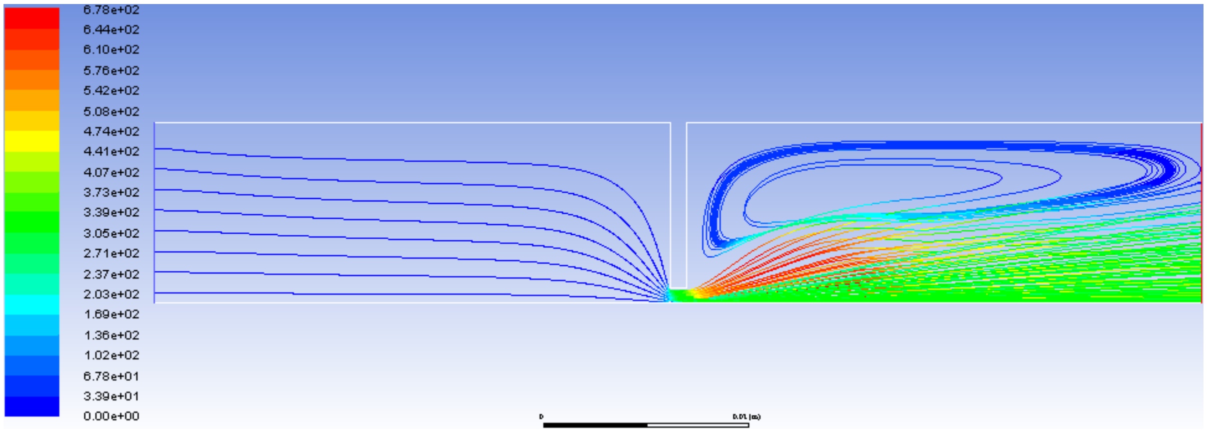

Figure D.16: Pathlines of injected nanoparticles showing velocity.

gas mean free path was used. This value corresponded to a pressure of 2,050 Pa, which suggests λ should be calculated at the orifice rather than before it. As particles pass the orifice, the gas mean free path decreases. A comparison of simulation results and the work of Middha and Wexler (2003) is shown in Figure D.17. Each plot is denoted by Rx, where x is the initial radial position of the particle upstream in mm.

The simulation results matched well with the work of Middha and Wexler (2003). A focusing effect can be observed for particles with a Stokes number of 1.0 and initially no further than 5 mm from the centerline upstream. Particles near the walls upstream were somewhat focused if the Stokes number is 0.75. Some differences can be seen with particle

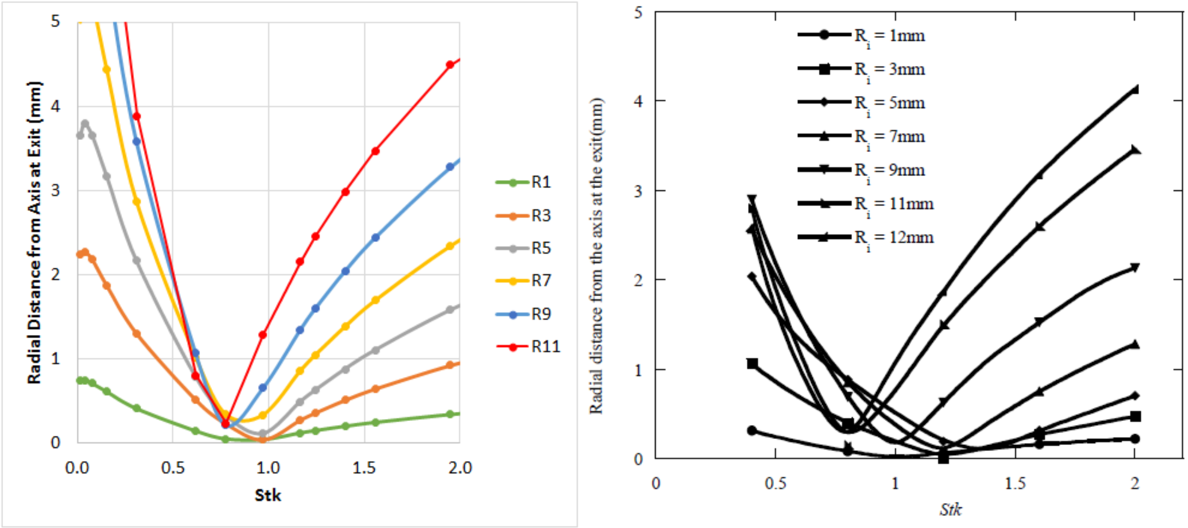

Figure D.17: Comparison of results from the simulation (left) and work of Middha and Wexler (2003) (right).

sizes which are not focused. In the simulation, those with a Stokes number of two were defocused to a much greater degree compared to the published work. The discrepancy can be attributed to different turbulence models selected, outlet pressure, and turbulence intensity set at the boundaries.

Although the base orifice design produces a focusing effect, it is likely not optimal for measuring PSD. Particles are focused in a small area as seen by the minimum point of each plot in Figure D.17. The aperture into the Faraday cup will have to be extremely small as a result. With an aperture radius of 1 mm, all particles initially 1 mm or closer to the centerline would be detected. For those further away, a sizable range of particle diameters would be detected as well. Since a large range of particle sizes are focused into a small aperture opening, performance of the APF decreases. Ideally, the plot should follow a Heaviside function such that $H(x) = 0$ for a small range of Stokes number.

Particles focused by the orifice also depends on their initial location upstream, which is undesirable. This can be seen by the minimum point of each plot in Figure D.17 shifting to the left as Rx increases. Although the orifice focuses particles with Stokes number equal to one, this is only true for particles that were 7 mm or closer to the centerline upstream. Otherwise, particles with Stokes number equal to one can be as far as 1.5 mm from the axis at the exit. This effect causes a wider range of particle sizes to be detected by the Faraday cup. Also, less particles with the optimally focused size enters the Faraday cup, leading to additional error. Ideally, the minimum point of each plot should occur at the same Stokes number, regardless of Rx. This also helps produce an electrical signal above the detection threshold of the Faraday cup by ensuring all particles upstream with the optimally focused Stokes number are captured.